University of Alberta

Implementation of Functional Magnetic Resonance Imaging and Applications to Psychiatric Research

by

Morgan Charles Willson ©

A thesis submitted to the Faculty of Graduate Studies and Research in partial fulfillment
of the requirements for the degree of Master of Science

Department of Biomedical Engineering

Edmonton, Alberta

Spring 2003

National Library
of Canada

Acquisitions and
Bibliographic Services

395 Wellington Street
Ottawa ON K1A 0N4
Canada

Bibliothèque nationale
du Canada

Acquisitions et
services bibliographiques

395, rue Wellington
Ottawa ON K1A 0N4
Canada

Your file Votre référence

Our file Notre référence

The author has granted a non-exclusive licence allowing the National Library of Canada to reproduce, loan, distribute or sell copies of this thesis in microform, paper or electronic formats.

L'auteur a accordé une licence non exclusive permettant à la Bibliothèque nationale du Canada de reproduire, prêter, distribuer ou vendre des copies de cette thèse sous la forme de microfiche/film, de reproduction sur papier ou sur format électronique.

The author retains ownership of the copyright in this thesis. Neither the thesis nor substantial extracts from it may be printed or otherwise reproduced without the author's permission.

L'auteur conserve la propriété du droit d'auteur qui protège cette thèse. Ni la thèse ni des extraits substantiels de celle-ci ne doivent être imprimés ou autrement reproduits sans son autorisation.

0-612-82364-4

Canada

University of Alberta

Library Release Form

Name of Author: Morgan Charles Willson

Title of Thesis: Implementation of Functional Magnetic Resonance Imaging and Applications to Psychiatric Research

Degree: Master of Science

Year this Degree Granted: 2003

Permission is hereby granted to the University of Alberta Library to reproduce single copies of this thesis and to lend or sell such copies for private, scholarly or scientific research purposes only.

The author reserves all other publication and other rights in association with the copyright in the thesis, and except as herein before provided, neither the thesis nor any substantial portion thereof may be printed or otherwise reproduced in any material form whatever without the author's prior written permission.

Morgan Charles Willson
#1604 10001 Bellamy Hill
Edmonton AB
T5J 3B6

Date: January 6, 2003

University of Alberta

Faculty of Graduate Studies and Research

The undersigned certify that they have read, and recommend to the Faculty of Graduate Studies and Research for acceptance, a thesis entitled **Implementation of Functional Magnetic Resonance Imaging and Applications to Psychiatric Research** in partial fulfillment of the requirements for the degree of **Master of Science**.

Dr. Alan H. Wilman (Supervisor)

Dr. Peter H. Silverstone

R. Snyder

Dr. Richard E. Snyder

Date: Jan 5, 2003

Abstract

The objective of this thesis is to implement the technique of functional magnetic resonance imaging (fMRI) and apply it to psychiatric research. Prior to this work only magnetic resonance spectroscopy (MRS) and conventional magnetic resonance imaging (MRI) were used at the University of Alberta for evaluation of changes in human brain chemistry and structure. Functional MRI hardware for paradigm delivery and response collection, and software for analysis and presentation of fMRI results, were installed, set up, and tested. Specific cognitive paradigms were then developed to evaluate areas of the brain involved in language, reaction time, working memory, and motor activity. These paradigms were tested on volunteers and then applied to a psychiatric study of medications used in the treatment of bipolar disorder.

A double blind, placebo-controlled drug study was used to investigate the effects of lithium and dextroamphetamine on cerebral blood flow and brain activity. Dextroamphetamine and lithium were both found to decrease brain activation as measured using fMRI. Also, lithium was able to reverse the effects of dextroamphetamine stimulation after treatment.

Acknowledgements

I would like to thank my supervisors, Dr. Alan Wilman and Dr. Peter Silverstone, for the support and advice they have provided throughout the duration of my M.Sc. Without their guidance and leadership none of this work would have been possible. I would also like to thank all the people with whom I have worked over the last two years, professors Dr. Richard Snyder, Dr. Christian Beaulieu, and also Dr. Peter Allen for their support.

Thank you to all the graduate students, friends, and volunteers who have spent countless hours in the scanner while I performed my experiments; Your time and patience is appreciated.

Finally, I would like to thank my parents, Ken and Linda Willson, who have always provided the love and support necessary for me to succeed in academics, athletics, and life. I am eternally grateful.

Table of Contents

Chapter 1: Introduction

1.1 Introduction........1
1.2 Evaluation of Brain Function........1
1.3 The Scope of This Thesis........3
1.4 References........5

Chapter 2: Principles of Magnetic Resonance Imaging

2.1 Introduction........6
2.2 Nuclear Magnetic Resonance........6
  2.2.1 The Quantum Mechanical Description of NMR........6
  2.2.2 The Classical Description of NMR........10
2.3 Relaxation Mechanisms and Image Contrast........18
  2.3.1 T1 Contrast........19
  2.3.2 T2* and T2 Contrast........21
2.4 Magnetic Resonance Imaging........24
  2.4.1 Slice Selection........25
  2.4.2 Frequency Encoding........26
  2.4.3 Phase Encoding........27
  2.4.4 K-space........29
2.5 Echo Planar Imaging........32
  2.5.1 Single Shot EPI........33
  2.5.2 Limitations of Single Shot EPI........35
  2.5.3 Single Shot EPI Artifacts........35
    2.5.3.1 Nyquist Ghost........35
    2.5.3.2 Chemical Shift........36
    2.5.3.3 Magnetic Susceptibility Effects........37
  2.5.4 Safety........38
2.6 References........40

Chapter 3: Functional Magnetic Resonance Imaging

3.1 Introduction........42
3.2 Brain Structure and Function........43
  3.2.1 Human Brain Anatomy........43
    3.2.1.1 The Forebrain........43
    3.2.1.2 The Midbrain........44
    3.2.1.3 The Hindbrain........45
  3.2.2 Functional Neuroanatomy........45
    3.2.2.1 Motor Function........45
    3.2.2.2 Visual Function........47
    3.2.2.3 Working Memory........47
3.3 Cerebral Metabolism, Blood Flow, and the BOLD Effect........48
  3.3.1 Cerebral Metabolism and Blood Flow........49
  3.3.2 Blood Oxygen Level Dependant Contrast........52
  3.3.3 Properties of the BOLD Signal........53

3.4 Functional Magnetic Resonance Imaging Using the BOLD Effect... 56
    3.4.1 Paradigm Design.......... 57
    3.4.2 Paradigm Delivery and Response Collection.......... 58
    3.4.3 Data Collection.......... 59
3.5 References.......... 62

Chapter 4: Bipolar Disorder

4.1 Introduction.......... 66
4.2 Epidemiology.......... 66
4.3 Clinical Features and Diagnosis.......... 67
4.4 Treatment.......... 68
    4.4.1 Lithium.......... 68
4.5 Dextroamphetamine as a Model for Mania.......... 72
4.6 The Effects of Dextroamphetamine on Cerebral Blood Flow and Metabolism.......... 73
4.7 Neuroimaging Studies of Bipolar Disorder.......... 74
4.8 References.......... 76

Chapter 5: Analysis of Functional MRI Data

5.1 Introduction.......... 81
5.2 Image Pre-Processing.......... 82
    5.2.1 Motion Correction (Realignment).......... 83
    5.2.2 Spatial Normalization.......... 84
    5.2.3 Spatial Filtering (Smoothing).......... 87
5.3 Statistical Parametric Mapping (SPM).......... 88
    5.3.1 The General Linear Model.......... 89
    5.3.2 Statistical Inference.......... 90
    5.3.3 The Multiple Comparisons Problem.......... 91
5.4 Group Analysis.......... 92
5.5 ROI Analysis.......... 94
5.6 References.......... 97

Chapter 6: Methods

6.1 Introduction.......... 99
6.2 Development of Cognitive Tasks.......... 100
    6.2.1 Motor Task.......... 100
    6.2.2 Word Generation Task.......... 101
    6.2.3 Working Memory Task.......... 102
    6.2.4 Reaction Time / Spatial Attention Task.......... 104
6.3 Study Design.......... 106
6.4 Subjects.......... 108
6.5 Comparisons.......... 110
6.6 Subjective and Physiological Measurements.......... 114
6.7 Functional MRI Data Collection.......... 114
6.8 Data Analysis.......... 115

6.8.1 fMRI Data Pre-Processing..................................115
6.8.2 fMRI Single Subject Analysis (Voxel-wise Analysis)..................................116
6.8.3 fMRI Group Analysis..................................117
6.8.4 fMRI Response Data..................................120
6.8.5 Subjective and Physiological Measurements..........121
6.9 References..................................122

Chapter 7: Results

7.1 Introduction..................................125
7.2 Subjective and Physiological Measurements..................................125
7.3 Quantitative Measures of Task Performance..................................127
7.4 Functional MRI Task Summary..................................130
7.5 Functional MRI ROI Analysis Results..................................133
7.5.1 The Effects of Dextroamphetamine..................................135
7.5.2 The Effects of Lithium..................................136
7.5.3 Control Comparisons..................................138
7.5.4 The Effects of Lithium on Dextroamphetamine Stimulation..................................139

Chapter 8: Discussion

8.1 Introduction..................................143
8.2 Dextroamphetamine Causes a Decrease in Cerebral Blood Flow and Brain Activity..................................143
8.3 Lithium Causes a Decrease in Cerebral Blood Flow and Brain Activity..................................146
8.4 Lithium Causes a Reversal of the Effects of Dextroamphetamine Stimulation on Cerebral Blood Flow and Brain Activity..................................148
8.5 The Use of Functional Magnetic Resonance Imaging in Psychiatric Research..................................149
8.6 References..................................151

Chapter 9: Conclusions

Conclusions..................................154

Appendix A: Analysis of a Sample fMRI Data Set Using SPM99

Analysis Using SPM99..................................157

List of Figures

Figure 2-1 Zeeman Energy Levels.......... 9

Figure 2-2 Net Magnetization Resulting From a Static Magnetic Field, B_0..... 10

Figure 2-3 Precession of the Magnetization Vector in a Static Magnetic Field, B_0.......... 12

Figure 2-4 The Precession of the Magnetization Vector About B_{eff}.......... 15

Figure 2-5 The Magnetization Vector in the Laboratory and Rotating Frame... 17

Figure 2-6 Induced Current in a Coil of Wire and the Fourier Transform of the Resulting Signal.......... 18

Figure 2-7 Recovery of Longitudinal Magnetization After a 90° Pulse.......... 20

Figure 2-8 Recovery of Longitudinal Magnetization After a 180° Pulse.......... 20

Figure 2-9 Dephasing of the Transverse Magnetization.......... 22

Figure 2-10 Decay of the Transverse Magnetization.......... 23

Figure 2-11 Principles of Spatial Encoding.......... 24

Figure 2-12 Gradient Echo Pulse Sequence and K-Space Traversal.......... 32

Figure 2-13 Echo Planar Imaging Pulse Sequence.......... 34

Figure 2-14 K-Space Traversal For Echo Planar Imaging Sequences.......... 34

Figure 2-15 Nyquist Ghosting.......... 36

Figure 3-1 Four Lobes of The Human Brain.......... 44

Figure 3-2 The Motor Homunculus.......... 46

Figure 3-3 The Basic Visual Pathway.......... 47

Figure 3-4 The Stages of Aerobic Metabolism.......... 49

Figure 3-5 Principles of BOLD Contrast.......... 51

Figure 3-6 The Effects of Oxygenated Hemoglobin on the MRI Signal.......... 53

Figure 3-7 The Hemodynamic Response.......... 55

Figure 3-8 Block Design fMRI Paradigm.......... 57

Figure 3-9 EPI Images at Different Resolutions and Echo Times.......... 61

Figure 4-1 The Inositol Depletion Hypothesis.......... 70

Figure 4-2 The Phosphatidylinositol Cycle 71
Figure 4-3 Structure of Dextroamphetamine 73

Figure 5-1 Steps Involved in the Analysis of fMRI Data 82
Figure 5-2 Spatial Normalization of EPI Images 86
Figure 5-3 3D Gaussian Filter 88
Figure 5-4 Smoothing of EPI Images 88
Figure 5-5 Anatomical Template for Creation of Regions of Interest 96

Figure 6-1 Motor Task 101
Figure 6-2 Verbal Fluency Task 102
Figure 6-3 Working Memory Task 103
Figure 6-4 Reaction Time Task 105
Figure 6-5 Study Design 108
Figure 6-6 fMRI Comparisons 112
Figure 6-7 Left Pre-Central Gyrus ROI 119

Figure 7-1 Finger Tapping Rate 128
Figure 7-2 Reaction Time Task 129
Figure 7-3 Working Memory 129
Figure 7-4 Group Analysis of the Verbal Task 130
Figure 7-5 Group Analysis of the Memory Task 131
Figure 7-6 Group Analysis of the Reaction Time Task 132
Figure 7-7 Group Analysis of the Left and Right Hand Motor Tasks 133
Figure 7-8 The Effects of Lithium on Activated Pixels 140
Figure 7-9 The Effects of Lithium on BOLD Contrast 141

List of Tables

Table 2-1 T1 and T2 Values at 1.5T, 3.0T and 4.0T.............................. 21

Table 4-1 Common Symptoms of Depression and Mania......................... 68

Table 6-1 Subject Demographic Data... 109
Table 6-2 Regions of Interest for the fMRI Tasks.................................. 111
Table 6-3 fMRI Data Comparisons.. 113
Table 6-4 MRI Data Collection Parameters.. 115
Table 6-5 High Pass Filter Cut-Off Frequencies................................... 117
Table 6-6 Talairach Daemon.. 118

Table 7-1 The Effects of Dextroamphetamine on Heart Rate and Blood Pressure.. 126
Table 7-2 Changes in Subjective Responses.. 127
Table 7-3 Comparison Summary.. 134
Table 7-4 The Effects of Dextroamphetamine...................................... 135
Table 7-5 The Effects of Lithium (2).. 136
Table 7-6 The Effects of Lithium (3).. 137
Table 7-7 Control Comparison (4).. 138
Table 7-8 Control Comparison (5).. 139
Table 7-9 Effects of Lithium on Dextroamphetamine Stimulation (6)........... 140
Table 7-10 Effects of Lithium on Dextroamphetamine Stimulation (7).......... 142

Abbreviations

ATP	adenosine tri-phosphate
BA	Brodmann area
BOLD	blood oxygen level dependant
BW	bandwidth
CNR	contrast to noise ratio
CBF	cerebral blood flow
CGM	cerebral glucose metabolism
CING	cingulate gyrus
CT	computed tomography
CUN	cuneus
DCT	discrete cosine transform
DLPFC	dorsal lateral pre frontal cortex
DSM-IV	Diagnostic and Statistical Manual for Mental Disorders 4th Edition
EPI	echo planar imaging
FDG	fluorodeoxyglucose
fMRI	functional magnetic resonance imaging
FOV	field of view
FWHM	full width at half max
GLM	general linear model
GRE	gradient recalled echo
Hb	hemoglobin
I-1,4,5-P_3	1,4,5-triphosphate
ICBM	International Brain Mapping Consortium
IFG	inferior frontal gyrus
IMPase	inositol monophosphatase
INS	insula
IOG	inferior occipital gyrus
IPL	inferior parietal lobule
IPPase	inositol polyphosphate-1-phosphatase

LG	lingual gyrus
MFG	middle frontal gyrus
MI	myo-inositol
MNI	Montreal Neurological Institute
MOG	middle occipital gyrus
MRI	magnetic resonance imaging
MRS	magnetic resonance spectroscopy
N/2	nyquist ghost
NMR	nuclear magnetic resonance
PCG	pre-central gyrus
PET	positron emission tomography
PI	phosphatidylinositol cycle
PKC	protein kinase C
PME	phosphomonoester
PSMC	primary sensorimotor cortex
PRE	precuneus
RPMT	Ravens progressive matrices task
rCBF	regional cerebral blood flow
rCBV	regional cerebral blood volume
RF	radio frequency
ROI	region of interest
SE	spin echo
SFG	superior frontal gyrus
SMA	supplementary motor area
SNR	signal to noise ratio
SPECT	single photon emission computed tomography
SPL	superior parietal lobule
SPM	statistical parametric mapping
STG	superior temporal gyrus
SVC	small volume correction
T1	spin-lattice relaxation/longitudinal relaxation

T2	spin-spin relaxation/transverse relaxation/intrinsic relaxation
T2*	transverse relaxation
T2’	reversible decay
TE	echo time
THAL	thalamus
TR	repetition time
VAS	visual analog scale
WCST	Wisconsin card sorting task

Symbols

α	flip angle
β	parameter estimate
Θ	phase angle
$\hbar$	Planck's constant divided by 2π
μ	magnetic dipole moment
ρ	rotating frame
γ	proton gyromagnetic ratio
ψ	energy eigenstates
τ	torque
χ	susceptibility
ω	Larmor frequency
$\|\alpha\rangle$	spin parallel to static magnetic field
$\|\beta\rangle$	spin antiparallel to static magnetic field
Δy	spatial resolution in Y direction
Δx	spatial resolution in X direction
Δk_y	sampling period in k_y direction
Δk_x	sampling period in k_x direction
Δt	sampling time
$\mathbf{B_0}$	external static magnetic field
$\mathbf{B_1}$	radio frequency magnetic field
$\mathbf{B_{eff}}$	effective magnetic field
BW_{RF}	RF bandwidth
E	interaction energy
EMF	electromotive force
FOV	field of view
G_X	readout gradient
G_Y	phase encode gradient
G_Z	slice select gradient

$\mathcal{H}_z$	Hamiltonian
$\mathbf{I}$	spin angular momentum
k	Boltzman’s constant
$\mathbf{M_0}$	net magnetization vector
M_X	transverse magnetization (x)
M_{XY}	transverse magnetization
M_Y	transverse magnetization (y)
N_{freq}	number of acquisitions in the frequency encode direction
N_{pe}	number of phase encoding steps
SNR	signal to noise ratio
T	t-statistic
TE	echo time
TR	repetition time
T1	longitudinal relaxation time
T2*	transverse relaxation time (reversible + irreversible)
T2’	transverse relaxation time (reversible)
T2	transverse relaxation time (irreversible)

CHAPTER 1

Introduction

1.1 Introduction

The brain is the most fascinating organ in the human body. At approximately 1400 grams the human brain contains over 100 billion nerve cells each capable of making numerous connections with adjacent neurons [1]. It is through these connections that signals are sent out to skeletal muscle, return from sensory organs and travel from one area of the brain to another. Not only does the brain send and receive electrical signals it also interprets and processes them. Emotion, reason, conscience, and memory, all result from the interaction and communication between neurons in the brain. With such overwhelming complexity in design and function it is not surprising that we have only just begun to unravel the mysteries of the mind.

1.2 Evaluation of Brain Function

For centuries scientists and philosophers have speculated about the relationship between the anatomy of the brain and memory, emotion, thought, or conscience. During the Middle Ages it was thought that the soul was located in the heart. However, as knowledge of the body and the brain began to increase it was suggested that mental activities were located in the brain, specifically in the ventricles. Common sense was located in the lateral ventricles with imagination being located in the posterior part. The third ventricle was involved in reasoning, judgment and thought. Memory was believed to be located in the fourth ventricle. In the 17th century Franciscus de le Boë and Thomas Willis independently presented a revolutionary idea that the brain was composed of dedicated areas, each of which responsible for specific cerebral tasks [2]. At the end of the eighteenth century Franz Joseph Gall and his understudy Johann Caspar Spuzheim introduced the concept that the cerebral cortex was disseminated into specific functional areas. They further identified 27 of these areas, which represented moral and psychological attributes. The relative importance of each of these areas in an individual could be determined by feeling the surface of the skull for bumps or depressions over particular areas. Although the basic premise of phrenology was flawed, it introduced the concept of functional organization to the scientific community. The brain was the center of all mental and moral abilities, and specific functions could be localized to definite regions in the cerebral cortex [2]. In 1890, William James would link brain activity with changes in cerebral blood flow when he published *The Principles of Psychology;* with its publication James began a new science of measuring changes in blood flow associated with brain activity [3]. James' subject lay on a table, perfectly balanced at the center, which could tip up or down at either end. As the subject undertook a mental or emotional task the table was seen to tilt down at the head. James interpreted this as an increase in blood flow to the cortex associated with cerebral activity. The study of brain function and cerebral blood flow developed slowly over the next century until the advent of new brain imaging techniques, which permitted more precise evaluation of brain structure and activity. Computerized Tomography (CT), Positron Emission Tomography (PET), Single Photon Emission Computed Tomography (SPECT), and lastly the development of Magnetic Resonance Imaging (MRI) have lead to an increased interest in the use of techniques which rely on changes in cerebral blood flow to measure brain activity. In 1990 using MRI, Ogawa was able to show that brain activity could be measured using an MRI technique sensitive to changes in oxygenated blood levels resulting from cerebral activity [4]. This technique, referred to as functional magnetic resonance imaging, or fMRI, allowed researchers even greater insight into the connection between cerebral blood flow, oxygenation, and brain activity.

1.3 The Scope of this Thesis

This thesis deals with the development and application of functional magnetic resonance imaging (fMRI); in particular, the use of fMRI techniques to evaluate the effects of psychiatric medications on cerebral blood flow and brain activity. The second chapter is concerned with the fundamentals of magnetic resonance starting from the quantum mechanical and classical descriptions of nuclear magnetic resonance (NMR). From this, a description of the theory and principles of magnetic resonance imaging follows. The mechanisms providing contrast in MR images are also discussed here. The flexibility to provide variable contrast between different tissues or pathologies is one of the greatest advantages of using MRI. Finally, in this chapter a description of echo planar imaging (EPI) is provided, which is the pulse sequence generally used for fMRI. In the third chapter the reader is introduced to the physiology of neural activation with particular attention paid to the vascular consequences of cerebral activation. The vascular response is discussed as it relates to changes in the MRI signal that can be detected when performing an experiment designed to evaluate brain function. The fourth chapter deals with bipolar disorder. The cause, features, diagnosis, and treatment are discussed. The use of dextroamphetamine is then presented as a model for mania. The analysis of fMRI data is given in chapter five. Finally, in chapters six, seven, and eight, the development of fMRI at the University of Alberta is presented and an fMRI study of the effects of lithium and amphetamines in normal volunteers is described and discussed.

1.4 References

1. Orrison, W. (1995), *Functional Brain Imaging.* Mosby-Year Book, Inc.
2. Clarke, E. and Dewhurst, K. (1972), *An Illustrated History of Brain Function.* Sanford Publications, Oxford.
3. James, W. (1890), *The Principles of Psychology.* Harvard: Cambridge, MA.
4. Ogawa, S., et all. (1990), *Intrinsic Signal Changes Accompanying Sensory Stimulation: Functional mapping with magnetic resonance imaging*. Proceedings of the National Academy of Science USA. 89(13): 5951-5, 1992.

CHAPTER 2

Principles of Magnetic Resonance Imaging

2.1 Introduction

Bloch [1] and Purcell [2] first described the phenomenon of nuclear magnetic resonance (NMR) in 1946. The work would result in a shared Nobel Prize for physics awarded in 1952. NMR quickly became a powerful tool in the analysis of chemical composition and structure. It would be twenty-seven years after the discovery of NMR that Mansfield [3] would introduce the principles of slice selection and Lauterbur [4] would illustrate the principles of spatial encoding leading to the production of the first magnetic resonance image of a small clam.

2.2 Nuclear Magnetic Resonance

2.2.1 The Quantum Mechanical Description of NMR

For an atom to interact with a magnetic field it must possess a nuclear magnetic moment μ. The nuclear magnetic moment can be related to the spin angular momentum, **I,** by a quantity known as the gyromagnetic ratio γ.

$$\boldsymbol{\mu} = \gamma\hbar\mathbf{I} \tag{2-1}$$

where $\hbar$ is Planks constant divided by 2π ($\hbar = 1.054 \times 10^{-34}$ J*s)

For a given species the gyromagnetic ratio is a constant. In the case of the hydrogen nuclei $\gamma = 42.7$ MHz/Tesla.

The interaction energy, E, can be written in terms of the nuclear magnetic moment and the magnetic field strength $\mathbf{B_0}$.

$$E = \mu \bullet \mathbf{B_0} \qquad (2\text{-}2)$$

If we consider a single isolated hydrogen nuclei (I= ½) in a perfectly uniform magnetic field $\mathbf{B_0}$ oriented in the z direction, the interaction energy can be written by solving for μ and equating equations 2-1 and 2-2.

$$E = -\gamma\hbar\mathbf{I} \bullet \mathbf{B_0} \qquad (2\text{-}3)$$

By multiplying out the scalar product, the interaction energy can be written in terms of the quantum mechanical operator **I** and of the Hamiltonian, $\mathcal{H}_z$, for the magnetic interaction between a nuclear spin and a magnetic field.

$$\mathcal{H}_z = -\gamma\hbar \mathrm{B_0 I_Z} \qquad (2\text{-}4)$$

The energy eigenstates, ψ, can be found using the time independent Schrödinger equation.

$$\mathcal{H}_z\psi = E_z\psi \tag{2-5}$$

where E_z are the Zeeman energy eigenvalues. Substituting for $\mathcal{H}_z$:

$$-\gamma\hbar B_0 I_Z\psi = E_z\psi \tag{2-6}$$

Since **I** is the only operator in equation 2-6 the energy eigenstates will be the eigenstates of **I.** The eigenvalues of **I** in a spin one-half system are ±½. The two possible energy states that result when a spin one-half system is placed in a static magnetic field are referred to as $|\alpha\rangle$ and $|\beta\rangle$, which refer to spins oriented parallel to B_0 and spins oriented anti-parallel to B_0, respectively [5].

The Zeeman energy can be expressed as:

$$\Delta E = E(\alpha) - E(\beta) \tag{2-7}$$

$$\Delta E = \frac{1}{2}\gamma\hbar B_0 - \left(-\frac{1}{2}\gamma\hbar B_0\right) = \hbar\omega_0 \tag{2-8}$$

Therefore,

$$\omega_0 = \gamma B_0 \tag{2-9}$$

The angular frequency ω_0 is referred to as the Larmor precession frequency and is associated with the emission or absorption of energy as shown in Figure 2-1.

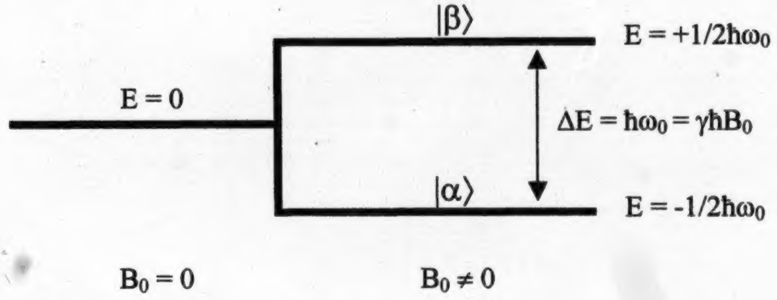

Figure 2-1

The Zeeman energy levels of a spin one-half system moved from a magnetic field of $B_0 = 0$ *to a magnetic field of* $B_0 \neq 0$.

For a population of independent spins at thermal equilibrium Maxwell-Boltzmann statistics can be used to determine the relative proportions of spins in each energy eigenstate [5]. In the absence of an external magnetic field the probability of finding a spin in either eigenstate is equal. When the system is placed in a non-zero magnetic field spins will tend to populate the lower energy state preferentially, which is parallel to the applied magnetic field.

$$\frac{N_{|\beta\rangle}}{N_{|\alpha\rangle}} = e^{-\frac{\Delta E}{kT}} \tag{2-10}$$

where N represents the number of spins in each energy eigenstate, k is the Boltzmann constant k = 1.38 x 10^{-23} J/K, and T is the temperature measured in Kelvin. For a population of spins in a magnetic field of 1.5T this ratio is only about 1:10^5.

Adding all the magnetic moments parallel to the field and subtracting the magnetic moments anti-parallel to the field results in the net longitudinal magnetization, **M**, of the sample parallel to B_0.

$$\mathbf{M} = \sum_{|\alpha\rangle} \mu_i - \sum_{|\beta\rangle} \mu_i \qquad (2\text{-}11)$$

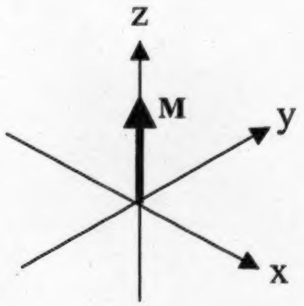

Figure 2-2

The net magnetization resulting from a population of spin one half nuclei placed in a uniform static magnetic field B_0.

2.2.2 The Classical Description of NMR

If the net longitudinal magnetization is placed in a static uniform magnetic field, $\mathbf{B_0}$, it will experience a torque, $\boldsymbol{\tau}$.

$$\tau = \mathbf{M} \times \mathbf{B_0} \tag{2-12}$$

Using Newton's Laws applied to angular mechanics, this torque will result in a rate of change of angular momentum.

$$\hbar \frac{d\mathbf{I}}{dt} = \frac{1}{\gamma} \frac{d\mathbf{M}}{dt} = \mathbf{M} \times \mathbf{B_0} \tag{2-13}$$

If $\mathbf{B_0}$ is a static time independent field oriented along the z-axis (i.e. $\mathbf{B_0} = 0\mathbf{i} + 0\mathbf{j} + B_0\mathbf{k}$), then the equations of motion for the different components of **M** can be written individually.

$$\frac{d\mathbf{M_x}}{dt} = \gamma \mathbf{M_y} B_0 \tag{2-14a}$$

$$\frac{d\mathbf{M_y}}{dt} = \gamma \mathbf{M_x} B_0 \tag{2-14b}$$

$$\frac{d\mathbf{M_z}}{dt} = 0 \tag{2-14c}$$

The solution for each component is found by solving each first order differential equation separately.

$$\mathbf{M_x}(t) = \mathbf{M_{xo}}\cos(\omega_0 t) - \mathbf{M_{yo}}\sin(\omega_0 t) \qquad \text{(2-15a)}$$

$$\mathbf{M_y}(t) = \mathbf{M_{xo}}\sin(\omega_0 t) + \mathbf{M_{yo}}\cos(\omega_0 t) \qquad \text{(2-15b)}$$

$$\mathbf{M_z}(t) = \mathbf{M_{zo}} \qquad \text{(2-15c)}$$

$$\omega_0 = -\gamma \mathrm{B}_0 \qquad \text{(2-16)}$$

These equations describe the precession of the magnetization vector about the z-axis as shown in Figure 2-3. Note that the angular precession frequency, ω_0, is identical to that obtained using the quantum mechanical description of NMR.

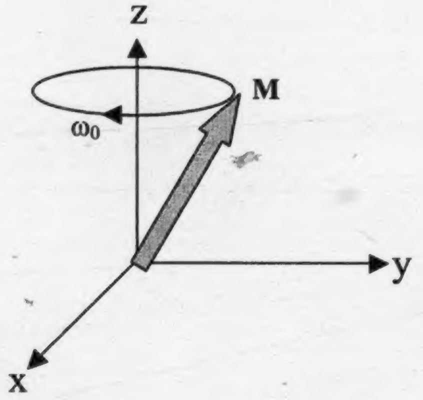

Figure 2-3

Precession of the magnetization vector in a static magnetic field aligned along the positive z-axis.

To create a transverse component of the rotating magnetization vector the net longitudinal magnetization must be tipped away from its equilibrium position along the positive z-axis. In addition to $\mathbf{B_0}$, the static uniform magnetic field, a circularly polarized magnetic field, $\mathbf{B_1}$, in a plane orthogonal to $\mathbf{B_0}$ is applied.

$$\mathbf{B_0} = 0\mathbf{i} + 0\mathbf{j} + B_0\mathbf{k} \tag{2-17}$$

$$\mathbf{B_1} = B_1 \cos \omega_0 t\mathbf{i} - B_1 \sin \omega_0 t\mathbf{j} + 0\mathbf{k} \tag{2-18}$$

The negative **j** term indicates that $\mathbf{B_1}$ rotates in a negative sense about the z-axis. The total magnetic field can then be written as the vector addition of the two fields.

$$\mathbf{B} = B_1 \cos \omega_0 t\mathbf{i} - B_1 \sin \omega_0 t\mathbf{j} + B_0\mathbf{k} \tag{2-19}$$

At this point it is helpful to describe a new coordinate system to view the resulting motion of the magnetization vector called the rotating frame, or rotating coordinate system, which will be referenced to by the subscript ρ [6]. The rotating reference frame rotates at the same frequency and in the same direction as the circularly polarized magnetic field $\mathbf{B_1}$. Therefore, anything rotating at the Larmor frequency in the laboratory frame will be stationary in the rotating frame. The components of the magnetization vector in the rotating frame can be related to the laboratory frame by the following equations.

$$\mathbf{M}_{x\rho} = \mathbf{M}_x \cos \omega t + \mathbf{M}_y \sin \omega t \tag{2-20a}$$

$$\mathbf{M}_{y\rho} = -\mathbf{M}_x \sin \omega t + \mathbf{M}_y \cos \omega t \tag{2-20b}$$

$$\mathbf{M}_{z\rho} = \mathbf{M}_z \tag{2-20c}$$

where ω is the frequency of $\mathbf{B}_1$.

If we apply the total magnetic field **B** (2-19) to the equation of motion (2-13) and subsequently substitute the new rotating reference frame equations (2-20a-c), the equations of motion for each component in the rotating frame can be obtained.

$$\frac{d\mathbf{M}_{x\rho}}{dt} = (\gamma B_0 + \omega)\mathbf{M}_{y\rho} \tag{2-21a}$$

$$\frac{d\mathbf{M}_{y\rho}}{dt} = -(\gamma B_0 + \omega)\mathbf{M}_{x\rho} + \gamma \mathbf{B}_1 \mathbf{M}_{z\rho} \tag{2-21b}$$

$$\frac{d\mathbf{M}_{z\rho}}{dt} = -\gamma B_1 \mathbf{M}_y \tag{2-21c}$$

These equations can be combined into a single vector equation of motion in the rotating frame.

$$\frac{d\mathbf{M}_\rho}{dt} = \gamma \mathbf{M}_\rho \times \mathbf{B}_{eff} \tag{2-22}$$

where

$$\mathbf{B}_{eff} = B_{1x\rho}\mathbf{i}_\rho + \left(B_0 + \frac{\omega}{\gamma}\right)\mathbf{k}_\rho \tag{2-23}$$

The equation of motion in the rotating frame has the same form as that derived in the laboratory frame (2-13). The main difference is in the form of $\mathbf{B}_{eff}$, which now has components in both the x and the z directions. $\mathbf{B}_{eff}$ will cause the magnetization to precess on the surface of a cone around the vector resultant of the rotating field $B_1\mathbf{i}$ and the off-resonance field $(B_0 + \omega/\gamma)\mathbf{k}$.

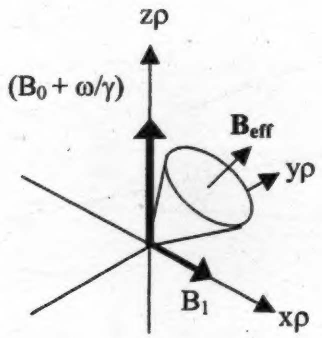

Figure 2-4

The precession of the magnetization vector about the vector resultant of the rotating field $B_1(t)$ and the off-resonant field $(B_0 + \omega/\gamma)$ in the rotating frame.

From equation 2-23, we can see that if ω is negative, and therefore rotates in a negative sense, that the contribution of $\mathbf{B_0}$ to $\mathbf{B_{eff}}$ can be eliminated if $|\omega| = \gamma B_0$ which is the definition of the Larmor frequency. At precisely these conditions the system is said to be on resonance and $\mathbf{B_{eff}} = B_1\mathbf{i}$. Therefore, at resonance the effective field is parallel to the polarized magnetic field $\mathbf{B_1}(t)$ and the magnetization vector can be tipped away from the z-axis to give rise to a transverse component and thus a detectable signal [5]. How far the magnetization is moved away from the z-axis and into the x-y plane depends on the strength of $B_1(t)$ and the length of time it remains on. The resulting angle with respect to the z-axis is referred to as the flip angle, α.

$$\alpha(t) = \gamma \int B_1 dt \qquad (2\text{-}24)$$

If a rectangular rf pulse is left on for a time $t = \pi/2\gamma B_1$ then the magnetization vector will have moved 90° from its starting position and will lie completely in the transverse plane. This is known as a 90° pulse and results in the maximum value of the transverse magnetization.

(a)

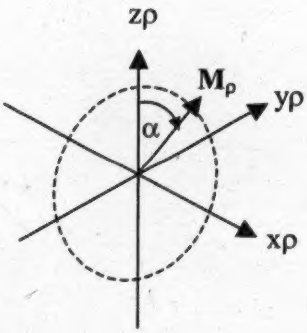

(b)

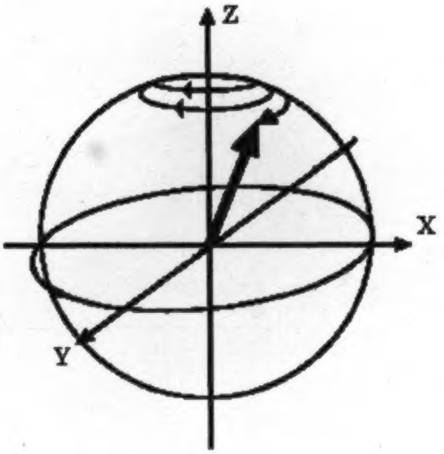

Figure 2-5

The magnetization vector during the application of an on-resonance radio frequency pulse in (a) the rotating reference frame and (b) the laboratory reference frame.

The rotating magnetization in the transverse plane will induce an electromotive force, or emf, in a coil of wire placed around the sample according to Faraday's Law of Induction.

$$emf = -\frac{d\phi}{dt} \tag{2-25}$$

where ϕ is the magnetic flux through the coil.

The rotating magnetic field, which oscillates at a frequency ω_0, induces a sinusoidal current in the coil of wire, which also oscillates at ω_0. The Fourier transform of the sinusoidal current waveform results in a delta function at the fundamental frequency, ω_0 [7].

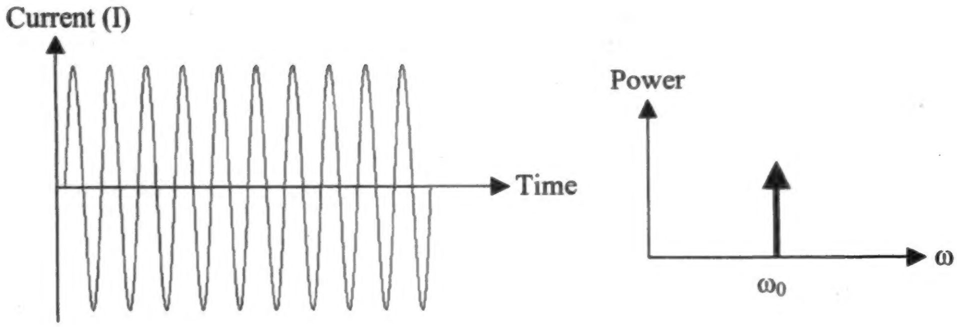

(a) (b)

Figure 2-6

(a) The oscillating current induced in a coil of wire wrapped around the sample after excitation. (b) The Fourier transform of the signal.

2.3 Relaxation Mechanisms and Image Contrast

We have now described the process by which a system of nuclear magnetic moments is prepared by placing the sample in a large magnetic field B_0 allowing a net longitudinal magnetization to result from the summation of nuclear magnetic moments. We have also seen how the use of a circularly polarized magnetic field applied orthogonal to B_0 at the Larmor frequency will excite the system and produce a transverse component. The process by which the spin system exchanges energy with its surroundings is called spin-lattice relaxation and can be characterized by the spin-lattice relaxation time, T1. Therefore, T1 relaxation describes the recovery of the longitudinal magnetization back to its equilibrium value of M_0. The spins not only exchange energy with their surroundings but also amongst themselves. This process is referred to as spin-spin relaxation and is characterized by the spin-spin relaxation time T2. Therefore, T2 relaxation describes the loss of the transverse component of the net magnetization vector back to its equilibrium value of zero.

2.3.1 T1 Contrast

The spin-lattice relaxation time, T1, is a measure of the time it takes for the longitudinal magnetization **M_z** to recover. T1 relaxation is governed by physical interactions with the surrounding molecular lattice and can be described by a first order rate equation.

$$\frac{d\mathbf{M}_z(t)}{dt} = \frac{\mathbf{M}_0 - \mathbf{M}_z(t)}{T1} \qquad (2\text{-}26)$$

where M_0 is the initial thermal equilibrium value of the longitudinal magnetization.

The solution gives us the equation for the recovery of M_z after perturbation by an RF pulse.

$$\mathbf{M}_z(t) = \mathbf{M}_0 + (\mathbf{M}_z(0) - \mathbf{M}_0)e^{-\frac{t}{T1}} \qquad (2\text{-}27)$$

At equilibrium the value of $M_z = +M_0$. If a 90° pulse is applied then all the longitudinal magnetization will be placed in the transverse plane and consequently $M_z(0) = 0$.

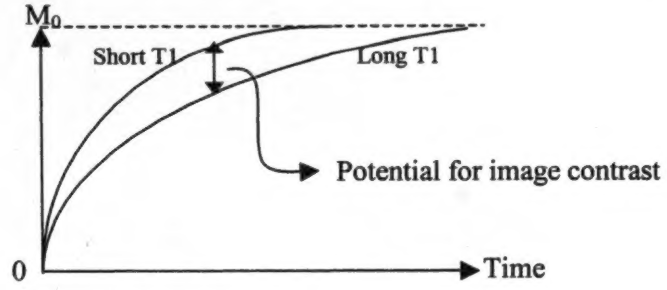

Figure 2-7

The Recovery of the net longitudinal magnetization following a 90° excitation pulse.

If the longitudinal magnetization vector is inverted with a 180° pulse prior to image acquisition then $M_z(0) = -M_0$. Different tissue components will then relax at different rates according to their T1's. At some point during the relaxation from $-M_0$ to $+M_0$ the magnetization must pass through zero. If an image is acquired precisely at this point then there will be no signal from the component with zero longitudinal magnetization.

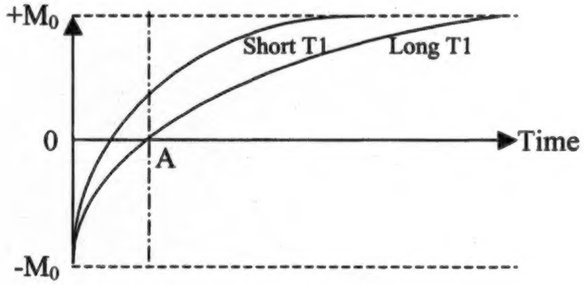

Figure 2-8

Recovery of the net longitudinal magnetization following a 180° inversion pulse. If imaging occurs at time t=A, there will be no signal from the tissue with long T1.

2.3.2 T2* and T2 Contrast

In practice, the magnetic field experienced by an ensemble of nuclei is never perfectly uniform. Magnet inhomogeneities, small magnetic fields created by nuclear dipoles or unpaired electron spins, and differences in the magnetic susceptibility of adjacent tissue can all cause local non-uniformities in the magnetic field [8]. These non-uniformities result in a decay of the transverse magnetization known at T2* decay which can be described by a first order rate equation.

$$\frac{d\mathbf{M}_{xy}(t)}{dt} = -\frac{\mathbf{M}_{xy}(t)}{T2^*} \tag{2-28}$$

In vivo, typical T2* values are much less than the corresponding T1 value. This suggests that the transverse magnetization decays to zero long before the longitudinal magnetization has fully recovered to $\mathbf{M}_0$.

	T1 White Matter (ms)	T2 White Matter (ms)	T1 Grey Matter (ms)	T2 Grey Matter (ms)
1.5T	790	100	920	92
3.0T	832	110	1331	80
4.0T	1043	50	1724	63

Table 2-1

T1 and T2 values for different tissues at field strengths of 1.5T, 3.0T, and 4.0T. [9-11]

If there are spatial or temporal non-uniformities in the main magnetic field, the net field experienced by the spins can be written as the sum of three parts. The main magnetic field $\mathbf{B_0}$, a time dependant field $\mathbf{b}$(x,y,z,t), and a static field $\boldsymbol{\beta}$(x,y,z).

$$\mathbf{B} = \mathbf{B}_0 + \mathbf{b}(x, y, z, t) + \boldsymbol{\beta}(x, y, z) \qquad (2\text{-}29)$$

The addition of these two fields causes the precession frequency of the spins to slowly dephase and consequently reduces the amplitude of the transverse magnetization to zero.

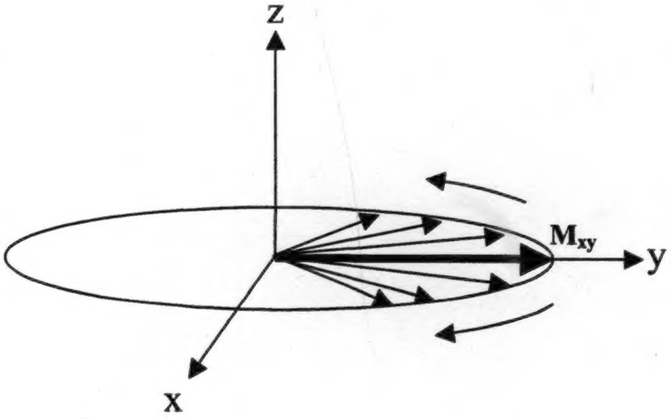

Figure 2-9

Dephasing of the transverse magnetization in the presence of magnetic field inhomogeneities.

Since there are two separate components contributing to the transverse decay, T2* can be written as the sum of these two effects [12].

$$\frac{1}{T2^*} = \frac{1}{T2} + \frac{1}{T2'} \qquad (2\text{-}30)$$

where T2 is the contribution of the time dependant component b, and is termed intrinsic, irreversible decay. T2' is the contribution of the static inhomogeneity β, and is expressed as reversible decay.

The static inhomogeneity is always present and constant and can therefore be reversed by applying a 180° refocusing pulse. The 180° pulse causes the spins to precess in the opposite direction. Fast spins revolving in a positive sense in the rotating frame reverse to revolve negatively and vice versa for slow spins. The net result of the 180° pulse is a refocusing of the transverse magnetization that was lost due to the static inhomogeneity.

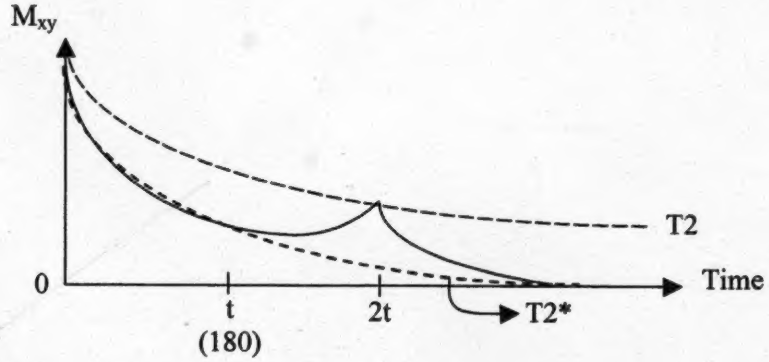

Figure 2-10

The decay of the transverse magnetization under T2 decay, T2 decay, and recovery of signal following a 180° pulse. The dashed lines show the exponential decay of the transverse magnetization under T2* and T2 decay. The solid line shows the resultant signal after application of a 180° pulse at time t and signal recovery at time 2t.*

2.4 Magnetic Resonance Imaging

Now that we have a thorough understanding of the concepts of NMR, we can proceed to the techniques required to generate spatially encoded NMR signals. With spatial information encoded in the acquired NMR signal it is possible to reconstruct an image of the original object using the intensity at each spatial location.

Spatial information is encoded in the NMR signal through the use of magnetic field gradients. These gradients vary linearly along an arbitrary orientation and serve to add or subtract from the main magnetic field at each location.

To spatially encode an NMR signal, slice selection is typically done to excite transverse magnetization within a thin slice of the object. Spatial locations can then be encoded within this slice using frequency and phase encoding which will be discussed later.

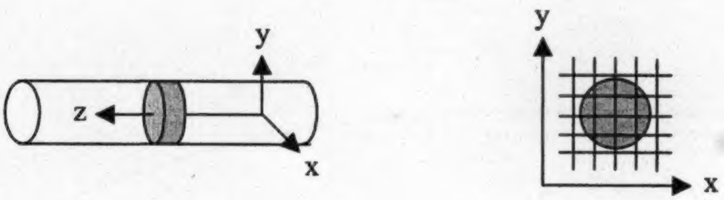

(a) (b)

Figure 2-11

Principles of encoding spatial information in the NMR signal (a) slice selection (b) frequency and phase encoding.

A linearly varying gradient **G,** applied in the presence of $\mathbf{B_0}$, will change the effective magnetic field along the direction it is applied.

$$\mathbf{B}_{\text{total}} = \mathbf{B_0} + \mathbf{Gr} \qquad (2\text{-}31)$$

where **r** is the displacement.

Substituting the new value $\mathbf{B}_{\text{total}}$ into equation 2-9 gives us an equation for the resonant frequency, which varies linearly with position. For a gradient in the x direction, G_x:

$$\omega_{total} = \gamma(B_0 + G_x x) \qquad (2\text{-}32)$$

or in the rotating frame:

$$\omega_p = \gamma(G_x x) \qquad (2\text{-}33)$$

By convention we will refer to slice selection using a gradient G_z, in the z direction, frequency-encoding using a gradient G_x, in the x direction, and phase encoding using a magnetic gradient G_y, applied in the y direction.

2.4.1 Slice Selection

To excite a slice, a gradient G_z is applied simultaneously with an RF pulse of bandwidth BW_{rf}, at a frequency ω_{rf}. As we have just seen the gradient has the effect of spreading out the resonant frequencies of the spins along the gradient direction. Only those spins, which have Larmor frequencies within the bandwidth of the pulse, will be excited.

The thickness of the slice excited depends on the bandwidth of the RF pulse and the strength of the gradient as shown in equation 2-34. Changing the centre frequency of the RF pulse can then alter the location of the slice.

$$Slice\_Thickness = \frac{BW_{RF}}{\mathrm{G_Z}} \qquad (2\text{-}34)$$

2.4.2 Frequency Encoding

Once a slice has been selected it is possible to encode spatial information by applying a magnetic gradient G_x, during signal acquisition. The effect of the magnetic gradient is to make the Larmor frequency of the nuclei spatially dependent. The signal received will have components with frequencies in a narrow range around ω_0. This range of frequencies is known as the signal bandwidth, BW_{freq} and can be described by the following equation.

$$BW_{freq} = \gamma \mathrm{G_x} FOV_x \qquad (2\text{-}35)$$

where FOV_x is the field of view in the direction of the frequency gradient direction and is equal to $x_{max} - x_{min}$.

If the object is completely contained within the field of view then satisfying the Nyquist criteria will ensure that there will not be any aliasing.

$$Sampling\_Frequency \geq 2 f_{max} \tag{2-36a}$$

$$Sampling\_Frequency \geq 2\gamma G_x x_{max} \tag{2-36b}$$

The spatial resolution in the frequency encode direction can be found by dividing the field of view by the number of points.

$$\Delta x = \frac{FOV_x}{N_{freq}} \tag{2-37}$$

where N_{freq} is the number of points collected in the frequency encode direction.

2.4.3 Phase Encoding

Phase encoding is used to encode spatial information into the NMR signal by applying a gradient G_y, during free precession. In the rotating frame precession at the Larmor frequency has been removed, therefore any spins that experience a total magnetic field in excess of B_0 will rotate in a positive direction in the rotating frame (fast spins), whereas any spins that experience less than B_0 will rotate in a negative sense (slow spins). The phase angle accumulated during a rectangular gradient pulse of duration τ can be found by multiplying the angular frequency in the rotating frame by the pulse duration.

$$\phi(y) = \omega(y)\tau \tag{2-38a}$$

$$\phi(y) = \gamma(\mathrm{G}_y y\tau) \tag{2-38b}$$

Notice that phase encoding only encodes one point per gradient pulse whereas in frequency encoding we can acquire many points (N). To collect all the data needed to reconstruct an image the entire process of slice selection, phase encoding, and frequency encoding is repeated M times changing the value of the phase encoding gradient by ΔG_y after each repetition. The final image resolution will then be N x M.

To avoid aliasing in the phase encode direction the Nyquist criteria must be obeyed. The Nyquist criteria states that the signal must be sampled at a rate at least twice the maximum frequency expected. For the phase encode situation this criteria correlates to a maximum phase shift of π radians between adjacent points that are sampled.

$$\Delta\phi_{\max} \leq \pi \tag{2-39}$$

But we know that the maximum phase shift can be related to the gradient strength and the field of view in the y direction.

$$\Delta\phi_{\max} = 2\pi f_{\max}\tau \tag{2-40a}$$

$$\Delta\phi_{\max} = \pi\Delta G_y FOV_y \qquad (2\text{-}40b)$$

Therefore to avoid aliasing the phase encode gradient must be incremented in steps ΔG_y such that:

$$\Delta G_y \le \frac{1}{\gamma FOV_y \tau} \qquad (2\text{-}41)$$

2.4.4 k-Space

K-space is a space in which frequency and phase take the place of displacement in real space [13]. For a phase encoding gradient pulse the phase of the rotating transverse magnetization depends on the gradient strength G, the duration of the pulse τ, as well as the position of the spins.

$$\phi(y) = y\gamma \int G\,dt \qquad (2\text{-}42)$$

We are interested in the accumulated phase as a function of y so we can rewrite this equation in terms of y and a new variable k.

$$\phi(y) = yk_y \qquad (2\text{-}43)$$

where:

$$k_y = \gamma \int G_y\,dt \qquad \text{(radians/meter)} \qquad (2\text{-}44a)$$

Similarly, in the frequency encode direction

$$k_x = \gamma \int G_x dt \qquad \text{(radians/meter)} \tag{2-44b}$$

Using the definitions for k-space in the phase encode and frequency encode directions we can express the distance between adjacent points in k-space, Δk.

$$\Delta k'_{freq} = \gamma G_x \Delta t \tag{2-45a}$$

$$\Delta k_{phase} = \gamma \Delta G_y \tau \tag{2-45b}$$

Relating the spatial resolution in the time domain to the resolution in the frequency domain we get the following equations.

$$\Delta k_x = \frac{1}{FOV_x} \tag{2-46a}$$

$$Sampling\_rate\_in\_k_x = \frac{2\pi N_{freq}}{\gamma G_x \Delta t} \tag{2-46b}$$

$$\Delta x = \frac{1}{\Delta k_y N_{freq}} \tag{2-46c}$$

$$\Delta k_y = \frac{1}{FOV_y} \tag{2-47a}$$

$$Sampling\_rate\_in\_k_y = \frac{2\pi}{\gamma \Delta G_y \tau} \tag{2-47b}$$

$$\Delta y = \frac{1}{\Delta k_y N_{phase}} \tag{2-47c}$$

To see how k-space is traversed by the application of gradients it is instructive to look at a simple 2D gradient echo image sequence. First, a spatially selective RF pulse is applied. A phase encode gradient G_y is then applied for a time τ. Finally, the frequency encode gradient G_x is applied during the acquisition of N points separated in time by Δt. This sequence is repeated M times with phase encode steps that vary by ΔG_y to acquire a matrix of N x M points.

Figure 2-12 shows a 2D gradient echo pulse sequence and the corresponding k-space traversal. During the time τ both the frequency and phase encode gradients are on resulting in the movement from the centre of k-space to line 1. The application of the frequency gradient by itself results in the traversal of k-space from left to right. During this time N points are acquired in the frequency encode direction. This sequence of events is repeated N times by varying the magnitude of G_y by ΔG_y and repeating data acquisition one line at a time from 1 to N. At the conclusion of the experiment k-space will have been completely covered and a total of N x N data points will have been collected.

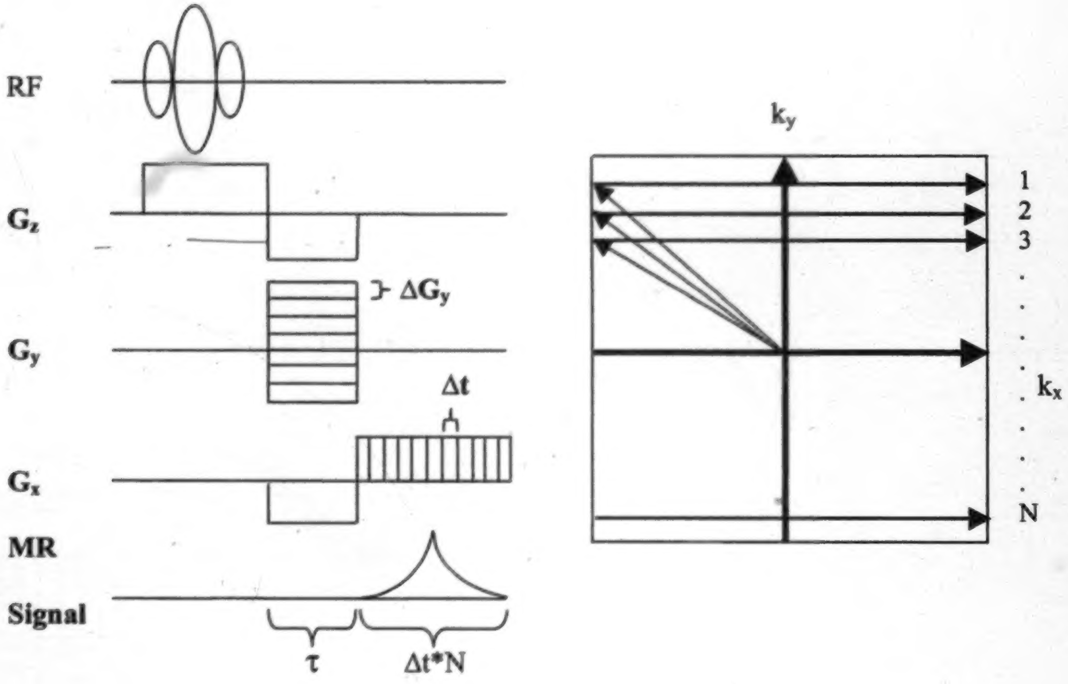

(a) (b)

Figure 2-12

(a) 2D gradient echo pulse sequence. (b) The k-space traversal pattern resulting from the application of gradients.

2.5 Echo Planar Imaging

Echo-planar imaging (EPI), first described by Mansfield in 1977 [14], is a fast imaging technique that allows collection of all the data required to reconstruct an image in a single excitation on the order of 30-100ms. This data acquisition strategy is much different than typical MRI sequences. As shown in Figure 2-12, conventional spin-echo (SE) and gradient-recalled-echo (GRE) pulse sequences collect a portion of the data during each excitation requiring multiple excitations to cover all of k-space. A significant advantage of EPI is that the image acquisition time is typically shorter that the period of physiological motion. The images effectively freeze motion caused by respiration, cardiac pulsation, or subject motion. Due to the significant hardware requirements to perform EPI it took 10 years from Mansfield's description before Rzedzian and later Ordidge produced the first EPI images of comparable quality to conventional MRI techniques [15-16]. Although initial progress in the field of EPI was slowed by the lack of fast switching magnetic field gradients, EPI is now used extensively for many applications such as diffusion and perfusion imaging, imaging of the heart and abdomen, as well as functional brain imaging.

2.5.1 Single-Shot EPI

Single shot EPI is the most commonly employed form of EPI in which a single excitation is used followed by a sequence of gradients that allows all the k-space data to be collected in one 'shot'. A typical single shot EPI pulse sequence is shown in Figure 2-13 and the resulting traversal of k-space in Figure 2-14. A slice selective RF pulse is applied then the data is acquired during the application of a rapidly switching frequency encode gradient. As the frequency encode gradient reverses polarity from positive to negative a small phase encode blip is applied to move to the next line in k-space. After N switches of the frequency encode gradient an N x N image can be reconstructed.

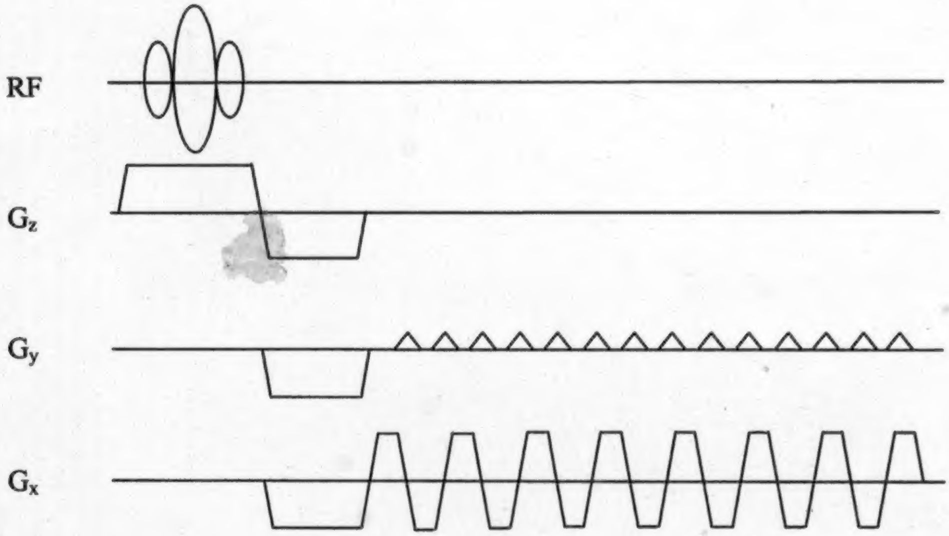

Figure 2-13

2D Echo Planar Imaging pulse sequence.

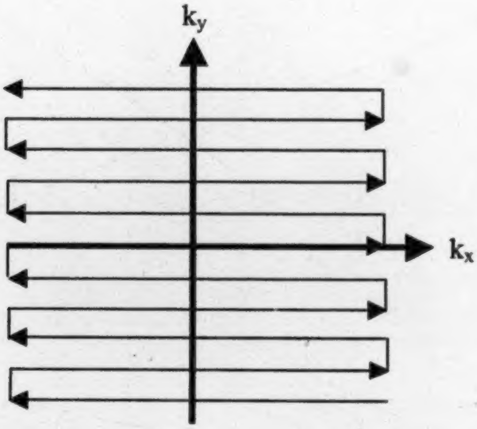

Figure 2-14

K-space trajectory for a 2D echo planar imaging sequence.

2.5.2 Limitations of Single Shot EPI

The data collection during an EPI readout takes place under the T2* decay envelope [17]. The image resolution is therefore limited to the number of points that can be collected before the signal decays below the noise level. Typical EPI resolutions are limited to 128x128 at 1.5T. However, it is often the effects of T2* blurring that limits the length of data collection, not the available signal. The long acquisition window means that very little signal remains for regions sampled at the edges of k-space. As a result high frequencies will not be well represented in the images causing them to be blurred.

2.5.3 Single Shot EPI Artifacts

Single shot EPI suffers from several image artifacts due to the gradient reversal used to traverse k-space and the long readout period. The most common artifact resulting from the acquisition of the signal under alternate gradient polarities in called the Nyquist ghost. The other effects are the result of spins that do not precess at exactly the frequency expected. This type of artifact is referred to as an off-resonance effect.

2.5.3.1 Nyquist Ghost (N/2)

EPI data acquisition takes place during a rapidly switched frequency encode gradient. This means that adjacent lines in k-space are acquired during a gradient read out of opposite polarity. Slight imperfections in the gradients, gradient induced eddy currents, fluid flow, or field inhomogeneities can cause mismatches in alternating lines of the raw k-space data. Mismatches in alternate lines of k-space results in a ghost image shifted by half of the field of view in the phase encode direction after the data has been Fourier transformed [18].

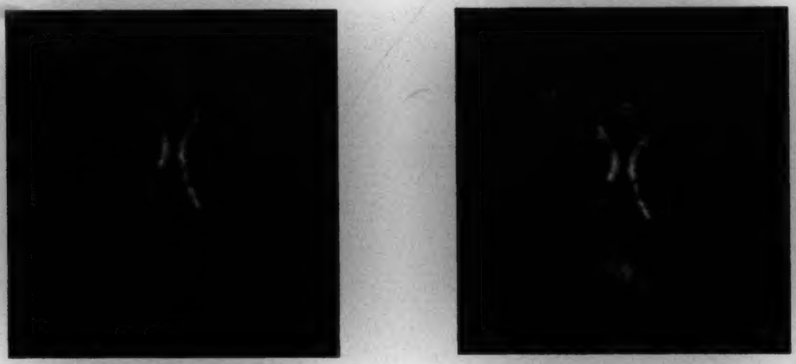

(a) (b)

Figure 2-15

Echo planar images acquired at 3T showing the effects of Nyquist ghosting; (a) an EPI image without Nyquist ghosting, and (b) an EPI image showing severe Nyquist ghosting overlapping structures of interest and obscuring anatomical detail.

2.5.3.2 Chemical Shift

A difference in the chemical environment observed by spins in different molecules results in spins precessing at frequencies other than the Larmor frequency. These differences in the frequency cause phase shifts that vary according to the magnetic field seen by the particular spin. When the data is Fourier transformed these phase shifts cause pixels to appear shifted in the phase encode direction. For example, fat spins precess at a frequency slower that water by 3.5ppm or 220Hz at 1.5T [9]. This frequency difference causes fat to be shifted from its true position. The amount of displacement in each direction is proportional to the inverse of the bandwidth. In the frequency encode direction the bandwidth is much higher than in conventional imaging because of the large gradients applied so displacements are small and do not influence image quality significantly. However, the gradients applied in the phase encode direction are very small by comparison. This results in very large fat/water shifts, up to several centimetres. The misregistration of fat can overlap tissues of interest disguising pathology or affecting results. The most common method of reducing the effects of fat chemical shift is to apply a fat saturation pulse prior to data acquisition nulling the fat signal contribution.

2.5.3.3 Magnetic Susceptibility Effects

Magnetic susceptibility refers to the variations in the magnetic field that result when a sample with heterogeneous magnetic properties is placed in the static magnetic field. The magnetic flux density B inside a sample containing susceptibility χ can be found from the following equation.

$$\mathrm{B} = (1+\chi)\mathrm{H} \qquad (2\text{-}48)$$

where H is the applied magnetic field strength.

Therefore, at the interface between two substances with different susceptibility a field inhomogeneity exists, ΔB_0, proportional to the difference in susceptibilities.

$$\Delta \mathrm{B}_0 = (\chi_1 - \chi_2)\mathrm{B}_0 \qquad (2\text{-}49)$$

Variations in magnetic susceptibility of tissues in vivo can cause signal loss or distortion analogous to chemical shift. However, the effect of magnetic susceptibility is not spatially constant. Instead of a constant shift, a geometric distortion or complete signal loss occurs. The degree of distortion increases with larger differences in susceptibility, higher field strengths, and also with longer acquisition times. Most notably these effects are pronounced at interfaces between air, bone, and soft tissue. The application of a 180° pulse can decrease these effects by refocusing the static inhomogeneities present in the sample. Another simple way to reduce susceptibility effects is to place the slices at an oblique angle sloping down from the front of the brain to the back. This way fewer slices cross the air, bone, and tissue interfaces of the nasal cavities, frontal sinuses, and temporal bone.

2.5.3 Safety

According to Faraday's law of induction a time varying magnetic field will induce a voltage in a conductor that is oriented perpendicular to the time rate of change of the magnetic field [19].

$$\oint E dx = \frac{1}{k}\frac{d\phi_B}{dt} \tag{2-50}$$

Therefore, the rapidly switching gradients used in EPI can induce electric currents in human tissue. Volunteers exposed to field changes of 60 T/s have reported sensations ranging from tickling to pain. The sensation is most pronounced near the extreme ends of the gradient coils where the change in magnetic field per unit time is the greatest. Also, since the magnitude currents induced in tissue is proportional to the cross-sectional area of the induced current, stimulation occurs at lower dB/dt when the z gradient is used for readout, (coronal or saggital EPI).

2.6 References

1. Bloch, F. et al. (1946), *Nuclear Induction*. Physics Reviews 69:127.
2. Purcell, E. et al. (1946), *Resonance Absorption by Nuclear Magnetic Moments in a Solid*. Physics Reviews 69: 37-38.
3. Mansfield, P. and Grannell, P.K. (1973), *NMR 'Diffraction' in Solids*? Journal of Physics C, 6: L422-L426.
4. Lauterbur, P. (1973), *Image Formation by Induced Local Interactions: Examples Employing Nuclear Magnetic Resonance*. Nature, 242: 190-191.
5. Haacke, E.M. (1999), *Magnetic Resonance Imaging, Physical Principles and Sequence Design*. John Willy & Sons.
6. Bronskill, M.J. (1993), *The Physics of MRI, 1992 AAPM Summer School Proceedings*. Woodbury: American Institute of Physics Inc.
7. Thomas, S. (2001), *Transient Magnetization Magnetic Resonance Angiography at 3.0 Tesla*. University of Alberta, M.Sc. Thesis.
8. Edelman, R. (1994), *Echo Planar MR Imaging*. Radiology, 192: 600-612.
9. Kuperman, V. (2000), *Magnetic Resonance Imaging, Physical Principles and Applications*. Academic Press.
10. Janaka P. et al. (1999), *NMR Relaxation Times in the Human Brain at 3.0 Tesla*. Journal of Magnetic Resonance Imaging, 9(4): 531-538
11. Jezzard, P. et al. (1996), *MRI Relaxation Times in Human Brain: Measurement at 4T*. Radiology, 199: 773-779.
12. Rajan, S.S. (1998), *MRI, a Conceptual Overview*. Springer-Verlag New York.

13. Slavin, G. (1997), *Theoretical and Experimental Advances in Multi-Shot Echo Planar Magnetic Resonance Imaging.* The Mayo Graduate School, PH.D. Thesis.

14. Mansfield, P. (1977), *Multi-Planar Image Formation using NMR Spin Echoes.* Journal of Physics C, 10: L55: 349-352.

15. Rzedzian, R. and Pykett, I. (1987), *Instant Images of the Heart Using a New , Whole-Body MR Imaging System.* American Journal of Roentgenology, 149: 245-250.

16. Ordidge, R., et al. (1998), *Snapshot Head Images at 0.5 T Using the Echo-Planar Technique.* Magnetic Resonance in Medicine, 8: 110-115.

17. Schmitt, F., et al. (1998), *Echo-Planar Imaging: Theory, Technique and Application.* Springer-Verlag Berlin.

18. Stehling, M., et al. (1991), *Echo-Planar Imaging: Magnetic Resonance Imaging in a Fraction of a Second.* Science, 254: 43-50.

19. Shellock, F. (1996), *Magnetic Resonance: Bioeffects, Safety, and Patient Management, 2^{nd} Ed.* Lippincott Williams & Wilkins Philadelphia.

CHAPTER 3

Functional Magnetic Resonance Imaging

3.1 Introduction

Modern functional neuroimaging began in 1948 when Kety and Schmidt described the nitrous oxide technique for measuring cerebral blood flow (CBF) [1]. Using nitrous oxide as an indicator in the blood, they measured the difference between arterial inflow and venous outflow from which a measure of cellular uptake could be obtained. With this new method it was possible to use CBF to monitor brain activity for the first time; however, it was useful only for global calculations. In 1963 Glass and Harper developed a new technique to measure CBF using the radioactive isotope Xenon – 133 [2]. Xe-133 emits gamma rays, which can be used to measure regional cerebral blood flow (rCBF). The development of computed tomography (CT) in the 1970's allowed mapping of the distribution of radioisotopes in the brain using a technique called single photon emission computed tomography (SPECT). In 1984, Fox et al. published the first study using a radioisotope that emits positrons instead of photons. This new technique was named positron emission tomography (PET) [3]. Although PET was more expensive and labor intensive than SPECT its greater spatial resolution allowed researchers to gain new insight into the functional neuroanatomy of the human brain. The next revolution in functional imaging would come in 1990 when Ogawa described the blood oxygen level dependant (BOLD) contrast mechanism for evaluation of brain activity and cerebral blood flow using magnetic resonance imaging [4].

3.2 Brain Structure and Function

Functional magnetic resonance imaging (fMRI) is a method used to evaluate human brain function. Therefore it is instructive to provide a brief overview of the functional neuroanatomy of the brain before introducing the principles of fMRI. For more in depth reference on the anatomy and biochemistry of the brain refer to references [5], [6], and [7].

3.2.1 Human Brain Anatomy

The central nervous system consists of the spinal cord and the brain. Together, the brain and spinal cord coordinate and interpret sensory activity transmitted from the periphery and process information to be transmitted back to muscles, organs, or other areas of the brain. The brain can be subdivided into 3 segments: the forebrain, midbrain, and hindbrain.

3.2.1.1 The Forebrain

The forebrain consists of the cerebral hemispheres and the structures that make up the diencephalon, most notably the thalamus and hypothalamus. The cerebral hemispheres are the most obvious external feature of the brain and are separated into the left and right hemispheres by the interhemispheric, or longitudinal fissure. Transmission of information between the two hemispheres occurs by way of a band of tissue known as the corpus callosum, which connects the hemispheres. Each hemisphere can be divided into four lobes: the frontal lobe, the parietal lobe, the temporal lobe, and the occipital lobe. The frontal lobes are involved in the planning, execution, and evaluation of actions. The parietal lobes receive information from the senses such as touch, pain, temperature, and pressure, and are concerned with perception and integration of these senses. Finally, the occipital lobes consist mainly of the visual cortex, and the temporal lobes consist of areas involved in auditory and speech processing. The frontal lobe and parietal lobe are separated by the central sulcus whereas the temporal lobe is separated from the rest of the cortex by the lateral fissure.

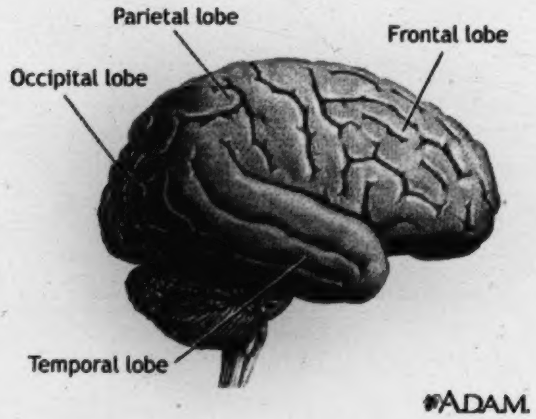

Figure 3-1

The human brain divided into the four lobes of the cerebral hemispheres. © *2002 adam.com.*

3.2.1.2 The Midbrain

The midbrain lies deep within the brain and consists of two major components; the tectum and tegmentum. The tectum forms the posterior part of the midbrain and consists of a number of distinct nuclei, notably the superior and inferior colliculi which receive sensory input from the visual and auditory systems respectively. The tegmentum, which is involved in the control of movement, lies anterior to the tectum and contains the substantia nigra and the red nucleus.

3.2.1.3 The Hindbrain

The hindbrain consists of the cerebellum, which is a large structure that hangs posterior and below the rest of the brain, the pons, and the medulla oblongata. The cerebellum receives and relays information related to balance, position, and muscle tone, which function to coordinate fine movement and coordination. The pons and medulla are structures that link the spinal cord to the rest of the brain. These areas control some of the most basic physiological processes such as respiratory rate and heart rate.

3.2.2 Functional Neuroanatomy

After a brief introduction to the major structural components of the brain we will now see how these structures interact to perform various functions of interest such as movement, vision, and memory.

3.2.2.1 Motor Function

The primary motor cortex lies anterior to the central sulcus and is organized topographically according to a rough map of the human body known as the motor homunculus. The motor homunculus does not give equal representation to every part of the body; rather, it accentuates certain areas that require a high level of control or dexterity, like the hand for example.

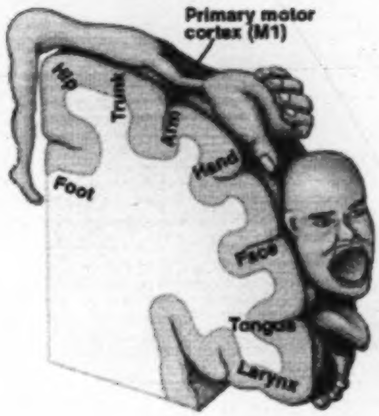

Figure 3-2

The motor homunculus in primary motor cortex. ©1999-2002 brainconnection.com

The other major component of the motor system located in the cerebral cortex is the somatosensory cortex. The somatosensory cortex lies posterior to the central sulcus and functions to integrate and interpret sensory signals from the periphery. Similar to the primary motor cortex the somatosensory cortex is organized according to the sensory homunculus, which devotes more cortical surface area to those areas of the body that require keen sensory ability, such as the lips and fingertips. Sensory motor information travels from the periphery up the spinal cord until it reaches the base of the medulla. In the medulla, ascending motor signals decussate so that signals from the left side of the body travel to the right side of the brain and vice versa. Motor information travels through the thalamus, which functions as a relay station for information, then on to the somatosensory cortex. Descending motor information travels in the opposite direction, originating in the primary motor cortex, traveling through the thalamus, and crossing over in the medulla on the way to its target muscle.

3.2.2.2 Visual Function

The primary visual cortex is located in the posterior aspect of the brain in the occipital lobe. Visual information enters the eye and falls upon the retina. The retina responds by sending visual information along the optic nerve in each eye to the visual cortex for interpretation. The optic tract crosses over at the optic chiasm so that the right visual field of each eye is mapped to the left visual hemisphere and the left visual field to the right hemisphere.

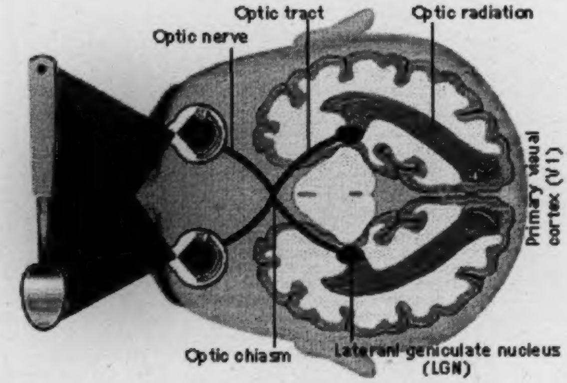

Figure 3-3

The basic visual pathway. © 1999-2002 brainconnection.com

3.2.2.3 Working Memory

Memory can be divided into separate classes based on the length of time the memory lasts. Immediate memory lasts only a few seconds, working memory lasts a few minutes, and long-term memory can last anywhere from hours to years. Furthermore, long-term memory can be further divided based on the accessibility of the stored information. Explicit memories are available for recollection and use by other cognitive systems. Facts and knowledge are included in explicit memory as is the memory of specific events. On the other hand implicit or procedural memory includes skills, habits, and other unconscious, automatic functions that alter actions and performance [8]. Working memory has been implicated as a symptom of several psychiatric disorders including schizophrenia [9] and bipolar disorder [10]; therefore, for this thesis we will limit the discussion to working memory. For more in depth examination of memory processes refer to references [11], and [12]. Working memory is composed of three components. The first is a buffer that stores verbal information called the phonological loop. The second component of working memory is a buffer that stores visual-spatial information, the visio spatial sketchpad. Lastly there exists a central executive, which regulates the activity of the two buffers and helps to interpret and recall the information that is stored within each buffer [13]. Working memory has been shown to be the result of activity in several cognitive areas. Visual-spatial information is stored in the right parietal region whereas verbal information is stored in the left parietal region and left temporal region, which is also involved in language and speech. The central executive consists of areas found in the frontal lobes. The left dorsal lateral pre-frontal cortex, DLPFC, is frequently activated in neuroimaging experiments employing working memory tasks and is considered a prime candidate for the central executive [14].

3.3 Cerebral Metabolism, Blood Flow, and the BOLD Effect

Functional magnetic resonance imaging relies on the delivery of oxygen to actively metabolizing tissue. It is a change in oxygenation of the local tissue that provides the mechanism by which brain function can be evaluated.

3.3.1 Cerebral Metabolism and Blood Flow

Whenever a tissue is metabolically active it requires a steady supply of glucose and oxygen, which is supplied by the surrounding vasculature. In the brain, neural activity is described as the propagation of action potentials, which rely on a separation of charge across the membrane. The Na+/K+ pump, which creates the resting membrane potential, requires energy in the form of adenosine triphosphate or ATP. ATP is produced through the full metabolism of glucose, which includes glycolysis, pyruvate decarboxylation, the Krebs cycle, and oxidative phosphorylation as shown in Figure 3-4.

a. Glycolysis: Glucose ($C_6H_{12}O_6$) → 2 Pyruvate + 6 ATP

b. Pyruvate Decarboxylation: 2 Pyruvate → 2 Acetyl CoA + 6ATP

c. Krebs Cycle:

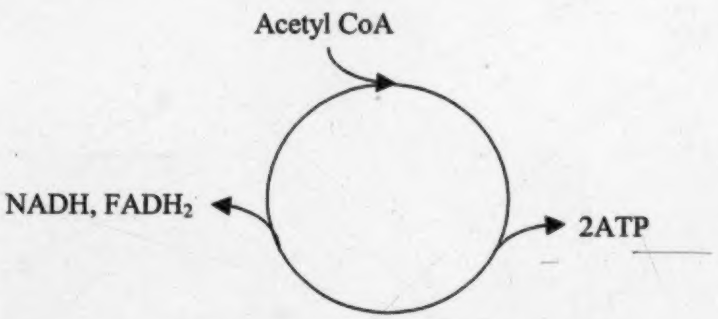

d. Oxidative Phosphorylation: NADH, FADH$_2$ + O_2 → 22ATP

Figure 3-4

The stages of aerobic metabolism, which break down glucose to form ATP.

The overall reaction for the breakdown of glucose is then given by:

$$\text{Glucose}\ (C_6H_{12}O_6) + 6O_2 \longrightarrow 6CO_2 + 6H_20 \quad (+36\ \text{ATP}) \tag{3-1}$$

The full metabolism of one mole of glucose results in the production of 36 moles of ATP that can be used to fuel metabolic processes. During the breakdown of glucose 6 moles of oxygen are needed as the final electron acceptors in the electron transport chain (oxidative phosphorylation). The rate of oxygen consumption can therefore be used as a measure of cellular metabolism in a particular tissue.

Oxygen is carried through the bloodstream by hemoglobin, Hb, which is a globular protein consisting of four polypeptide subunits each containing a non-protein portion called heme. Each heme portion contains an Fe(II) ion in the center of a ring structure which is able to bind reversibly to oxygen. When Hb has oxygen bound it is referred to as oxygenated hemoglobin, or oxy-Hb, whereas Hb that does not have oxygen bound is referred to as deoxy-hemoglobin, or deoxy-Hb.

Intuitively, it seems reasonable to assume that when a cerebral region becomes metabolically active that the increase in oxygen consumption by the tissue would drive the local concentration of oxy-Hb down. However, it has been shown that regional cerebral blood flow, rCBF, and regional cerebral blood volume, rCBV, increases significantly in response to neuronal activation, whereas oxygen consumption does not increase to the same extent [15]. The net result is an overall increase ~~in~~ the regional oxy-

Hb content of the tissue. The mechanism of this effect is not well understood but it has been hypothesized to involve chemical messengers such as nitric oxide, adenosine, hydrogen, potassium, or a direct link between the vasculature and the central nervous system [16-18]. As we have alluded to previously, it is the change in the oxygenation level in a localized region that allows the use of fMRI techniques to evaluate brain function.

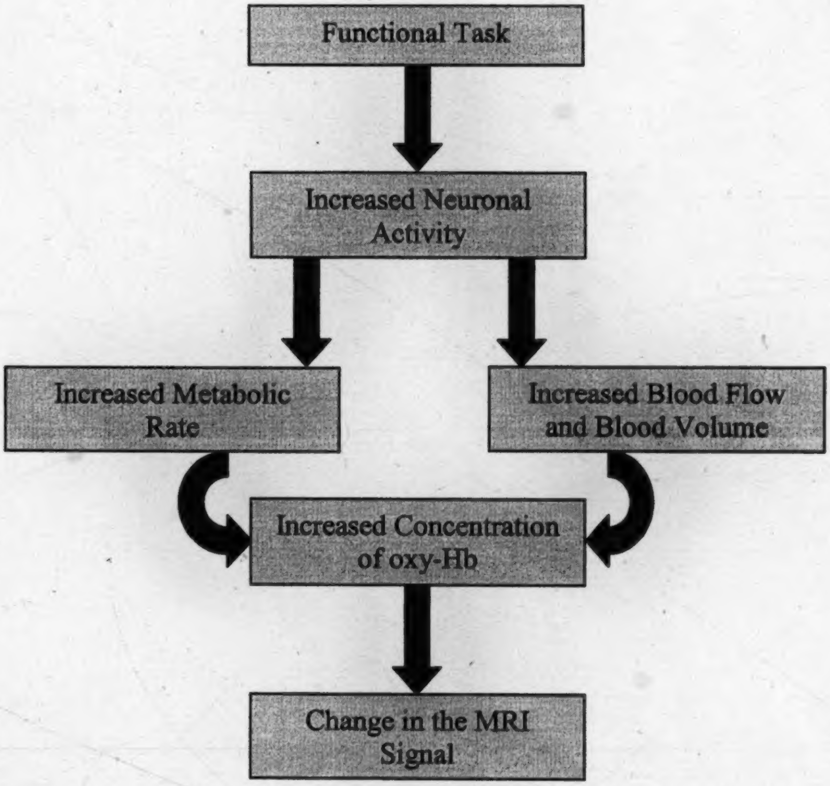
Functional Task
Increased Neuronal Activity
Increased Metabolic Rate
Increased Blood Flow and Blood Volume
Increased Concentration of oxy-Hb
Change in the MRI Signal

Figure 3-5

The sequence of events leading up to a detectable change in the MRI signal due to a change in neuronal activity.

3.3.2 Blood Oxygen Level Dependant Contrast

Blood oxygen level dependant, (BOLD), contrast refers to the effect that blood oxygen content has on the MRI signal. As early as 1936 it was known that the magnetic properties of Hb depend on the amount of oxygen bound [19]. Deoxy-Hb is a paramagnetic molecule whereas oxy-Hb is diamagnetic. As such, deoxy-Hb interacts with the magnetic field, **B**, causing a susceptibility difference between the molecule and the surrounding tissue. This susceptibility difference causes the spins within that region to precess at different rates depending on the local net magnetic field. The difference in frequency caused by local inhomogeneities results in dephasing of the NMR signal in regions of high deoxy-Hb content. In contrast, oxy-Hb does not interact with the magnetic field and therefore does not produce a susceptibility difference [20]. When an area of the brain becomes metabolically active, there is an increase in the local concentration of oxygenated blood and therefore oxy-Hb [21]. This increase in the relative concentration of oxy-Hb decreases the dephasing effects of deoxy-Hb, which is now in a relatively smaller proportion in the local vasculature. The net effect of an increase in oxy-Hb is an increase in the T2* value for that particular region and a concomitant increase in the local NMR signal [22].

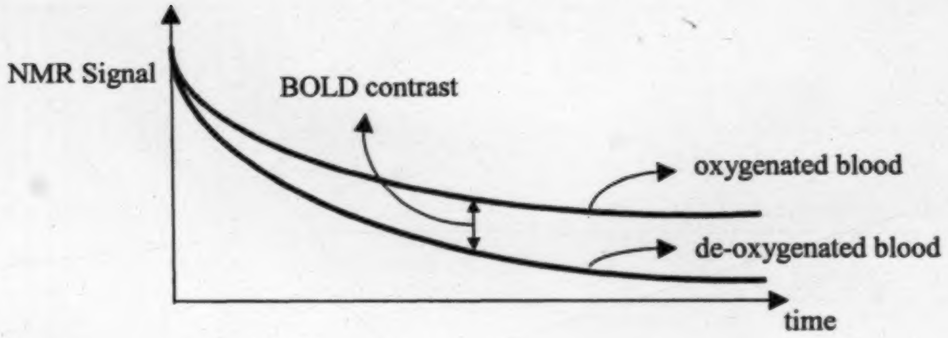

Figure 3-6

The T2 signal decay of the NMR signal showing the effects of oxygenated hemoglobin and de-oxygenated hemoglobin on the MRI signal.*

3.3.3 Properties of the BOLD Signal

The BOLD signal is not a direct measure of neuronal activity; instead, it is the end result of a complex metabolic and vascular response to increased brain function. Because neuronal activity is not being measured directly, there is a time delay from the onset of a particular stimulus until a measurable change in the BOLD response. This delay varies depending on the type of stimulus, the intensity, and the area of the brain being activated. From time t=0, when the stimulus begins there is characteristically a small initial negative dip in the BOLD signal, which may only be detectable at high magnetic field strengths, lasting approximately 1-2 seconds before there is a positive change from baseline and then another 1-8 seconds before the BOLD response has reached its maximum value [23]. The initial negative dip results from a brief decrease in oxy-Hb levels before the vasculature has time to respond to the increase in oxygen consumption. Upon reaching the maximum value there is a relatively constant maintenance of this level until discontinuation of the stimuli. After cessation of the stimulus the BOLD response returns to baseline levels on the order of a few seconds in two steps. First the BOLD response decreases to below baseline levels and then slowly recovers back to the original starting level. The post-stimulus undershoot results from a decreased oxy-Hb proportion persisting after blood flow has returned to baseline levels. Although the mechanism remains controversial it has been speculated to result from either increased oxygen extraction or increased cerebral blood flow after the vascular system has returned to normal levels. The characteristic vascular response to increased neuronal activity is called the hemodynamic response function, or hrf. The hemodynamic response function has implications for the final temporal resolution that can be obtained using functional MRI. The initial dip, rise to maximum, maintenance at maximum levels and a post-stimulus undershoot can all be seen in Figure 3-7, which shows a typical hemodynamic response for a task lasting eighteen seconds.

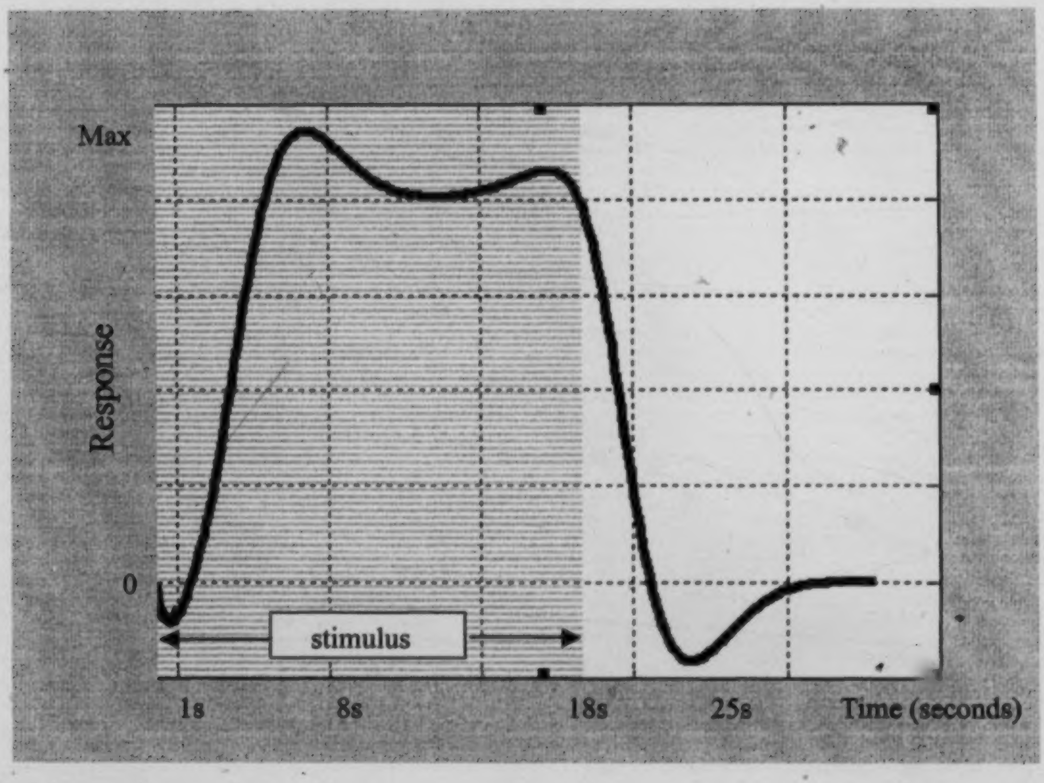

Figure 3-7

The hemodynamic response resulting from an 18 second stimulus representing a change in neuronal activity and the return to baseline levels.

If the BOLD response is to represent neuronal activity spatially, it should be composed of signal originating from the capillary bed exclusively because these vessels are in closest contact with the active neurons. However, the measured BOLD signal contains contributions from both the arterial vasculature that supplies fresh oxygenated blood and the venous system that returns blood back to the lungs. Arteries regulate the inflow of oxygenated blood and can have significant changes in volume associated with increased blood supply to tissue. Veins on the other hand collect all the oxygenated blood that was not consumed by the tissue. Therefore, both arteries and veins can have a significant effect on the measured BOLD signal [24]. Evidence from high-resolution fMRI suggests that the BOLD response increases proportional to B_0 for large vessels and proportional to B_0^2 for small vessels and capillaries suggesting an advantage to working at high field strengths [25]. This evidence has been supported at higher field strengths where there is a greater contribution to the BOLD signal from the capillary bed and less from large neighboring veins compared with lower field strengths [26]. However, recent evidence has shown that this increase is mitigated by other factors such as increased physiological noise and increased susceptibility artifacts at high field strengths, which reduces the signal to noise ratio, SNR, and contrast to noise ratio, CNR, so that actual increases are less than the theoretical B_0, and B_0^2, for large vessels and capillaries respectively [27]. This suggests that there are significant benefits to performing functional imaging experiments at higher field strengths but eventually a limit will be reached where the gains in NMR signal strength will be overcome by increased noise.

3.4 Functional Magnetic Resonance Imaging Using the BOLD Effect

A typical functional MRI experiment is carried out as a series of alternating blocks of stimulus and control tasks during which MRI images are collected continuously with a fast imaging sequence. The result is a time series of MRI images that follow the time course of the experimental paradigm where each volume of images represents a single time point in the series. The data must then be evaluated using statistical analysis prior to generating a three dimensional map of areas of the brain which are significantly correlated to the task.

3.4.1 Paradigm Design

Most paradigms for functional MRI studies are block-designs. A block design has alternating periods of each condition that repeat for the duration of the experiment. To accommodate the hemodynamic response, the length of each block is usually chosen to be greater that fifteen seconds to ensure adequate time for the BOLD signal to reach its maximum before changing stimuli.

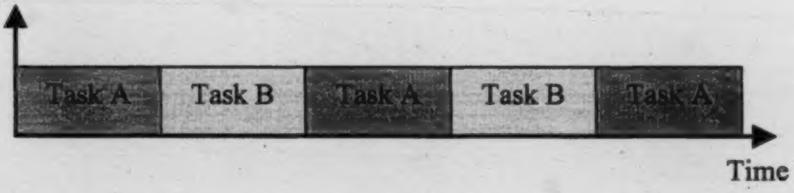

Figure 3-8

A typical block design fMRI paradigm with alternating presentations of Task A and Task B.

It is also possible to use single events as stimuli rather than blocks. Again the length of time between events needs to be much greater than the time taken for the hemodynamic response to reach its maximum and return to baseline. This type of study is called event-related fMRI and is more difficult to perform due to its need for very accurate timing between the stimulus presentation software and the MRI scanner data acquisition [28]. A typical block design will alternate the cognitive task with an appropriate control task. A well-designed control task will contain all on the cognitive components of the task being evaluated except for the particular operation being tested. For example a memory task that requires a motor response may be alternated with a control task that also requires the subject to make a decision and perform a motor response. If a pure rest control task were used instead the resulting activation would contain memory, motor, and a decision component. Therefore, by choosing an appropriate control task particular cognitive components can be included or excluded from the final results. The length of the paradigm is determined by the magnitude of the BOLD response for that particular task. For cognitive tasks that elicit a large BOLD response such as motor cortex tasks and visual tasks fewer alternating blocks, or events, are needed to reach a statistically significant threshold. Tasks that are very subtle such as memory, or attention, may require longer experiments before it is possible to find a significant correlation between the voxel intensity and the paradigm.

3.4.2 Paradigm Delivery and Response Collection

Many fMRI paradigms require the participant to see, hear, touch, or respond to certain stimuli, which is not straightforward in the confines of the MRI environment. Potential problems with fMRI experiments include acoustical noise, which can reach 120 dB during some EPI sequences, difficulty with the volunteer seeing the stimulus from within the magnet bore, movement of the subject during performance of the task, and the danger posed by any metallic objects around MRI machines. Although many commercial vendors supply different hardware packages for paradigm delivery we will only cover briefly the systems in place at the University of Alberta NMR Facility. Auditory communication is maintained via a set of earphones that serve both to transmit auditory information and dampen the acoustic noise of the scanner. The delivery of visual stimuli takes place via a projector located outside the magnet room which projects directly onto an opaque screen located within the magnet bore (MRA Inc. Pittsburgh, PA). With a mirror attached to the RF coil the volunteer can view any DVD, VHS, cable TV, or computer controlled software via this screen. Responses made from within the magnet bore can be collected using four fiber optic switches connected to a PC in the control room. These switches transmit single ASCII characters that can be recorded by many available stimulus presentation software packages such as SuperLab (Cedrus, San Pedro, CA), E-Prime (Psychology Software Tools Inc. Pittsburgh, PA) or Authorware (Macromedia Inc. San Francisco, CA)

3.4.3 Data Collection

The most common method of data collection is single-shot echo-planar imaging. EPI has several advantages over other imaging methods. The speed of EPI data acquisition is unsurpassed by other imaging methods. Therefore, it is possible to obtain more data points per given time and follow the BOLD signal change at a higher temporal resolution. A second advantage of the speed of EPI is that the time needed to acquire an image is usually much faster than physiological motion such as cardiac, respiratory, or head motion during the experiment. This allows EPI to effectively freeze in plane motion, however motion can still occur between images, which as we will see later must be dealt with during the analysis stage. Some typical parameters for an EPI based fMRI experiment at 1.5T are a repetition time, TR, of 3 seconds, an echo time of 50ms, and thirty 3mm slices at an in plane resolution of 3 x 3 mm. The repetition time determines the final temporal resolution of the experiment. For every TR, one volume of thirty images is collected in this case. The echo time, TE, determines how much T2* weighting there will be in the images. As we saw in Chapter 2, T2* contrast results from local inhomogeneities in the magnetic field. The local inhomogeneities that we are interested in are those resulting from paramagnetic deoxy-Hb that makes BOLD contrast possible. Therefore it is advantageous to maximize the BOLD contribution by optimizing TE. If a very short TE is chosen there will be no time for T2* contrast to develop. If TE is too long then the signal-to-noise ratio may be compromised due to excessive decay. The optimal value of TE is approximately equal to the value of the local T2*. Most BOLD studies at 1.5T are carried out with echo times near this value in the range of 50-60ms. The increased magnetic susceptibility effects at higher fields dephase the signal much faster; therefore, echo times are reduced to 25-40ms. Voxel dimensions also affect the signal-to-noise ratio in the images. In general, the smaller the voxel the fewer the number of spins it contains and thus SNR is proportional to the voxel volume. However, the BOLD SNR also decreases with very large voxels. If the voxel is larger than the expected BOLD activation region then partial volume averaging decreases the total BOLD signal from that voxel. Large voxels also contain signal with large differences in precession frequency resulting from large local field inhomogeneities. This difference in frequency causes the spins to be out of phase very quickly and the voxel will have a lower signal intensity than if the spins were in phase. The resulting artifact from large voxel dephasing is referred to as signal dropout. Signal dropout is most significant in areas of steep magnetic field inhomogeneities such as the frontal sinuses, orbits, temporal bones, and structures near the base of the brain.

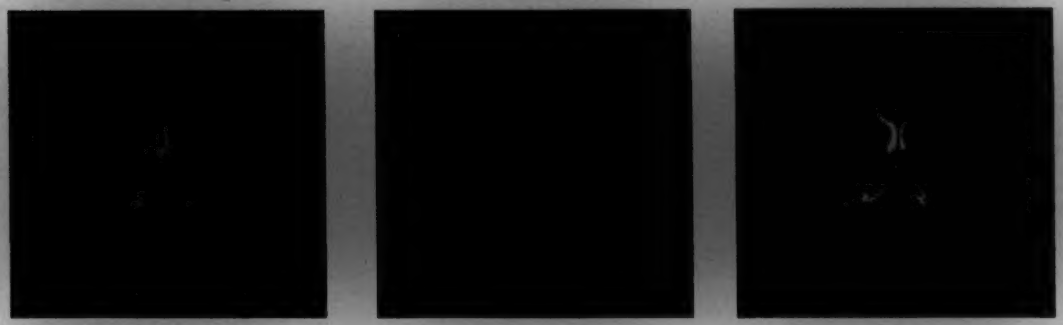

(a) *(b)* *(c)*

Figure 3-9

Echo Planar Images taken at three different resolutions and echo times at 1.5T (a) 64x64 matrix, 3.4x3.4mm in plane resolution, TE = 50ms, (b) 128x128 matrix, 1.7x1.7mm in plane resolution, TE = 50ms, and (c) 256x2565 matrix, 0.85x0.85mm in plane resolution, TE = 98ms.

3.5 References

1. Kety, S. and Schmidt, C. (1948), *The Nitrous Oxide Method for the Quantitative Determination of Cerebral Blood Flow in Man: Theory, Procedure and Normal Values.* Journal of Clinical Investigation, 27: 476-483.
2. Glass, H. and Harper, A. (1963), *Measurement of Regional Cerebral Blood Flow in Cerebral Cortex of Man Through Intact Skull.* British Medical Journal, 1: 593.
3. Fox, P., et al. (1984), *A Non-Invasive Approach to Quantitative Functional Brain Mapping with* $H_2^{15}0$ *and Positron Emission Tomography.* Journal of Cerebral Blood Flow and Metabolism, 4: 329-333.
4. Ogawa, S. and Lee, T.M. (1990), *Magnetic Resonance Imaging of Blood Vessels at High Fields: In Vivo and In Vitro Measurements and Image Simulation.* Magnetic Resonance in Medicine, 16(1): 9-18.
5. Afifi, A. Bergmen, R. (1997), *Functional Neuroanatomy: Text and Atlas 1st ed.* New York: McGraw-Hill, Health Professions Division.
6. Fix, J.D. (2002), *Neuroanatomy, 3rd ed.* Philadelphia: Lippincott Williams & Wilkins.
7. Clancy, J. McVicar, A. (2002), *Physiology and Anatomy: A Homeostatic Approach 2nd ed.* New York: Oxford University Press.
8. Frackowiak, R.S.J. et al. (1997), *Human Brain Function.* London: Academic Press.
9. Park, S. and Holtzman, P.S. (1992), *Schizophrenics Show Spatial Working Memory Deficits.* Archives of General Psychiatry, 49: 975-982.

10. Sweeney J.A. et al. (2000), *Neuropsychologic Impairments in Bipolar and Unipolar Mood Disorders on the CANTAB Neurocognitive Battery.* Biological Psychiatry, 48(7): 674-84.

11. McConkey, J. (1996), *The Anatomy of Memory: An Anthology.* New York: Oxford University Press.

12. Vanderwolf, C.H. and Cain, D.P. (1994), *The Behavioral Neurobiology of Learning and Memory: A Conceptual Reorientation.* Brain Research Reviews, 19: 264-297.

13. Baddely, A. (1992), *Working Memory.* Science, 255: 556-559.

14. Smith, E. and Jonides, J. (1997), *Working Memory: A View From Neuroimaging.* Cognitive Psychology, 33: 5-42.

15. Fox, P.T. and Raichle, M.E. (1986), *Focal Physiological Uncoupling of Cerebral Blood Flow and Oxidative Metabolism During Somatosensory Stimulation in Human Subjects.* Proceeding of the National Academy of Sciences USA, 83: 1140-1144.

16. Lou, H.C. et al. (1987), *The Concept of Coupling Blood Flow to Brain Function: Revision Required?* Annals of Neurology, 22: 289-297.

17. Iadecola, C. (1993), *Regulation of the Cerebral Microcirculation During Neural Activity: Is Nitric Oxide the Missing Link?* Trends in Neuroscience, 16: 206-214.

18. Deyoe, E. et al. (1994), *Functional Magnetic Resonance Imaging (fMRI) of the Human Brain.* Journal of Neuroscience Methods, 54: 171-187.

19. Pauling, L. and Coryell, C.D. (1936), *The Magnetic Properties and Structure of Hemoglobin, Oxyhemoglobin, and Carbonmonoxyhemoglobin.* Proceedings of the National Academy of Sciences USA, 22: 210-216.

20. Thulborn, K. (1982), *Oxygenation Dependence of the Transverse Relaxation Time of Water Protons in Whole Blood at High Field.* Biochimica et Biophysica Acta, 714: 265-270.

21. Fox, P.T. et al. (1988), *Nonoxidative Glucose Consumption During Focal Physiologic Neural Activity.* Science, 241: 462-464.

22. Ogawa, S. et al. (1993), *Functional Mapping by Blood Oxygen Level Dependant Contrast Magnetic Resonance Imaging: A Comparison of Signal Characteristics with a biophysical model.* Biophysics Journal, 64: 803-812.

23. Buxton, R. (2002), *Introduction to Functional Magnetic Resonance Imaging: Principles an Techniques.* Cambridge University Press.

24. Lai, S. (1993), *Identification of Vascular Structures as a Major Source of Signal Contrast in High Resolution 2D and 3D Functional Activation Imaging of the Motor Cortex at 1.5 T.* Magnetic Resonance in Medicine, 30: 387-392.

25. Gati, J.S. et al. (1997), *Experimental Determination of the BOLD Field Strength Dependence in Vessels and Tissue.* Magnetic Resonance in Medicine, 38: 296-302.

26. Menon, R.S. (1995), *BOLD Based Functional MRI at 4 Tesla Includes a Capillary Bed Contribution: Echo-planar Imaging Correlates with Previous Optical Imaging using Intrinsic Signals.* Magnetic Resonance in Medicine, 33: 453-459.

27. Krüger, G. et al. (2001), *Neuroimaging at 1.5T and 3.0T: Comparison of Oxygen Sensitive Magnetic Resonance Imaging.* 45: 595-604.

28. Buckner, R.L. et al. (1996), *Detection of Cortical Activation During Averaged Single Trials of a Cognitive Task Using Functional Magnetic Resonance Imaging.* Proceedings of the National Academy of Sciences (USA), 93: 14878-14883.

Chapter 4

Bipolar Disorder

4.1 Introduction

Bipolar disorder (manic-depressive illness) is a psychiatric disorder that affects approximately 1% of the general population [1]. Classified as a mood disorder, bipolar disorder is marked by a characteristic mood cycle that alternates from mania, where subjects are energetic and outgoing, to severe depression. Both depression and mania impact the patient by affecting mood, cognition, and behavior. Bipolar disorder has a severe economic impact on the health care system worldwide. In a 1990 survey, the World Health Organization identified bipolar disorder as the sixth leading cause of disability among people aged 15-44 years [2]. In 1991, the economic cost of bipolar disorder in the United States was estimated to be $45 billion [3]. A recent study has shown that the economic burden of mental illness as a whole in Canada reaches $14.4 billion annually [4]. Bipolar Disorder also has major social implications with respect to mortality and suicide rates. Compared with the general population those suffering from bipolar disorder have a mortality rate that is 2-3 times greater and at least 25% of patients attempt suicide [5,6].

4.2 Causes and Epidemiology

There is no single known cause of bipolar disorder, however, it is known to be a heritable illness. The likelihood of developing mood disorders is greatly increased for first-degree relatives of bipolar patients compared to first-degree relatives of people without psychiatric illness [7]. In addition to genetic influences the impact of life stresses, especially to those who are already at higher risk, may also play a role in the development of the disorder [8]. Although bipolar disorder can present at virtually any time across the life span, it is most often diagnosed between the ages of 18 and 24 [9]. Men and women appear equally affected by the disorder; however, women may be more prone to the depressive symptoms than men [10].

4.3 Clinical Features and Diagnosis

Like other mental illnesses, bipolar disorder is diagnosed based on the symptoms, course of illness, and family history. The diagnostic criteria for bipolar disorder are described in the Diagnostic and Statistical Manual for Mental Disorders, fourth edition, (DSM-IV) [11]. There are two major classifications of bipolar disorder: bipolar I and bipolar II. Bipolar I disorder involves recurrent episodes of depression and mania whereas bipolar II disorder consists of depression alternating with milder episodes of mania known as hypomania. Data from family studies of bipolar disorder suggest that bipolar II is the more common form of the disorder [12]. If four or more episodes of the illness occur within a 12-month period the person is said to have rapid-cycling bipolar disorder. Sometimes symptoms experienced by patients can meet both the criteria for depression and mania simultaneously. In these cases they are said to have mixed-episode bipolar disorder. The particular classification has implications in the treatment and long-term course of the illness. Table 4-1 shows some of the common symptoms of depression and mania in patients suffering from bipolar disorder.

Symptoms	
Depression	Mania
- Feeling worthless, helpless or hopeless - Loss of interest or pleasure - Change in appetite - Trouble sleeping - Decreased energy or fatigue - Poor concentration	- Excessively high or elated mood - Unreasonable optimism or elated mood - Hyperactivity or racing thoughts - Decreased sleep - Decreased attention span - Irritability

Table 4-1

Common symptoms associated with depression and mania.

4.4 Treatment

The treatment for bipolar disorder involves the use of a class of medications known as mood stabilizers. Mood stabilizers function to reduce the amplitude of deviations from normal mood to both the depressive and manic states. The most common treatment for bipolar disorder is lithium long-term symptom reduction. Other medications have recently been applied to the management of bipolar disorder that are equally or more effective than lithium for treatment of specific stages or classifications of the disorder. Some of these new medications include the anti-epileptic drugs valproic acid and carbamazapine.

4.4.1 Lithium

The history of lithium as a psychiatric medication can be traced back to the 1880's when Aulde and Lange used it for the treatment of recurrent depressive episodes [13,14].

However, it wasn't until the 1950's when lithium was first used to treat the symptoms of bipolar disorder [15]. Lithium is now well established as a mood stabilizer and has indications for treatment of the manic phase, depressed phase, and for maintenance treatment of bipolar disorder. Unfortunately, lithium has a narrow therapeutic index in which the optimal steady state plasma levels occur in the range 0.6 to 1.2 mEq/L [16]. At or above therapeutic levels some patients may find the side effects of lithium intolerable. These side effects include weight gain, tremors, muscle weakness, nausea, stomachaches, diarrhea, excessive thirst, frequent urination, and thyroid abnormalities. Long-term use may also be a contributing factor to kidney disease [17].

The mechanism of action of lithium is complex and not well understood but has been hypothesized to include membrane transport systems, neurotransmitter receptor regulation, second messenger signaling, protein kinase C (PKC) regulation, and gene expression [18]. Of the possible mechanisms for lithium's action, second messenger signaling is regarded as one of the most important. The theory that describes lithium's proposed action on second messenger systems is described by the inositol-depletion hypothesis shown in Figure 4-1 [19, 20].

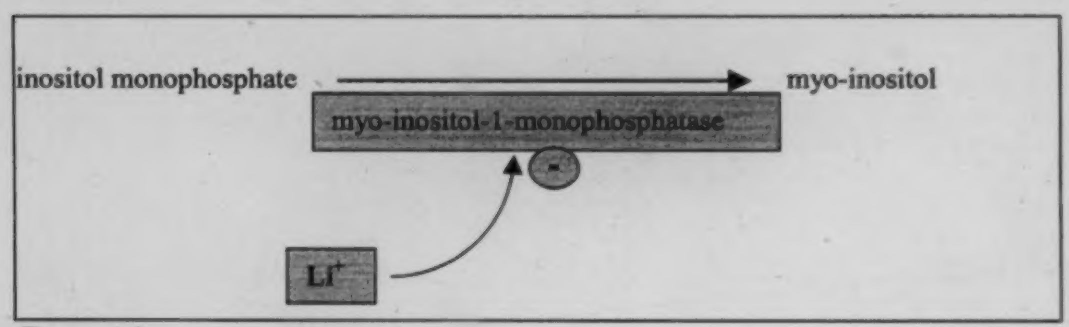

Figure 4-1

The inositol-depletion hypothesis.

The inositol-depletion hypothesis proposal began with the work of Alison and Stewart who were able to show that administration of lithium caused a reduction of *myo*-inositol (MI) concentrations and an accumulation of inositol-1-phosphateses (I-1-P) in the cerebral cortex of the rat [21,22]. Furthermore, the use of lithium ex vivo was shown to result in an accumulation of I-1-P that was greatly accentuated by agonists of receptors coupled to the phosphatidylinositol (PI) cycle [19]. Based on these finding Berridge proposed the inositol-depletion hypothesis which states that the effectiveness of lithium in the treatment of bipolar disorder is due to its ability to attenuate the PI second messenger pathway shown in Figure 4-2.

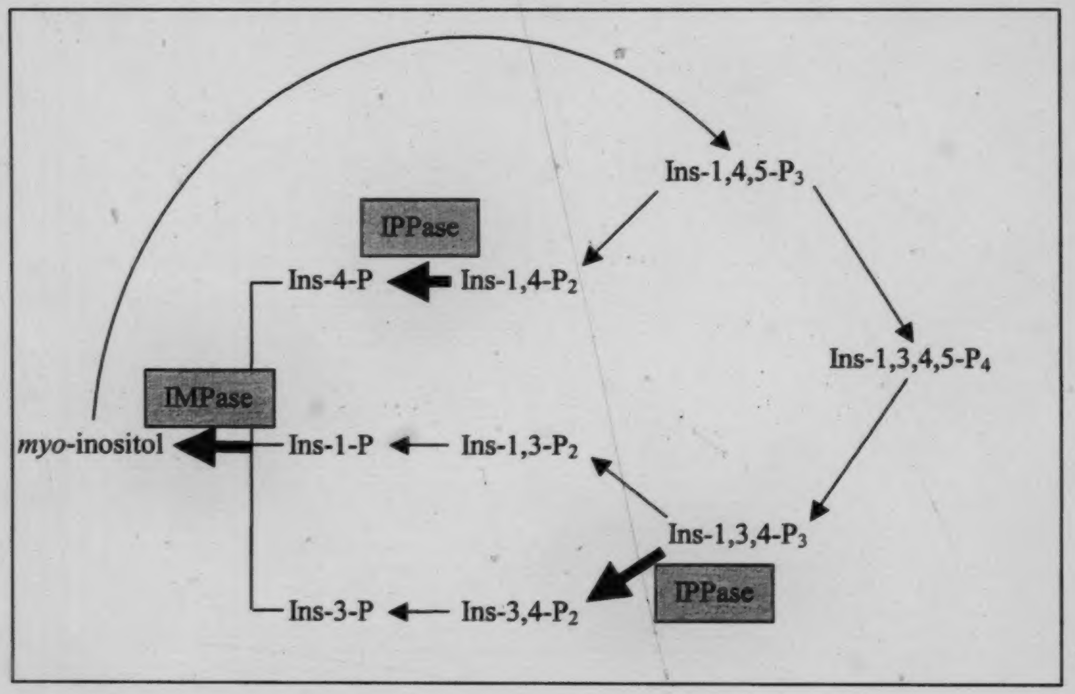
Ins-1,4,5-P3
IPPase
Ins-4-P
Ins-1,4-P2
Ins-1,3,4,5-P4
IMPase
myo-inositol
Ins-1-P
Ins-1,3-P2
Ins-1,3,4-P3
IPPase
Ins-3-P
Ins-3,4-P2

Figure 4-2

The phosphatidylinositol cycle (PI). The steps inhibited by the action of lithium are shown in large bold arrows.

Lithium acts on the PI cycle by a noncompetitive inhibition of the enzymes inositol monophosphatase (IMPase), and inositol polyphosphate-1-phosphatase (IPPase), which are used in the PI cycle to regenerate inositol phosphates [23,24]. Inhibition of inositol phosphate regeneration decreases the amount of myo-inositol available to be used in the production of membrane phospholipids required for signal transduction. The PI cycle is an intracellular second messenger system involving the increased phosphorylation of *myo*-inositol to D-*myo*-inositol 1,4,5-triphosphate (I-1,4,5-P_3) and the subsequent breakdown of I-1,4,5-P_3 to *myo*-inositol. I-1,4,5-P_3 acts as an intracellular second messenger that increases the release of calcium from intracellular stores within endoplasmic reticulum. The increase in free intracellular calcium concentrations that results from this action in turn increases neurotransmitter release. Thus, by decreasing the concentration of myo-inositol and attenuating the effectiveness of the PI cycle, lithium may decrease the amount of neurotransmitter released following a given level of receptor stimulation. Because of the uncompetitive nature of the inhibition of these enzymes it has been suggested that lithium will have a pronounced effect on systems undergoing a high rate of turnover [25]. Based on the proposed action of lithium on the PI cycle it has also been predicted that the underlying abnormality in bipolar patients is a hyper-responsive PI cycle in one or more regions of the brain.

4.5 Dextroamphetamine As A Model for Mania

Patients with bipolar disorder, and in particular those in the manic phase, tend to be difficult to study because they are often restless, unable to concentrate for long periods, and uncooperative. Therefore, the use of pharmacological agents as a model for mania is an important research tool for studying manic patients. Dextroamphetamine, shown in Figure 4-3, is often used as a model for mania because it induces some of the same subjective and physiological changes that are associated with the naturally occurring condition. Dextroamphetamine is thought to act by increasing the levels of catecholamine neurotransmitters such as dopamine and norepinephrine by inhibiting reuptake in the synaptic cleft, increasing their release, or binding directly to post synaptic receptors [26]. Pharmacological stimulation using dextroamphetamine has been shown to cause increases in elation, irritability, alertness, energy, restlessness, mental speed, and a decreased need for sleep, similar to the subjective changes related with mania [27].

Physiological changes associated with dextroamphetamine administration may also model the biological changes associated with bipolar disorder. Documented changes include, increased heart rate, blood pressure and dopamine activity. [27-28]. A useful model of mania should also respond to pharmacological treatment in the same way as the naturally occurring condition. Most studies, but not all [29] suggest that treatment with lithium attenuates the effects caused by dextroamphetamine stimulation in the same way it attenuates the symptoms of mania. Therefore, it appears to be a useful model of mania.

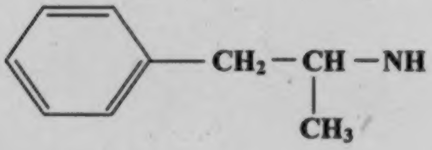

Figure 4-3

The chemical composition of dextroamphetamine.

4.6 The Effects of Dextroamphetamine on Cerebral Blood Flow and Metabolism

Neuroimaging studies using PET and SPECT have resulted in mixed findings concerning the effects of dextroamphetamine on cerebral glucose metabolism (CGM) and cerebral blood flow (CBF) in humans. Studies have found significant decreases [30], non-significant changes but a trend toward decreased CBF and CGM [31,32], and both an increase or decrease in CM and CBF in areas innervated by dopamine pathways [33]. An increase in global cerebral glucose metabolism has also been reported but only with very high doses of dextroamphetamine (1mg/kg) [34].

Functional magnetic resonance imaging studies evaluating the effects of dextroamphetamine have also been inconclusive. Using an auditory and visual stimulus it was found that the effect of dextroamphetamine in control subjects was a small reduction in the extent of sensory-induced activation [35]. In a group analysis dextroamphetamine increased BOLD signal during a task with increasing working-memory load that approached working-memory capacity in the right prefrontal cortex. However, the effect of dextroamphetamine on performance and on signal change varied across individuals. Dextroamphetamine improved performance only in those subjects who had relatively low working-memory capacity at baseline, whereas in the subjects who had high working-memory capacity at baseline, it worsened performance. In subjects whose performance deteriorated, signal change was greater than that in subjects who had an improvement in performance. This data demonstrate that even in normal subjects the behavioral and neurophysiologic effects of dextroamphetamine are not homogeneous [36]. Finally using a tone discrimination task and a right hand finger-tapping task it was found that the number of voxels activated after 20 mg of dextroamphetamine significantly increased the number of activated voxels in the left and right primary auditory cortices during the tone discrimination task and increased the number of activated voxels in the ipsilateral primary sensorimotor cortex and right middle frontal area during the motor task [37].

4.7 Neuroimaging Studies of Bipolar Disorder

There is relatively little information linking the functional pathophysiology of bipolar disorder as it relates to the use of neuroimaging techniques. Potential problems arise with a diverse patient population that may be depressed, manic, or exhibit symptoms of both.

Also, because of the difficulty recruiting cooperative manic patients most functional studies have focused on the bipolar depression. Functional neuroimaging studies of bipolar disorder have primarily used PET or SPECT imaging to evaluate CGM or CBF respectively. Using ^{18}[F] fluorodeoxyglucose (FDG)-PET to evaluate global CGM, depressed bipolar patients have been reported to exhibit increased [38], decreased [39], or the same [40] resting rate of glucose metabolism. In mania, whole brain glucose metabolism has been shown to be similar in bipolar patients and healthy comparison subjects [39,41]. Studies of regional glucose metabolism have generally shown that decreased prefrontal cortical glucose metabolism occurs during depression, and that a corresponding increase may occur in mania, although this is less clear [42]. Using SPECT to evaluate global CBF most studies have reported no changes associated with mania or depression compared with healthy controls [43,44] although a single study reported an increase in CBF associated with mania [45]. Regional CBF changes have been consistently reported for bipolar depression similar to those seen in unipolar depression. In general, decreased blood flow or perfusion is seen in frontal and temporal regions particularly in the left hemisphere [42]. These results further confirm the findings of decreased glucose metabolism in these areas. By contrast there are no consistent findings in the few studies relating cerebral blood flow abnormalities to the manic phase of bipolar disorder. In three studies it was found that there was no difference [46], increased basal ganglia and temporal blood flow [47], and also a decrease in blood flow to temporal and frontal areas [48].

4.8 References

1. Kessler, R.C. et al. (1994), *Lifetime and 12-Month Prevalence of DSM-III-R Psychiatric Disorders in the United States.* Archives of General Psychiatry, 51: 8-19.
2. Murray, C.J.L. and Lopez, A.D. (1996), *The Global Burden of Disease: A Comprehensive Assessment of Mortality and Disability, Injuries, and Risk Factors in 1990 and Projected to 2020.* Cambridge, MA. Harvard School of Public Health on Behalf of the World Health Organization and the World Bank. Harvard University Press.
3. Woods, S. (2000), *The Economic Burden of Bipolar Disease.* Journal of Clinical Psychiatry, 61 (Supplement 13): 38-40.
4. Steven, T. and Joubert, N. (2001), *The Economic Burden of Mental Health Problems in Canada.* Chronic Diseases in Canada, 22 1:18-23.
5. Fogarty, F. at al. (1994), *Mania.* Acta Psychiatrica Scandinavica, Supplement 376: 16-23.
6. Strakowski, S.M. (1996), *Suicidality in Mixed and Manic Bipolar Disorder.* American Journal of Psychiatry, 153: 674-676.
7. Gurling, H. (1995), *Linkage Findings in Bipolar Disorder.* Nature Genetics, 10: 8-9.
8. Post, R.M. (1992), *Transduction of Psychosocial Stress Into the Neurobiology of Recurrent Affective Disorder.* American Journal of Psychiatry, 149: 999-1010.
9. Health Canada (2002), *A Report on Mental Illnesses in Canada.* Ottawa, Canada.

10. Arnold L.M. et al. (2000), *Mixed Mania in Women.* Comprehensive Psychiatry, 41: 83-87.

11. American Psychiatric Association (1994), *Diagnostic and Statistical Manual for Mental Disorders, fourth edition (DSM-IV).* Washington, DC, American Psychiatric Press.

12. Simpson, S.G. (1993), *Bipolar II: The Most Common Phenotype?* Journal of Clinical Psychopharmacology, 13: 42-47.

13. Aulde, J. (1887), *The Use of Lithium Bromide in Combination With Solution of Potassium Citrate.* Medical Bulletin (Philadelphia), 9: 35-39.

14. Lange, C. (1886), *Om Periodiske Depressionstilstande og deres Patogenese.* Copenhagen, Denmark. Jacob Lunds Forlag.

15. Cade, J.F.L. (1949), *Lithium Salts in the Treatment of Psychotic Excitement.* Medical Journal of Australia, 36: 349-352.

16. Timmer, R. and Sands, J. (1999), *Lithium Intoxication.* Journal of the American Society of Nephrology, 10(3): 666-674.

17. Harvard University, (2001), *General Review – Bipolar Disorder.* Harvard Mental Health Letter, 17(11).

18. Lenox, R. et al. (1998), *Neurobiology of Lithium: An Update.* Journal of Clinical Psychiatry, 59(Supplement 6): 37-43.

19. Berridge, M. (1982), *Lithium Amplifies Agonist-Dependant Phosphatidylinositol Responses in Brain and Salivary Glands.* Biochemistry Journal, 206: 587-595.

20. Berridge, M. (1989), *Neural and Developmental Actions of Lithium: A Unifying Hypothesis.* Cell, 59: 411-419.

21. Alison, J. and Stewart, M. (1971), *Reduced Brain Inositol in Lithium Treated Rats.* Nature, 233:267-268.

22. Alison, J. et al. (1976), Biochemistry and Biophysics Research Communications, 71: 664-670.

23. Hallcher, L.M. and Sherman, W.R. (1980), *The Effects of Lithium Ion and Other Agents on the Activity of Myo-Inositol-1-Phosphatase From Bovine Brain.* Journal of Biological Chemistry, 255: 10896-10901.

24. Majerus, P.W. et al. (1988), *Inositol Phosphates: Synthesis and Degradation.* Journal of Biological Chemistry, 263: 3051-3054.

25. Berridge, M. and Irvine, R. (1989), *Inositol Phosphates and Cell Signalling.* Nature, 341: 197-205.

26. Moore, K.E. (1977), *The Actions of Amphetamine on Neurotransmitters: A Brief Review.* Biological Psychiatry, 12: 451-62.

27. Jacobs, D. and Silverstone, T. (1986), *Dextroamphetamine-Induced Arousal in Human Subjects as a Model for Mania.* Psychological Medicine, 16: 323-329.

28. Diehl, D.J. and Gershon, S. (1992), *The Role of Dopamine in Mood Disorders.* Comprehensive Psychiatry, 33: 115-20.

29. Silverstone, P.H. et al. (1998), *Lithium Does Not Attenuate the Effects of D-Amphetamine in Healthy Volunteers.* Psychiatry Research, 79(3): 219-26.

30. Wolkin, A. et al. (1987), *Effects of Amphetamine on Local Cerebral Metabolism in Normal and Schizophrenic Subjects as Determined by Positron Emission Tomography.* Psychopharmacology, 92: 241-246.

31. Mathew, R. and Wilson, W. (1985), *Dextroamphetamine-Induced Changes in Regional Cerebral Blood Flow.* Psychopharmacology, 87: 298-302.

32. Kahn, D. et al. *Dissociated Effects of Amphetamine on Arousal and Cortical Blood Flow in Humans.* Biological Psychiatry, 25: 755-767.

33. Devous, M. et al. (2001), *Regional Cerebral Blood Flow Response to Oral Amphetamine Challenge in Healthy Volunteers.* Journal of Nuclear Medicine, 42: 535-542.

34. Vollenweider, F.X. et al. (1998), *Effects of High Amphetamine Dose on Mood and Cerebral Glucose Metabolism in Normal Volunteers Using Positron Emission Tomography (PET).* Psychiatry Research, 83: 149-62.

35. Howard, R.J. et al. (1996), *Functional Echo-Planar Brain Imaging Correlates of Amphetamine Administration to Normal Subjects and Subjects With The Narcoleptic Syndrome.* Magnetic Resonance Imaging, 14: 1013-1016.

36. Mattay, V.S. et al. (2000), *Effects of Dextroamphetamine on Cognitive Performance and Cortical Activation.* Neuroimage, 12: 268-275.

37. Uftring, S.J. et al. (2001), *An fMRI Study of the Effect of Amphetamine on Brain Activity.* Neuropsychopharmacology, 25: 925-935.

38. Bauchsbaum, M.S. et al. (1986), *Frontal Cortex and Basal Ganglia Metabolic Rates Assessed by Positron Emission Tomography with [^{18}F]2-deoxyglucose in Affective Illness.* Journal of Affective Disorders, 10: 137-152.

39. Baxter, L.R. et al. (1985), *Cerebral Metabolic Rates for Glucose in Mood Disorders: Studies with Positron Emission Tomography and Flourodeoxyglucose F 18.* Archives of General Psychiatry, 42: 441-447.

40. Cohen, R.M. et al. (1989), *Evidence for Common Alterations in Cerebral Glucose Metabolism in Major Affective Disorders and Schizophrenia.* Neuropsychopharmacology, 2: 241-254.
41. Baxter, L.R. et al. (1989), *Reduction of Prefrontal Cortex Glucose Metabolism Common to Three Types of Depression.* Archives of General Psychiatry, 46: 243-250.
42. Strakowski, S.M. et al. (2000), *Neuroimaging in Bipolar Disorder.* Bipolar Disorders, 2: 148-164.
43. Silfverskiöld, P. et al. *Regional Cerebral Blood Flow in Depression and Mania.* Archives of General Psychiatry, 46: 253-259.
44. Tutus, A. et al. (1998), *Changes in Regional Cerebral Blood Flow Demonstrated by Single Photon Emission Computed Tomography in Depressive Disorders: Comparison of Unipolar vs. Bipolar Subtypes.* Psychiatry Research, 83: 169-177.
45. Rush, A.J. et al. (1982), *Cerebral Blood Flow in Depression and Mania.* Psychopharmacology Bulletin, 18: 6-7.
46. O'Connell, R.A. et al. (1989), *Single Photon Emission Computed Tomography (SPECT) with [*^{123}*I]IMP in the Differential Diagnosis of Psychiatric Disorders.* Journal of Neuropsychiatry and Clinical Neuroscience, 1: 145-153.
47. O'Connell, R.A. et al. (1995), *Single Photon Emission Computed Tomography of the Brain in Acute Mania and Schizophrenia.* Journal of Neuroimaging, 5: 101-104.
48. Rubin, E. et al. (1995), *Regional Cerebral Blood Flow in Mood Disorders IV: Comparison of Mania and Depression.* Psychiatry Research, 61: 1-10.

CHAPTER 5

Analysis of Functional MRI Data

5.1 Introduction

The ultimate goal of any functional MRI study is to determine the regions of the brain that are activated or deactivated with a particular task, medication, or condition. However, the magnitude of the BOLD response is sufficiently small that changes in neuronal activation cannot be detected without the use of statistical analysis techniques. These analysis techniques are quite often based on a linear model of the expected response known as the general linear model, GLM. However, before these techniques can be applied the data must be processed to increase the statistical power and validity of the final analysis. Corrections are made for gross movement during the experiment and differences in anatomical size and shape between subjects to ensure that the analysis is carried out at the same spatial location within a single subject and across subjects. Although many software packages exist for the analysis of functional data sets this chapter will focus on the theory used in SPM99, which is the software package implemented at the University of Alberta in the Center for Magnetic Resonance Evaluation of Human Function and Disease [1]. See Appendix A for exact steps for analyzing an example data set using SPM.

The entire process of analysis of functional MRI data sets consists of three distinct steps. Pre-processing to prepare the data for statistical analysis, statistical analysis itself, and finally the results must be interpreted and displayed.

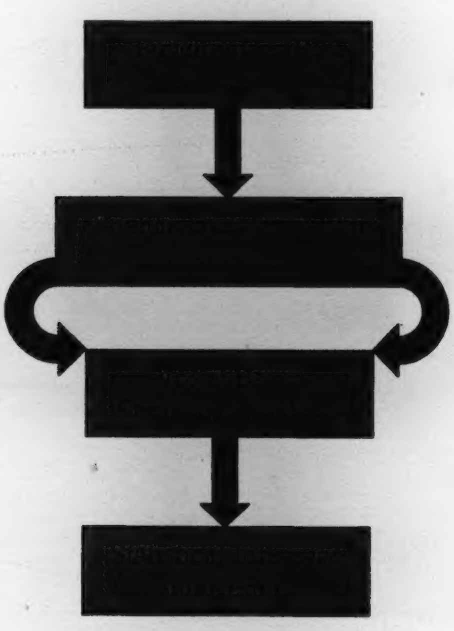

Figure 5-1

The major steps involved in the analysis of fMRI data.

5.2 Image Pre-Processing

Functional MRI images are pre-processed in several independent steps. Each step involves a mathematical manipulation of the images designed for a specific purpose to be described in the following sections.

5.2.1 Motion Correction (Realignment)

Echo-planar imaging can obtain images fast enough to freeze subject motion during image acquisition. However, there is still a possibility that the subject may move between each subsequent image. Subject movement causes individual voxels to contain information from slightly different anatomical locations over the course of a functional MRI experiment. For example, a voxel at the edge of the ventricles may contain brain in one image and cerebral spinal fluid in the following image if the subject has moved. Subject motion can cause one of two separate effects on an fMRI time series. First, if the subject movement is correlated with the functional task then the change in image intensity caused by the motion may result in pixels that falsely appear activated after analysis. Second, if the movement does not correlate with the task in any way then the motion increases the noise and reduces the sensitivity to task related activation [2]. Although these effects have opposing consequences, they both function to reduce the statistical power for detecting true activation.

To correct for these problems, the images are realigned so that all the images are matched to the first image in the time series. In three dimensions, any spatial transformation can be expressed by six parameters. Rotations can be described by the parameters pitch, roll, and yaw, and similarly translations can be described by x, y, and z. This type of rigid body transformation is known as the affine transformation. Realignment is accomplished by computing the sum of squares of the difference in these parameters between the image at time *t* and the reference image, typically the first image in the series [3]. Minimizing the sum of squares by iteratively rotating and translating the target volume by smaller and smaller amounts results in the closest possible match between the reference and target images.

The rigid body (affine) transformation can be written in matrix form:

$$\begin{pmatrix} x_1 \\ y_1 \\ z_1 \\ 1 \end{pmatrix} = \begin{pmatrix} A \end{pmatrix} \begin{pmatrix} x_0 \\ y_0 \\ z_0 \\ 1 \end{pmatrix} \qquad (5\text{-}1)$$

where the matrix *A* can be any of the following to implement a translation, or rotation (Θ, Φ, Ω in radians) about the x, y, and z axes.

$$\begin{pmatrix} 1 & 0 & 0 & x_{trans} \\ 0 & 1 & 0 & y_{trans} \\ 0 & 0 & 1 & z_{trans} \\ 0 & 0 & 0 & 1 \end{pmatrix}$$

$$\begin{pmatrix} 1 & 0 & 0 & 0 \\ 0 & \cos(\Theta) & \sin(\Theta) & 0 \\ 0 & -\sin(\Theta) & \cos(\Theta) & 0 \\ 0 & 0 & 0 & 1 \end{pmatrix}, \begin{pmatrix} \cos(\Phi) & 0 & \sin(\Phi) & 0 \\ 0 & 1 & 0 & 0 \\ -\sin(\Phi) & 0 & \cos(\Phi) & 0 \\ 0 & 0 & 0 & 1 \end{pmatrix}, \begin{pmatrix} \cos(\Omega) & \sin(\Omega) & 0 & 0 \\ -\sin(\Omega) & \cos(\Omega) & 0 & 0 \\ 0 & 0 & 1 & 0 \\ 0 & 0 & 0 & 1 \end{pmatrix}$$

5.2.2 Spatial Normalization

For functional MRI analysis involving multiple subjects a common image space is needed to account for individual differences in size, shape, and anatomy. Individual functional images are therefore normalized to a standard image template using an automated normalization algorithm. The Talairach and Tournoux atlas is an anatomical atlas based on the analysis of a single human brain [4]. This atlas was the first to use a cartesian coordinate system to localize both anatomical landmarks as well as cytoarchitectonic labels such as those described by Brodmann [5]. The MNI305 was the first MRI based template created at the Montreal Neurological Institute [6]. First, they took 241 normal MRI scans, and manually matched landmarks to equivalent positions on the Talairach atlas. They then took 305 normal MRI scans and used an automated 9 parameter linear algorithm to match the brains to the average of the 241 brains that had been matched to the Talairach atlas. From this they generated an average of 305 brain scans, the MNI305. The current standard MNI template that is implemented in SPM is the International Brain Mapping Consortium – 152, or ICBM152, which is the average of 152 normal MRI scans that have been matched to the MNI305 using a 9 parameter affine transform. Although the ICBM-152 template is supplied with SPM and other functional imaging software many researchers prefer to report results in coordinates based on the Talairach and Tournoux stereotaxtic atlas. The MNI template approximates the atlas described by Talairach and Tournoux but they are not exactly the same size or shape. When reporting results from SPM analysis a conversion must be made from MNI space to report the results in terms of the Talairach atlas.

The normalization of functional images takes place in two separate steps. The first is to apply a 12-parameter affine transformation that maps the target image to the template. This transformation is more robust than the realignment stage in that it includes 3 scaling parameters, and 3 skew parameters in addition to the 6 rigid body parameters. These extra parameters increase the accuracy of the registration at the expense of increased computational time. Second a non-linear spatial transformation is applied where the deformations are defined by a linear combination of three-dimensional discrete cosine transforms (DCT) [7]. Without suitable constraints the non-linear mapping of one image to another would be ill posed. Part of this problem lies in the fact that there is nothing to force the transformation to have a unique solution to map an image to the template. Therefore, the DCTs used are considered smooth spatial basis functions, which imposes the constraint that the deformations must be smooth. Smooth spatial deformations reduce the likelihood of the matching algorithm becoming unstable. Even with smooth transformations normalization does not have the ability to match every structure of the brain perfectly to the template.

a. Raw EPI Data *b. Normalized EPI Data* *c. ICBM152 Template*

Figure 5-2

Spatial normalization of echo-planar images obtained at 1.5T compared with the standard ICBM-152 template.

5.2.3 Spatial Filtering (Smoothing)

Smoothing is a mathematical process by which a voxel is averaged with surrounding voxels in an image. This process is also referred to as spatial filtering because applying a smoothing function reduces high frequency noise. The spatial extent of a filter is measured by the full width at half max (FWHM), which refers to the width of the filter at half of the maximum value. A filter with a larger FWHM smoothes the data to a greater extent by including more neighboring voxels in the computation. Smoothing is typically done for two reasons. First, applying a spatial filter can increase the signal to noise in the data. By averaging the signal intensity of a voxel with its neighbors there is a tendency for some of the noise to cancel. However, if a smoothing filter is selected which is larger than the expected region of activation then the BOLD signal can be reduced by volume averaging. Second, the statistical analysis implemented in SPM requires knowledge of the smoothness of the image data for Gaussian Random Field Theory (RFT) to be applied in the analysis stage [8]. RFT describes the corrections performed in neuroimaging analysis to compensate for the multiple comparisons performed when analyzing fMRI data at each voxel independently. In typical neuroimaging experiments a Gaussian filter with a 4-8mm full width half max (FWHM) is adequate to fulfill both requirements.

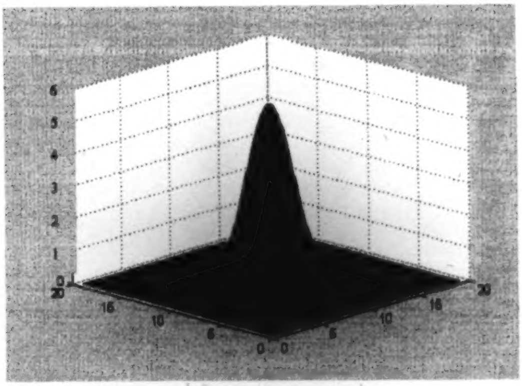

Figure 5-3

A three-dimensional Gaussian filter used to spatially smooth functional MRI images.

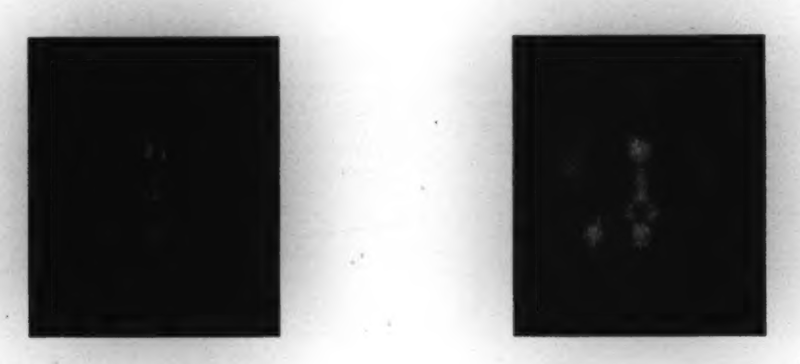

Figure 5-4

The effects of spatial smoothing on functional MRI images acquired at 1.5T.

a. Normalized EPI data, b. Smoothed, normalized EPI data

5.3 Statistical Parametric Mapping

Statistical parametric mapping, SPM, refers to a set of statistical processes used to test hypotheses about regionally specific effects in functional images [9]. Specifically, SPM does an analysis of variance for each voxel and then calculates a t-statistic based on a known statistical distribution, which approximates a Gaussian distribution. A three dimensional image of the t-statistics can then be used to display areas of the brain which are activated by a particular task or condition. Finally, an adjustment to the t-statistics is performed to correct for the multiple comparisons used to evaluate the large number of voxels in a typical image volume.

5.3.1 The General Linear Model

The general linear model, GLM, describes a model for the general pattern you expect to see in the data based on the specific paradigm and then attempts to model the response variable (in fMRI the response variable is the voxel intensity) as a linear combination of model functions and random noise [10]. The GLM can be written for a single voxel in a time series as:

$$Y(t) = \beta X(t) + \varepsilon(t) + c \tag{5-2}$$

where Y(t) is the data, X(t) is the model, β is the parameter estimate for that voxel, c is a constant that represents the baseline intensity of the data, and ε is the error in fitting the model to the data.

If the data is modeled as a simple boxcar of height one, then the model, X(t), consists of a series of ones and zeros where X(t) equals zero during rest, and X(t) equals one during the task. (i.e. 000001111100000…) The value of the parameter estimate, β, is the value that the boxcar model must be multiplied by to best fit the data and minimize the error, ε. A large value of β suggests that the voxel responds strongly to the model X(t).

A simple boxcar is rarely used as the model to represent the expected response of a voxel to a task or condition. It is more common to convolve the boxcar waveform with a hemodynamic response function, hrf. The hrf includes the time delay and dispersion, or blurring, of the response to a brief cognitive task [11]. The result of convolving the boxcar with the hrf is a model that more accurately represents the actual hemodynamic response.

5.3.2 Statistical Inference

To characterize a particular voxel as activated or not activated by the task, a statistic is needed which describes how unlikely the probability is, of obtaining a value for the parameter estimate equal to or greater than the current value of the parameter estimate. For a useful statistic to be generated, the parameter estimate, β, is compared with the uncertainty in its estimation, which results in a T-value.

$$T = \frac{\beta}{standard\_error(\beta)} \tag{5-3}$$

The T statistic describes how significantly the data is related to the model. For example if the value of β is large and the uncertainty in its measurement is small, then the T statistic will be large suggesting a strong relationship between the signal response of that voxel and the model. Given a threshold value of probability such as $p < 0.05$ a T statistic can be found from a T distribution which corresponds to this threshold. Voxels with a T statistic larger than this value are statistically significant and are considered activated by the task.

5.3.3 The Multiple Comparisons Problem

The preceding sections have all been concerned with the characterization of a single voxel using a statistical test. Therefore, for a single test we are assured that the probability of finding an activated voxel by chance is less than the threshold value. SPM, however, performs this test on a large number of voxels independently. Take, for example, a functional MRI image which contains 50 000 voxels. If we perform the same statistical test for all voxels independently, and use a threshold value of $p < 0.05$, then by chance alone we can expect that 5% of them will appear activated. This corresponds to 2500 voxels that are falsely activated because of the multiple comparisons we have performed.

A typical method used to correct for multiple comparisons is the Bonferroni correction. The Bonferroni correction assumes that all the observations are independent. In this technique, the threshold value chosen is divided by the number of comparisons. For such a large number of comparisons this corresponds to a very small p value of 0.000001 in our case. With such a small effective threshold the ability to detect true activation is greatly reduced and the possibility of rejecting true activation is high. Also, adjacent voxels are not necessarily independent. The point spread function of the imaging process means that a voxel will contain some information about the tissue immediately surrounding it, and the smoothing function that is typically applied during the pre processing stage means that adjacent voxels cannot be considered independent. Gaussian Random Field Theory has been developed to deal with the multiple comparisons problem as it relates to functional imaging [8]. The theory of Gaussian random fields takes into account both the significance of a particular activation and its spatial extent. The first step involves calculating how many resels there are in the image. A resel is referred to as a resolution element and is defined as a block of pixels of the same size as the FWHM of the smoothness of the image. In a 128x128 image smoothed by a filter 8x8 pixels FWHM (the smoothing that we applied) a resel is an 8x8 pixel block, and the number of resels in our image is (128 / 8) * (128 / 8) = 256. Note that the number of resels depends only on the number of pixels, and the FWHM. It is recommended that the smoothness of the image be at least twice the size of the voxel before applying the theory of Gaussian random fields. If the smoothness approaches voxel size then the corrected P value will approach those based on a Bonferroni correction [12]. For very small values of smoothing Gaussian random field theory can result in more stringent p values than a Bonferroni correction. The second step involves calculating the expected Euler characteristic of the image. The Euler characteristic can be considered to be the number of independent areas of activation after the image has been thresholded. From the Euler characteristic a calculation is made to correct for the required threshold value.

5.4 Group Analysis

After performing SPM analysis at a single subject level it is often required that inferences about generic activations in groups of subjects be performed. There are two major ways in which to make group statistical analysis using SPM: random and fixed-effect analysis [13]. The difference between the two methods relies on the computation of the error variance and has implications as to the conclusions one can make. One analysis is making conclusions about the typical characteristics of a population and the other about the average characteristics [14].

To construct a fixed-effect analysis all the subjects and or sessions are included in one design matrix similar to a first level analysis with one subject. SPM makes no distinction at this level with regards to subjects or sessions, therefore only the scan-to-scan variability is used in the calculation of the error variance. In this method the scan-to-scan variability is relatively small, and the number of degrees of freedom is large (number of scans minus the rank of the design matrix), which makes a fixed-effect analysis very sensitive to detecting group activation.

In contrast, a random effects analysis is performed in two stages that, taken together, account for both scan-to-scan variability and between subject variability. The first step is to perform an SPM analysis separately for each subject. This analysis creates a single image that contains the contrast of parameter estimates for the task (a con*.img image in SPM). The second step uses a standard statistical test such as a paired t-test, or single sample t-test with the contrast of parameter estimates created in the first level. In a random effects model the first level analysis controls for scan-to-scan variability and the second level analysis controls for subject-to-subject variability. By including both sets of variance we have greatly reduced the sensitivity to detecting activation. The degrees of freedom have fallen dramatically to the number of subjects minus one and the error variance is much larger. The low degrees of freedom can be overcome by adding more subjects to the analysis [14]. Experience here at the University of Alberta suggests that even with simple tasks such as motor cortex activation sample sizes of twelve to fourteen are needed before any group activation can be detected using a random effects analysis.

The difference in the error variance used in the analysis also implies differences in the conclusions that can be drawn from the results. A fixed-effect analysis in general tells you that the mean group response is to activate a particular area. This, however, can be the result of a single subject with very significant response or a true group response to the task. A random effects analysis tells us that the group's response is significant and also suggests that the sample of subjects shows a consistent activation to the task. This is a result that is generalizable to the population from which the subjects were chosen. Fixed-effect analysis, although not generalizable to the population, still remains an important tool in analysis of functional neuroimaging data. It is useful at times to use the results of a fixed-effect analysis as an exploratory analysis or to define functional regions of interest to be investigated using a random-effects model.

5.5 ROI Analysis

It is frequently useful to constrain analysis to predefined regions of interest or ROI's. An ROI based analysis is an important tool because you may have an apriori hypothesis as to an area of expected activation in a statistical parametric map. In such a case, to correct for multiple comparisons across the whole image is too conservative, as you are restricting your interest to a subset of the comparisons being made. Regions of interest can be specified based on two types of evidence. First, if you have a specific hypothesis about what areas of the brain you expect to be activated based on knowledge from other methods such as lesion studies or cortical mapping then it may be appropriate to limit your analysis to these areas. Second, evidence from previous fMRI, PET, or SPECT studies can be used to specify regions of interest. In this case, a particular task has been shown to produce activation only in a small number of areas; therefore, it is possible to limit analysis to these regions.

Regions of interest are constructed as analyze images that contain non-zero numbers in the specified area and zeros everywhere else. Using MRIcro it is possible to construct a region of interest in two ways. The first method is to use a high-resolution T1 weighted image and manually draw the area to be enclosed in the ROI on each slice of the volume of images using anatomical landmarks. The second method is to use an anatomical template image that has already been segmented into the various regions of the brain and simply specify which areas are to be included in the ROI. In MRIcro these templates take two forms. The first is a Brodmann map that corresponds roughly to the cytoarchitectonic labels described by Brodmann, and the second is an anatomical map that corresponds to the anatomical labeling system used in traditional neuroanatomy [15]. An example of the anatomical template is shown in Figure 5-5.

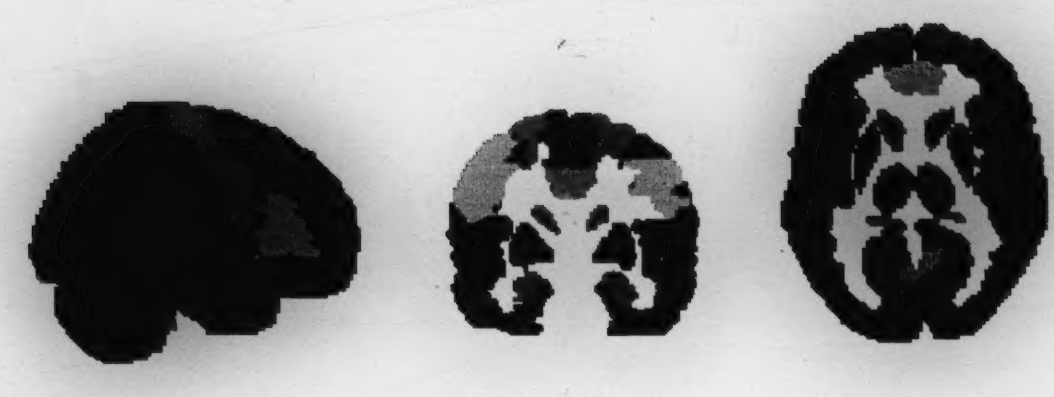

(a) Saggital View *(b) Coronal View* *(c) Transverse View*

Figure 5-5

The anatomical template used to create regions of interest for analysis. Each color represents a different anatomical region that can be isolated to create an ROI.

5.4 References

1. http://www.fil.ion.ucl.ac.uk/spm *Statistical Parametric Mapping (SPM).* Wellcome Department of Cognitive Neurology, University College London.
2. Friston, K.J. et al. (1996), *Movement-Related Effects in fMRI Time-Series.* Magnetic Resonance in Medicine, 35: 346-355.
3. Friston, K. J. et al. (1995), *Spatial Registration and Normalization of Images.* Human Brain Mapping, 2: 165-189.
4. Talairach, J. and Tournoux, P. (1988), *Co-Planar Stereotaxic Atlas of the Human Brain.* Thieme Medical, New York.
5. Brodmann, K. (1909), *Vergleichende Lokalisationslehre der Grosshirnrinde in ihren Prinzipien dargestellt auf Grund des Zellenbaues.* Barth, Leipzig.
6. Evans, A.C., Collins, D.L., Milner, B. (1992), *An MRI-Based Stereotaxtic Atlas From 300 Young Normal Subjects.* Proceedings of the 22nd Annual Symposium for the Society of Neuroscience, Anaheim. 408.
7. Ashburner, J. and Friston, K. J. (1999), *Nonlinear Spatial Normalization Using Basis Functions.* Human Brain Mapping, 7: 254-266.
8. Worsley, K.J. (1996), *A Unified Statistical Approach For Determining Significant Signals In Images Of Cerebral Activation.* Human Brain Mapping, 4: 58-73.
9. Friston, K.J. et al. (1995), *Statistical Parametric Maps In Functional Imaging: A General Linear Approach.* Human Brain Mapping, 2: 189-210.
10. Jezzard, P. et al. (2002), *Functional MRI: An Introduction to Methods.* Oxford University Press.

11. Friston, K.J., Jezzard, P., and Turner, R. (1994), *The Analysis of Functional MRI Time-Series.* Human Brain Mapping, 1: 153-171.
12. Worsley, K.J., and Friston, K.J. (1995), *Analysis of fMRI Time Series Revisited – Again.* Neuroimage, 2: 173-181.
13. Friston, K.J. et al. (1999), *Multisubject fMRI Studies and Conjunction Analysis.* Neuroimage 10: 385-396.
14. Friston, K.J. et al. (1999), *How Many Subjects Constitute a Study.* Neuroimage, 10: 1-5.
15. Tzourio-Mazoyer, N. et al. (2002), *Automated Anatomical Labeling of Activations in SPM Using a Macroscopic Anatomical Parcellation of the MNI MRI Single Subject Brain.* Neuroimage, 15: 273-289.

Chapter 6

Methods

6.1 Introduction

Before functional MRI techniques could be applied in a research study it was necessary to develop the infrastructure required to use this new technique. EPI BOLD sequences were developed and optimized at 1.5T for the detection of brain activation. Paradigm delivery systems were set up and tested so subjects in the magnet could see and hear the necessary visual and auditory stimuli required to perform cognitive tasks. It is also desirable for subjects to be able to make responses while performing the tasks in the confines of the MRI machine. Therefore, fibre-optic response buttons were installed and integrated with a stimulus presentation package (SuperLab Pro: Cedrus Inc, San Pedro CA) on a PC that would function to control the stimulus software and record subject response time and accuracy. Finally, cognitive tasks had to be developed to evaluate specific higher brain functions. These tasks were programmed in SuperLab Pro and tested both outside the magnet and inside the magnet. To fully integrate the paradigms with data collection each paradigm required specific timing modifications to ensure paradigm delivery and data collection were synchronized. Once completed each paradigm was then tested on several control subjects to ensure reliability and reproducibility in producing activation in the predetermined areas.

6.2 Development of Cognitive Tasks

Each of the cognitive tasks was chosen based on a search of the literature concerning fMRI studies in schizophrenia. Cognitive areas that patients suffering from schizophrenia activated abnormally were identified as regions of interest to investigate in bipolar disorder. Using fMRI, research has shown that schizophrenia patients have abnormalities relating to motor function [1], working memory [2-6], and verbal fluency or word generation [7-9]. Also, using a novel reaction time/spatial attention task we intended to evaluate any changes associated with the administration of these medications on the cognitive areas involved in mediating spatial attention.

6.2.1 Motor Task

The motor task, or finger-tapping task, involves rapidly tapping the index finger. There are two conditions for this experiment. The instruction 'STOP' or 'START' is given visually. When the 'STOP' instruction is given, subjects are instructed to lie very still and try not to move. When the 'START' instruction appears subjects respond by tapping the index finger as rapidly as possible in a controlled manner on a response button which will record each button press and continue tapping until the 'STOP' instruction appears again. Each condition (Rest or Tapping) is performed in four alternating blocks each lasting forty seconds. This experiment is done twice, once with the left hand and then again with the right hand. The task is illustrated in Figure 6-1.

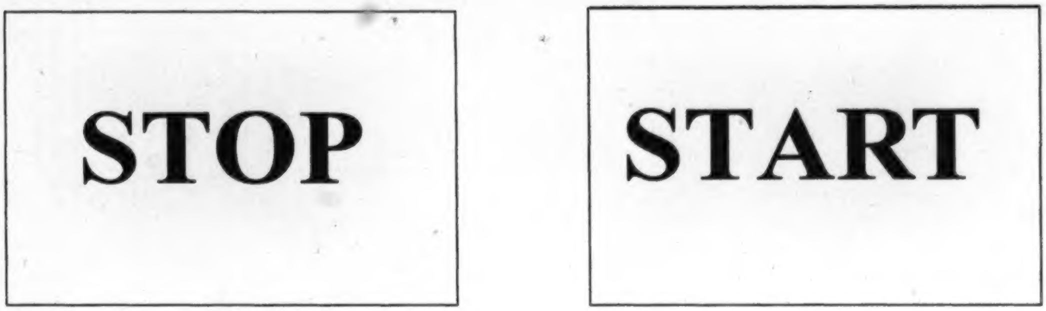

STOP

START

Figure 6-1

The instruction screens for the motor cortex fMRI experiment.

6.2.2 Word Generation Task

The word generation task involves two conditions. When the 'REST' instruction is given subjects are required to repeat the word 'REST' silently until another instruction is given. In the second condition a series of ten single letters randomly chosen from the alphabet are displayed at 4-second intervals. During the display of a single letter, subjects responded by thinking of as many words as possible that begin with that letter and repeating them silently until another letter is presented or the 'REST' instruction appears. This task can be seen in Figure 6-2. Each condition was performed for forty seconds total for each block. The experiment consisted of five alternating blocks of each condition beginning with 'REST'.

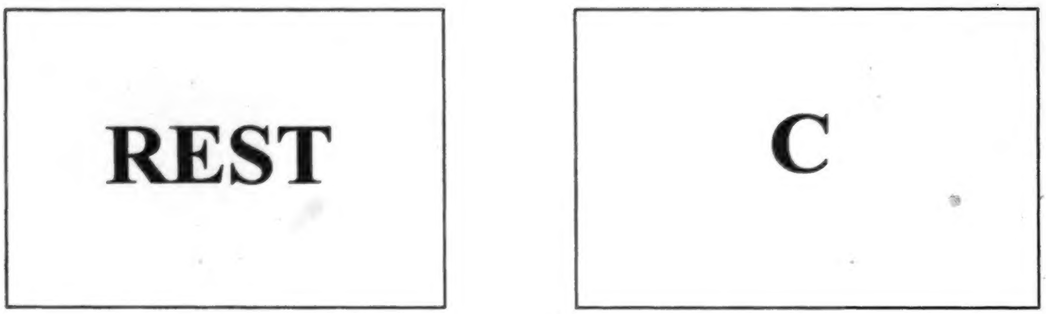

Figure 6-2

The experimental conditions used in the verbal fluency task.

6.2.3 Working Memory Task

The working memory task involves two conditions. In the first condition there is a series of ten arrows pointing to the left or to the right. Subjects respond by pressing the left or right button. In the second condition a two or five digit number is presented on the screen for four seconds with the instruction 'Remember this Number'. Immediately after a series of ten random single digits is presented. Subjects were asked to respond by pressing the button for yes if the single digit was in the memorized number, or by pressing the button for no if the single digit was not in the memorized number. Figure 6-3 gives a graphical representation of the task as seen by the subject in the MRI machine.

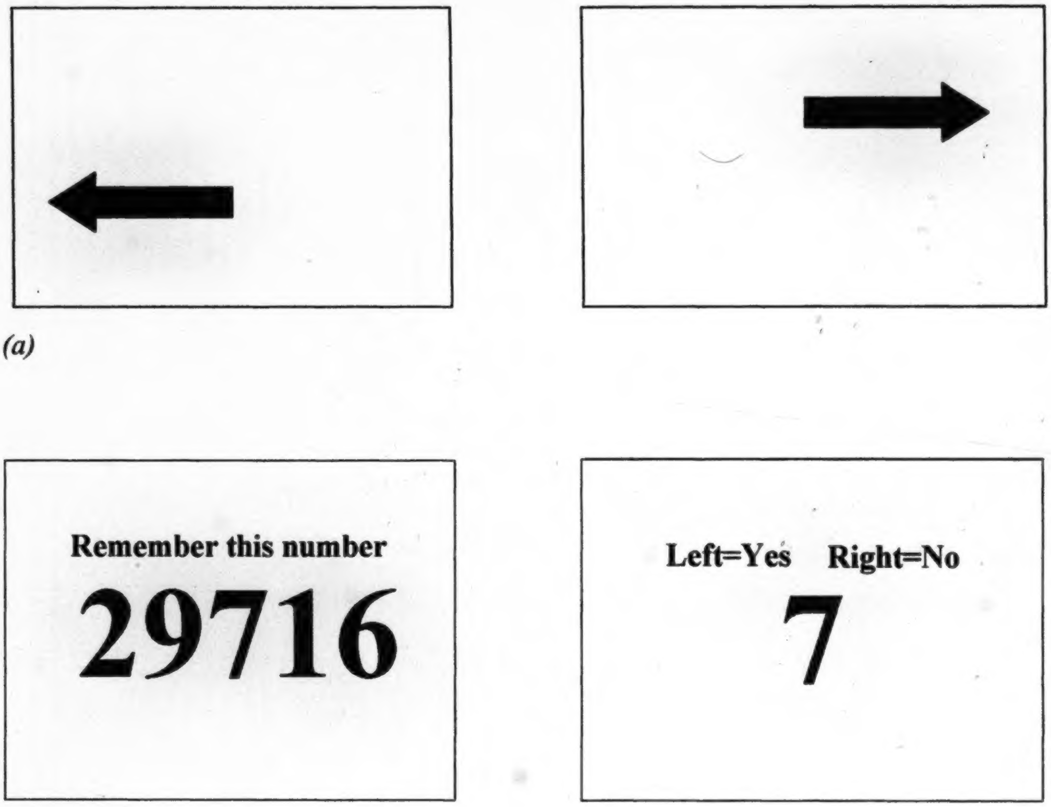
Remember this number
29716
Left=Yes
Right=No
7

(a)

(b)

Figure 6-3

The conditions used in the working memory task. (a) The control task, (b) The high working memory condition.

The working memory was the longest of all the tasks due to the delicate nature of the cognitive function being evaluated. In all, each of the three conditions was presented seven times in twenty-four second blocks pseuodorandomly arranged.

6.2.4 Reaction Time/ Spatial Attention Task

For this task, subjects were asked to respond as quickly as possible to a certain criteria. First, a black cross appeared on the screen. Soon after, the black cross would appear with a target. The target is a black square. Whenever the black cross and square appeared together subjects responded by pressing the button in their dominant hand as fast as possible. The delay between the appearance of the cross and the target was varied randomly from 300 – 1100ms. Approximately 10% of the trials were actually catch trials designed to ensure subjects were engaged in the task. In a catch trial another black cross appeared instead of the target and subjects were not supposed to respond in this case. Any responses to catch trials were considered errors. In this experiment two conditions of the reaction task were alternated to evaluate spatial attention. In the stationary condition the cross and square appeared in the same location. Therefore, subjects were responding to a visually attended location. In the second condition the target appeared a distance away from the cross. In this condition subjects were responding to an unattended visual location. A sample of the reaction task can be seen in Figure 6-4. This method of evaluating spatial attention was chosen because there is significant evidence that suggests that spatial attention is analogous to a mental spotlight that requires a certain connectivity to operate properly. In particular, the parietal lobe is involved in mediating the act of disengaging attention from its current location, the thalamus and midbrain are involved in the movement and engagement at its new location, and finally the prefrontal cortex is the executive control of this action [10,11]. This task was performed in ten alternating blocks of each condition, twenty-four seconds in duration each.

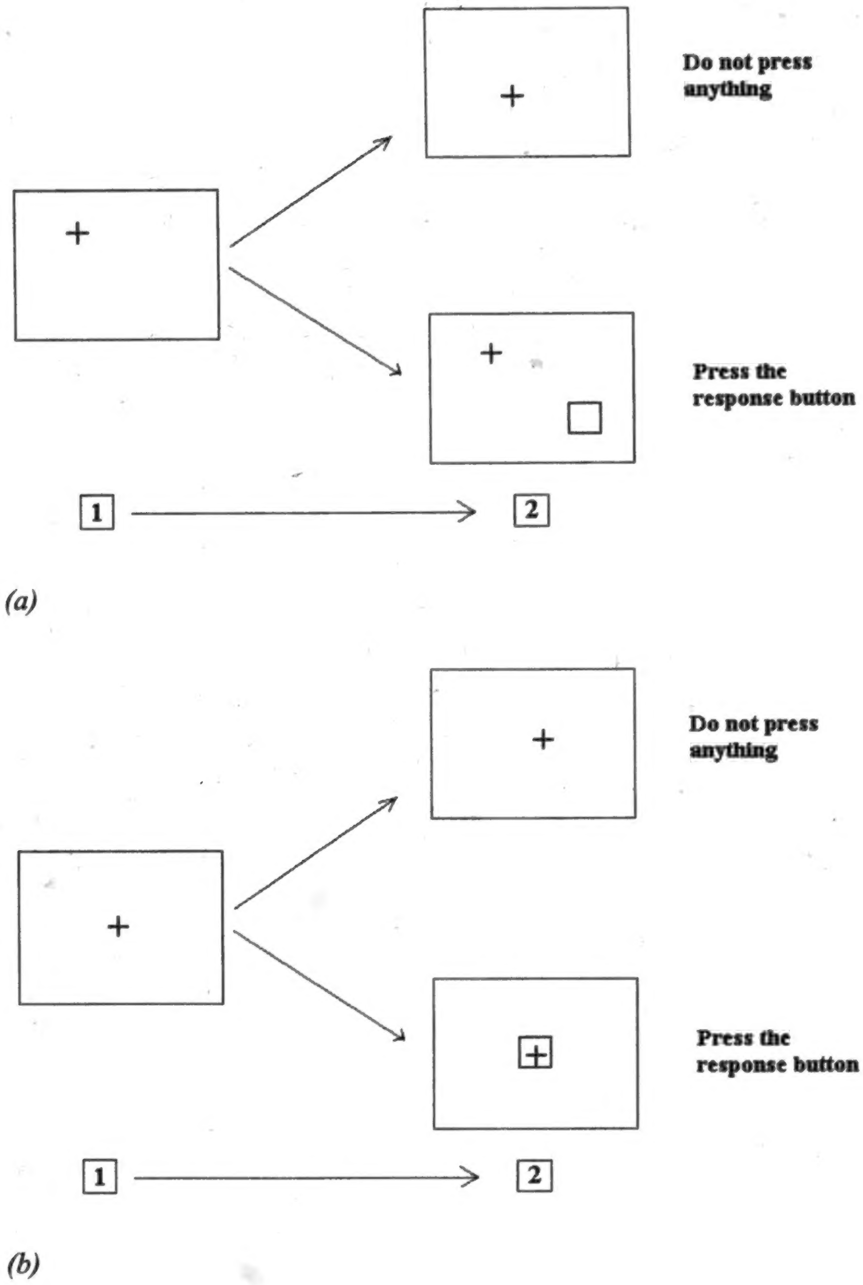
Do not press anything
Press the response button
1
2
(a)
Do not press anything
Press the response button
1
2
(b)

Figure 6-4

The tasks used in the reaction time / spatial attention task. (a) Responding to a visually unattended spatial location. (b) Responding to a visually attended spatial location

6.3 Study Design

The purpose of this study is to look at the effects of medications important in the treatment or pathophysiology of bipolar disorder on cerebral blood flow and brain activity in healthy volunteers using functional magnetic resonance imaging. In the context of this study we will examine the effects of dextroamphetamine and lithium independently, as well as the effects of lithium on the changes associated with dextroamphetamine stimulation. These three research questions are all important in understanding the pathophysiology of bipolar disorder. Lithium is the most common treatment available today for the treatment of bipolar disorder yet its underlying mechanism of action remains unresolved. With the use of fMRI we hope to find out if lithium has any global or regional effects on brain activity in healthy volunteers. Hopefully, with this knowledge a better understanding of lithium's action can be obtained. Dextroamphetamine is used as a model for mania, and therefore it is interesting to evaluate how dextroamphetamine affects cerebral blood flow and brain activity. Finally, because amphetamines are used as a model for mania it is important to know if the changes associated with its administration respond to the same pharmacological treatment as seen in mania. With this knowledge it may be possible to further validate or contradict the usefulness of amphetamine as a model for mania.

A double-blind placebo controlled study design was used. Subjects (N=18) came in on two occasions fourteen days apart. During the first day they were given a physical examination and then performed the first fMRI session, which lasted approximately forty-five minutes. During this session subjects performed four types of tasks: motor movement of the left and right hand, a working memory task, a reaction time task, and a verbal fluency task. Upon completion of the fMRI portion subjects were then administered a single oral dose of 25 mg dextroamphetamine and allowed to rest for 75 minutes. Previous research with dextroamphetamine suggests that the maximum subjective response to dextroamphetamine administration occurs approximately 120 minutes after ingestion [12]. Therefore, the timing was chosen so that the peak subjective response to dextroamphetamine would occur during the second fMRI session, which began immediately after the rest period. At the completion of day 1 volunteers were given 42 opaque green capsules containing either 300 mg of lithium or placebo (lactose powder), which were administered in a random manner so that each subject had a fifty-percent chance of receiving either medication. Subjects took three capsules daily for a total dose of 900 mg of lithium per day for the next fourteen days. On day fourteen the subjects returned and the fMRI sessions were repeated, again separated by administration of 25 mg dextroamphetamine and a delay of 75 minutes before the second fMRI session. The study design is illustrated in Figure 6-5.

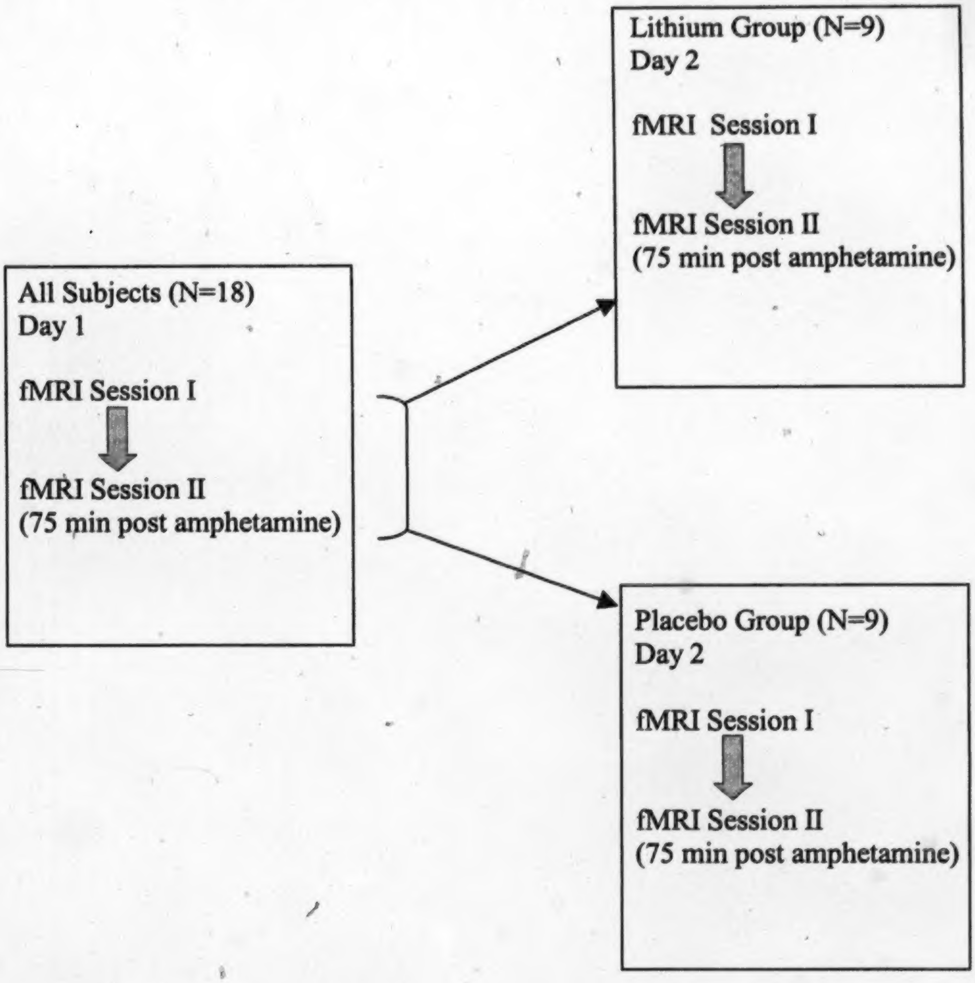
All Subjects (N=18)
Day 1
fMRI Session I
fMRI Session II
(75 min post amphetamine)
Lithium Group (N=9)
Day 2
fMRI Session I
fMRI Session II
(75 min post amphetamine)
Placebo Group (N=9)
Day 2
fMRI Session I
fMRI Session II
(75 min post amphetamine)

Figure 6-5

Double-blind placebo controlled study to look at the effects of lithium and amphetamines on cerebral blood flow and brain activity.

6.4 Subjects

Eighteen right-handed healthy volunteers were recruited through poster advertising from the university community to participate in the research study. Subject demographic data can be seen in Table 6-1.

Study Subjects (N = 18)	
Age	25.4 (± 6.51)
Sex	
Male	13
Female	5
Weight (lbs)	171.6 (± 22.2)

Table 6-1

Subject Demographic Summary (mean ± SEM).

To be included in the study, subjects were required to have no past or present history of psychiatric illness and no history of psychiatric illness in their immediate family (parents and/or siblings). Subjects that had used any recreational drugs in the past six months (one year for stimulants such as amphetamine) were also excluded. They were also screened at this time for any ondition requiring medication, or any physical illness that precluded the use of amphetamines. An MRI safety screen was performed to ensure safety in undergoing the MRI procedure. Subjects were required to fast from midnight the day prior to testing and were allowed only water during each session. Upon arrival they gave a detailed medical history to a physician who also performed a full physical examination prior to the start of the study. Ethics approval for the study was given by the ethics committee at the University of Alberta and all participants gave full informed consent.

6.5 Comparisons

In order to evaluate the three research questions proposed, comparisons were made based on two criteria: the number of activated pixels [13], and the change in BOLD intensity as measured using fMRI in anatomical regions of interest for each task [14]. Thus, we believe by measuring both the number of pixels and intensity in specific brain regions, we can most accurately measure any regional changes. Regions of interest for each task were generated based on a group analysis of all subjects. Table 6-2 shows the regions of interest identified for each task.

Using ROI based analysis to evaluate both the number of activated pixels and the BOLD intensity change we identified seven possible comparisons to evaluate the effects of dextroamphetamine shown in red, the effects of lithium shown in blue, the effects of lithium on dextroamphetamine shown in purple, and two control comparisons shown in yellow. The seven comparisons and a brief description of each are given in Figure 6-6 and Table 6-3.

Memory	Verbal	Motor	Reaction
Left, Right Inferior Parietal Lobule (IPL)	Left, Right Inferior Parietal Lobule (IPL)	Left, Right Inferior Parietal Lobule (IPL)	Left, Right Middle Occipital Gyrus (MOG)
Left, Right Superior Parietal Lobule (SPL)	Left, Right Superior Parietal Lobule (SPL)	Supplementary Motor Area (SMA)	Left, Right Superior Parietal Lobule (SPL)
Left, Right Dorsal Lateral Prefrontal Cortex (DLPFC)	Left, Right Dorsal Lateral Prefrontal Cortex (DLPFC)	Left, Right Inferior Frontal Gyrus (IFG)	Left, Right Lingual Gyrus (LG)
Left, Right Pre-Central Gyrus (PCG)	Left, Right Pre-Central Gyrus (PCG)	Left, Right Superior Temporal Gyrus (STG)	Precuneus (PRE)
Cingulate Gyrus (CING)	Cingulate Gyrus (CING)	Thalamus (THAL)	Cuneus (CUN)
Left, Right Inferior Occipital Gyrus (IOG)	Broca's Area (Broca's)	Left, Right Primary Sensorimotor Cortex (PSMC)	
Left, Right Inferior Frontal Gyrus (IFG)	Left, Right Superior Temporal Gyrus (STG)		
Left, Right Middle Frontal Gyrus (MFG)	Thalamus (THAL)		
Left, Right Superior Frontal Gyrus (SFG)	Supplementary Motor Area (SMA)		
Left, Right Insula (INS)			

Table 6-2

Regions of interest for each of the cognitive tasks.

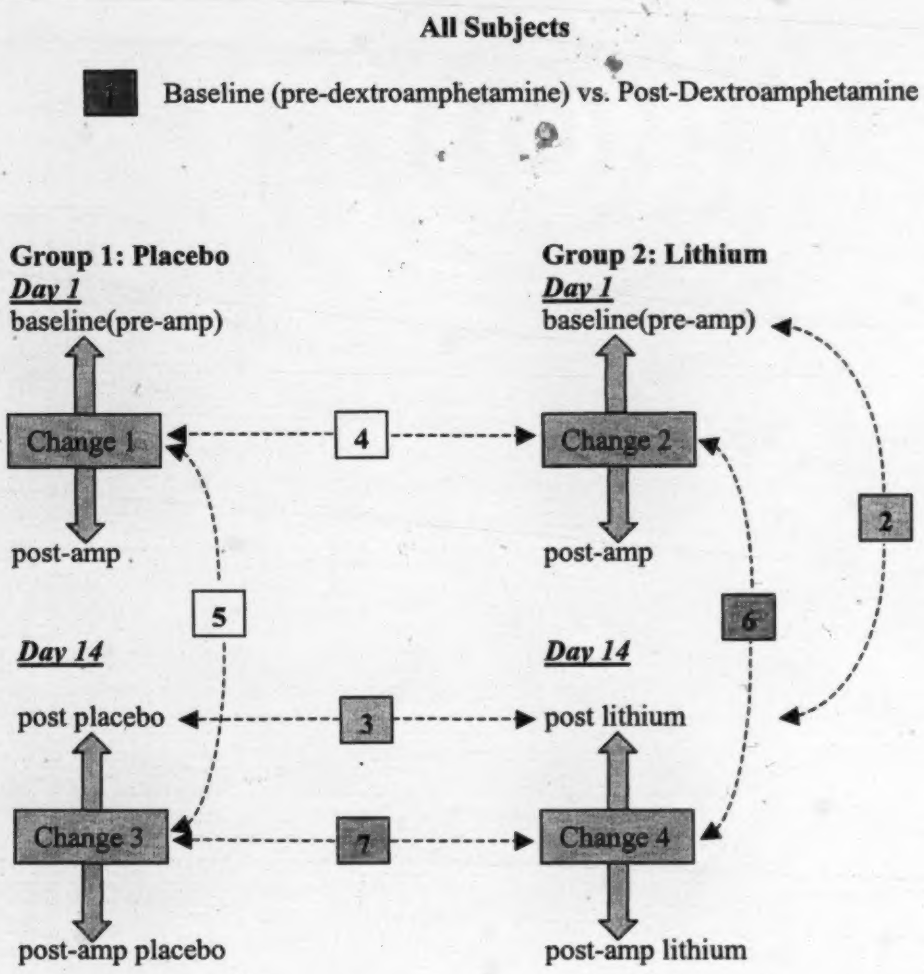
All Subjects
1
Baseline (pre-dextroamphetamine) vs. Post-Dextroamphetamine
Group 1: Placebo
Day 1
baseline(pre-amp)
Change 1
post-amp
Group 2: Lithium
Day 1
baseline(pre-amp)
Change 2
post-amp
4
2
5
6
Day 14
post placebo
Change 3
post-amp placebo
Day 14
post lithium
Change 4
post-amp lithium
3
7

Figure 6-6

The structure of the study based on the two groups, and the possible measurements of medication induced changes.

Effects of Amphetamines
1. Paired t-test: Pre vs. post amphetamine for all subjects.
Effects of Lithium
2. Paired t-test for group 2: Baseline vs. post lithium treatment.
3. Independent samples t-test of group 1 vs. group 2: post placebo treatment vs. post lithium treatment
Control Comparisons
4. Independent samples t-test of the change caused by amp **Change1** vs. **Change2.** Are there any differences between the groups before treatment.
5. Paired t-test of the change caused by amp **Change1** vs. **Change3**. Is there any difference between the first and second administration of amphetamine for the placebo group.
Effects of Lithium on Amphetamines
6. Paired t-test of the change caused by amp **Change2** vs. **Change4**. The change caused by amphetamine before vs. after lithium treatment.
7. Independent samples t-test of the change caused by amp **Change3** vs. **Change4.** The change caused by amphetamine after placebo compared with the change after lithium treatment.

Table 6-3

The seven comparisons to be made using ROI based analysis on the number of activated pixels and the BOLD signal intensity change.

6.6 Subjective and Physiological Measurements

Subjective and physiological measurements were taken from each volunteer before the first fMRI session, 75 minutes after amphetamine, and 120 minutes after amphetamine administration on both study days. Subjects were required to rate their feelings on anxiety, mood, alertness, physical well being, hunger, energy, concentration, irritability, mental speed, light headedness, and restlessness using a set of 100 mm visual analogue scales (VAS). A physician also measured blood pressure and heart rate at these intervals to evaluate physical changes associated with amphetamine administration.

6.7 Functional MRI Data Collection

All functional imaging was performed on a 1.5 T Siemens Sonata MRI scanner. Subjects were given earplugs and headphones to dampen the noise of the MRI machine and communication between the subject and operator was maintained using the same headphone system. Supports placed against the headphones were used to restrict subject motion during the MRI session. A mirror attached to the standard Siemens head coil allowed the participants to see the stimulus program via a digital projector system placed outside the MRI room and aimed at a translucent screen placed in the bore of the magnet (MRA Inc. Pittsburgh, Pennsylvania). All the cognitive tasks were programmed in SuperLab Pro (Cedrus Corp., San Pedro, California), which also collected response times and accuracy via 4 fibre optic response buttons held by the participant during the experiment (MRA Inc. Pittsburgh, Pennsylvania). Prior to the first fMRI session all participants were given the same instructions for the experiment, shown a demo of each task, and given an opportunity to practice the four experiments. The relevant MRI parameters for each of the tasks can be seen in Table 6-4.

	Motor	Memory	Reaction	Verbal
Echo Time	50 ms	50 ms	50 ms	50 ms
Repetition Time	5040 ms	4010 ms	4010 ms	4010 ms
Bandwidth per pixel	1502 Hz/pixel	1502 Hz/pixel	1502 Hz/pixel	1502 Hz/pixel
Matrix	128x128	128x128	128x128	128x128
Slice Thickness	3 mm	4 mm	4 mm	4 mm
Slices	30	30	30	30
Time Points	66	142	122	102
Block Design	4 on, 4 off	7 control, 7 low memory 7 high memory	10 on, 10 off	5 on, 5 off
Block Length	40.3 s	24.1 s	24.1 s	40.1 s
Total Time	5 min 21 s	9 min 29 s	8 min 9 s	6 min 49 s

Table 6-4

MRI parameters of interest for each of the experimental tasks.

6.8 Data Analysis

6.8.1 fMRI Data Pre-processing

All pre-processing steps were performed identically for all four tasks. Image transformation from Siemens IMA format to Analyze image format was performed offline using MRIcro [15]. Pre-processing and analysis was then performed using SPM99 [16]. Images were first re-oriented so that the anterior commissure and posterior commissure were aligned to match the required orientation in SPM. Realignment was performed using a 6-parameter rigid body transformation and a mean image was created of the entire time series for each data set. The mean image was then spatially normalized to the MNI template brain using a 12-parameter affine transformation with 12 non-linear iterations and 7 x 8 x 7 basis functions. The spatial transformations derived from normalizing the mean image to the template were then applied to the T2* weighted EPI functional images. After normalization, all volumes were resampled to 2 x 2 x 2 mm voxels using trilinear interpolation in space. Finally, all functional images were smoothed with an 8-mm full width at half-maximum isotropic Gaussian kernel to compensate for residual between subject variability and permit application of Gaussian random field theory to provide for corrected statistical inferences.

6.8.2 fMRI Single Subject Analysis (Voxel-wise Analysis)

Initial analysis was performed separately for each subject for each task. The model specified for each task was kept identical for all subjects and sessions to create identical design matrices. This is required when using the results from a first level analysis and applying them in any second level analysis. As part of this analysis three more pre-processing steps are performed using SPM99. First the data is high passed filtered to remove low-frequency drifts in the signal. The upper cut off period is different for each task and corresponds to roughly twice the experiment cycle. Specific values can be seen in Table 6-5. In addition, to remove high frequency noise the data was also low pass filtered using the hemodynamic response function (hrf). Furthermore, to remove effects due to global intensity fluctuations, the data was proportionally scaled to a global mean of 100. See Appendix A for notes on the use of global scaling in functional MRI studies.

	Memory	Motor	Reaction	Verbal
Cut off Period (s)	217	163	96	161

Table 6-5

Cut off period used to high pass filter the functional MRI data.

The time series for each data set was then analysed according to the general linear model. A fixed-response boxcar model was chosen to represent the data. The boxcar was then convolved with the hemodynamic response function. Convolving with the hrf will add a delayed onset, early peak, and late undershoot to the model to more accurately characterize the expected response. Results were finally obtained using a p-value of 0.05 corrected for multiple comparisons.

6.8.3 fMRI Group Analysis

Group analysis was performed by first constructing a fixed effects model for each task. All sessions for all subjects were included in this model to generate a group average activation map. The coordinates of the most significantly active voxels in the group results were transformed from MNI coordinates to Talairach coordinates and entered into the Talairach Daemon [17]. The Talairach Daemon takes a series of Talairach coordinates and returns the anatomical location from which the coordinates originate. An example of the Talairach Daemon's usage is given in Table 6-6.

Talairach Coordinates (x, y, z) **[53, 4, 42]**				
Level 1	Level 2	Level 3	Level 4	Level 5
Right Cerebrum	Frontal Lobe	Middle Frontal Gyrus	Gray Matter	Brodmann Area 6

Table 6-6

The anatomical description based on coordinates from the Talairach Atlas using the Talairach Daemon.

The anatomical areas output from the Talairach Daemon were then used to create regions of interest (ROI) for each task. ROI images were constructed using the automated anatomical labelling (AAL) template [18] available for use with MRIcro software. An example of the ROI image created for the left pre-central gyrus using MRIcro is shown overlaid on a T1 weighted structural MRI image in Figure 6-7.

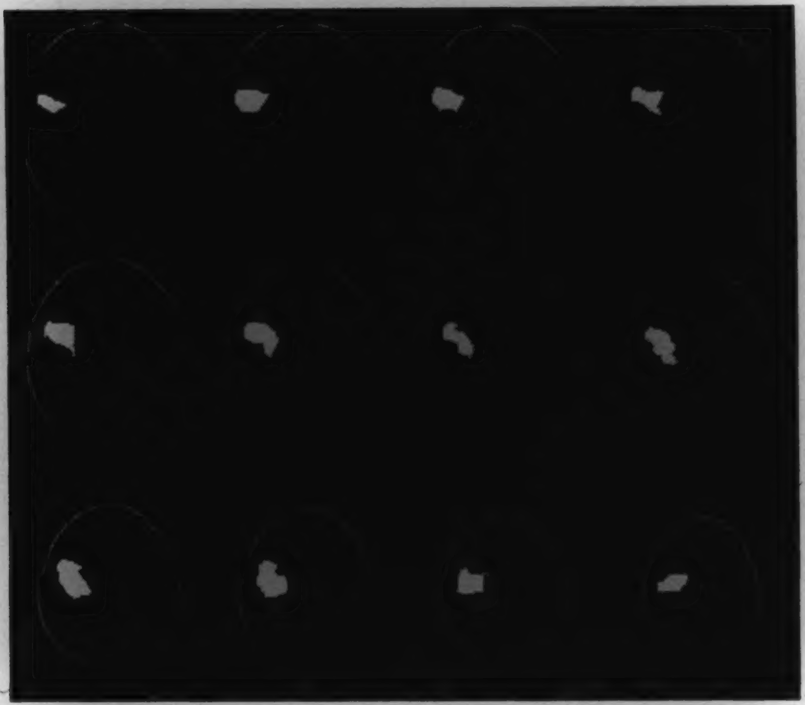

Figure 6-7

Anatomical ROI image defining the left pre-central gyrus created using the AAL template and MRIcro. Shown overlaid on a T1 weighted MRI image.

The number of activated pixels in each ROI for a particular task was calculated for each subject using the results from the single subject analysis and applying the small volume correction (SVC) in SPM [19]. A SVC is used because we have an apriori hypothesis as to the area of expected activation in the statistical parametric map based on the fixed effects analysis. In this case, to correct for multiple comparisons across the whole image is too conservative; the SVC gives results that allow the choice of appropriate thresholds given that you are restricting your investigation to a certain region of interest of defined shape and size. This is because both size and shape dictate how strict the correction for multiple comparisons must be. The number of significantly activated pixels was simply counted for each ROI and then analyzed using a conventional statistical program (Analyze It: Leeds, England) and paired t-tests for within group measures and independent sample t-tests for measures between groups.

The BOLD signal intensity change was also calculated based on regions of interest. The measure of BOLD signal intensity change used in SPM is referred to as the fitted response. The fitted response is calculated as a change in signal intensity expressed in percentage of whole brain mean. Because the global mean was scaled to 100 during the pre-processing stage, the height of an effect is the percentage signal change with respect to the global mean intensity of the scaled images. The fitted response was calculated using the MARSBAR toolbox for SPM [20] over a seven-voxel sphere centered on the most significantly active voxel in each ROI. The number of voxels over which the fitted response was calculated was kept small in order to minimize averaging over non-significant voxels [14]. The quantity used in the subsequent statistical calculations for BOLD signal intensity was the average fitted response calculated from the plateau portion of the hemodynamic response (eight seconds after stimulus origination until stimulus termination). Analysis was then performed using standard t-tests in the same fashion as was done in the analysis of the number of activated pixels for each ROI.

6.8.4 fMRI Response Data

Response and accuracy data was collected for the motor task, memory task, and reaction time task. Due to the nature of the word generation task no quantitative measures of performance could be obtained. For the motor task, the number of button presses was recorded during each forty-second epoch and averaged for that session. Dividing by the total time results in the frequency in Hertz subjects performed the tapping task. Standard t-tests were used to evaluate any changes in tapping frequency. Both accuracy and reaction time were recorded and entered into an analysis using t-tests to evaluate the memory task's three conditions, control, low working memory, and high working memory. In a similar manner reaction time and accuracy was measured for the attended visual location responses and the unattended visual location responses and analyzed.

6.8.5 Subjective and Physiological Measures

The behavioral changes, as measured using the VAS scales, and the physical changes, as measured by the heart rate and blood pressure, were analyzed using repeated measures ANOVA with the single factor, TIME (Before amphetamine, 75 minutes after amphetamine, and 120 minutes after amphetamine).

6.9 References

1. Schröder, F. et al. (1995), *Sensorimotor Cortex and Supplementary Motor Area Changes in Schizophrenia.* British Journal of Psychiatry, 167: 197-201.
2. Manoach, D.S. et al. (2000), *Schizophrenic Subjects Show Aberrant fMRI Activation of Dorsolateral Prefrontal Cortex and Basal Ganglia During Working Memory Performance.* Biological Psychiatry, 48: 99-109.
3. Menon, V. et al. (2001), *Functional Neuroanatomy of Auditory Working Memory in Schizophrenia: Relation to Positive and Negative Symptoms.* Neuroimage, 13: 433-446.
4. Callicot J.H. et al. (2000), *Physiological Dysfunction of the Dorsolateral Prefrontal Cortex in Schizophrenia Revisited.* Cerebral Cortex, 10: 1078-1092.
5. Manoach, D.S. et al. (1999), *Schizophrenic Subjects Activate Dorsolateral Prefrontal Cortex During a Working Memory Task, as Measured by fMRI.* Biological Psychiatry, 45: 1128-1137.
6. Honey, G.D. et al. (1999), *Differences in Frontal Cortical Activation by a Working Memory Task After Substitution of Risperidone for Typical Antipsychotic Drugs in Patients with Schizophrenia.* Proceedings of the National Academy of Sciences, 96: 13432-13437.
7. Curtis, V.A. et al. (1998), *Attenuated Frontal Activation During a Verbal Fluency Task in Patients with Schizophrenia.* American Journal of Psychiatry, 155: 1056-1063.

8. Frith, C.D. et al. (1995), *Regional Brain Activity in Chronic Schizophrenic Patients During the Performance of a Verbal Fluency Task.* British Journal of Psychiatry, 167: 343-349.
9. Yurgelun-Todd, D.A. et al. (1996), *Functional Magnetic Resonance Imaging of Schizophrenic Patients and Comparison Subjects During Word Production.* American Journal of Psychiatry, 153: 200-205.
10. Beauchamp, M.S. et al. (2001), *A Parametric fMRI Study of Overt and Covert Shifts of Attention.* Neuroimage, 14: 310-321.
11. Cabeza, R. and Kingstone, A. (2001), *Handbook of Functional Neuroimaging of Cognition.* Cambridge, Massachusetts: MIT Press.
12. Jacobs, D. and Silverstone, T. (1986), *Dextroamphetamine Induced Arousal in Human Subjects as a Model for Mania.* Psychological Medicine, 16: 323-329.
13. Uftring, S.J. et al. (2001), *An fMRI Study of the Effects on Amphetamines on Brain Activity.* Neuropsychopharmacology, 25: 925-935.
14. Mulderink, T.A. et al. (2002), *On The Use of Caffeine as a Contrast Booster for BOLD fMRI Studies.* Neuroimage, 15: 37-44.
15. Rorden, C. and Brett, M. (2000). *Stereotaxic Display of Brain Lesions.* Behavioural Neurology, 12: 191-200. (www.mricro.com)
16. SPM99 Welcome Department of Cognitive Neurology, University College London. (www.fil.ion.ucl.ac.uk/spm)
17. Lancaster, J.L. (1997), *The Talairach Daemon, A Database Server for Talairach Atlas Labels.* Neuroimage 5(4): S633.

18. Tzourio-Mazoyer N et al. (2002), *Automated Anatomical Labelling of Activations in SPM Using a Macroscopic Anatomical Parcellation of the MNI MRI Single Subject Brain.* Neuroimage, 15: 273-289.

19. Worsley, K.J. et al. (1996), *A Unified Statistical Approach For Determining Significant Signals in Images of Cerebral Activation.* Human Brain Mapping, 4: 58-73.

20. Brett, M. et al. (2002), *Region of Interest Analysis Using an SPM Toolbox.* [abstract] Presented at the 8th International Conference on Functional Mapping of the Human Brain, June 2-6, 2002, Sendai, Japan. Available on CD-ROM in Neuroimage, 16(2).

Chapter 7

Results

7.1 Introduction

The following chapter deals with the results obtained from an fMRI study of the effects of dextroamphetamine and lithium on cerebral blood flow and brain activity in healthy volunteers. The first section describes the results from subjective and physiological measurements taken from each volunteer at different time points during the study. These results are given to show that the dose of amphetamine given was sufficient to cause its known psychological and physical effects. The next section looks at the performance data from each of the tasks and how dextroamphetamine affected subject performance. Finally, the fMRI results are presented in the last section. The first part of this section shows group activation maps for each of the tasks to illustrate the various anatomical areas activated by each task. A representative time course from an individual subject is also given to show the response from a single activated pixel for each task. The second half of this section presents the ROI analysis of the effects of dextroamphetamine and lithium on the number of activated pixels and the magnitude of the BOLD response for the identified ROIs for each task.

7.2 Subjective and Physiological Measurements

Measurements before, 75 minutes after, and 125 minutes after dextroamphetamine administration show that heart rate increases significantly and continues to increase over the time span observed. Diastolic blood pressure also increased significantly in the same manner, however the systolic blood pressure increase has levelled off by 125 minutes post medication.

Physical Changes		
Heart Rate (beats per minute ± SD)		
Baseline	(t = 0)	66.2 ± 6
Pre fMRI	(t = 75 min)	70.9 ± 8
Post fMRI	(t = 125 min)	79.3 ± 11
Blood Pressure (mmHg ± SD)		
Systolic		
Baseline	(t = 0)	107.1 ± 12
Pre fMRI	(t = 75 min)	124.3 ± 14
Post fMRI	(t = 125 min)	122.9 ± 11
Diastolic		
Baseline	(t = 0)	78.1 ± 9
Pre fMRI	(t = 75 min)	84.1 ± 7
Post fMRI	(t = 125 min)	86.6 ± 5

Table 7-1

*The effects of dextroamphetamine on heart rate and blood pressure. *Blood pressure, both systolic and diastolic, was significantly higher for baseline vs. pre-fMRI, and baseline vs. post-fMRI, $p<0.05$. **Heart rate was significantly higher for baseline vs. post-fMRI, and pre-fMRI vs. post-fMRI, $p<0.05$.*

Using 100mm visual analog scales (VAS) subjects reported feeling significantly elevated levels of happiness ($F = 7.44$, $df = 53$, $p < 0.0015$), alertness ($F = 6.22$, $df = 53$, $p < 0.0038$), energy ($F = 11.88$, $df = 53$, $p < 0.0001$), speed of thoughts ($F = 9.80$, $df = 53$, $p < 0.0003$), light-headedness ($F = 6.60$, $df = 53$, $p < 0.0028$), and restlessness ($F = 5.25$, $df = 53$, $p < 0.0085$) for both baseline versus pre-fMRI (t = 75 minutes) and baseline versus post-fMRI (t = 125 minutes).

Subjective Changes	
Anxiety	--
Mood	↑
Alertness	↑
Physical Well Being	--
Hunger	--
Energy	↑
Concentration	--
Irritability	--
Mental Speed	↑
Light Headedness	↑
Restlessness	↑

Table 7-2

Amphetamine induced changes in subjective behaviour and being measured using VAS scales. ↑ indicates a significant change for baseline vs. pre fMRI ($t = 75$min), and baseline vs. post fMRI ($t = 125$min), -- indicates no significant change was found.

7.3 Quantitative Measures of Performance

The rate of finger tapping was recorded during performance of the motor task using SuperLab Pro (Cedrus, San Pedro: CA). Subject's performance was significantly increased after administration of amphetamine (Figure 7-1) for the non-dominant left hand ($p \leq 0.045$), but not the dominant right hand finger-tapping task ($p \leq 0.400$). For the reaction time task, reaction performance was also significantly better after dextroamphetamine (Figure 7-2) for both the attended visual responses and the unattended visual responses (Attended $t = 6.80$, $p \leq 0.0001$, Unattended $t = 6.81$, $p \leq 0.0001$). However, there was no significant difference in the number of errors (Errors $t = 1.77$, $p \leq 0.094$). Similarly, subjects performing the working memory task responded faster to all three conditions (Figure 7-3) after dextroamphetamine (Control $t = 2.85$, $p \leq$

0.008, 5 Digit Memory $t = 2.34, p \leq 0.0253$, 2 Digit Memory $t = 3.80, p \leq 0.0006$). The administration of dextroamphetamine had no effect on the number of errors incurred during the memory task (Errors $t = 1.09, p \leq 0.283$).

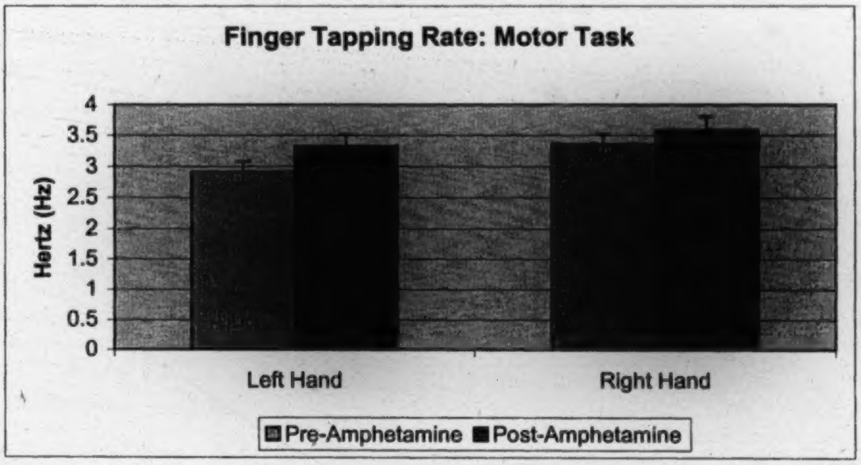

Figure 7-1

The average finger tapping rate (mean ± SE) for N = 18 subjects during performance of the left hand finger tapping task and right hand finger tapping task before and after dextroamphetamine.

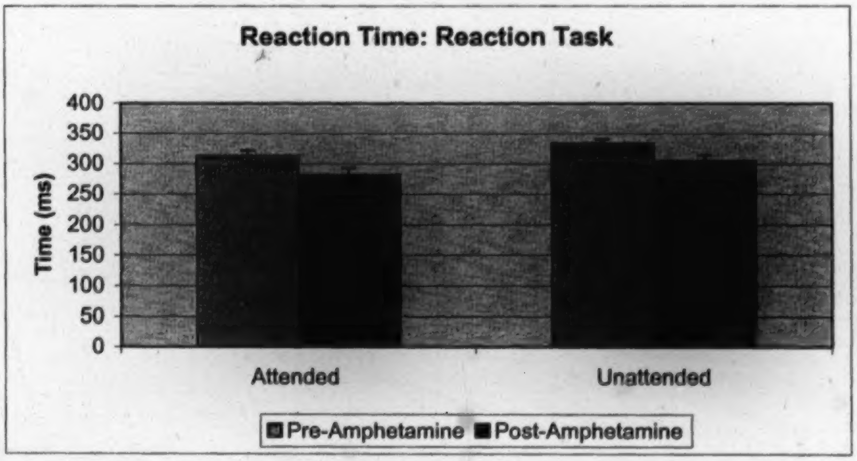

Figure 7-2

Reaction time measurements (mean ± SE) during performance of the reaction task for N = 18 subjects, pre and post dextroamphetamine.

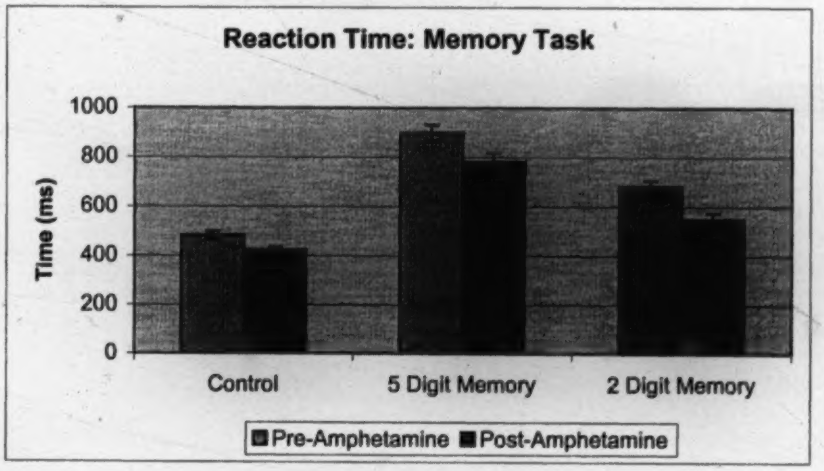

Figure 7-3

Reaction times for the memory task (mean ± SE) for N = 18 subjects, pre and post amphetamine.

7.4 Functional MRI Task Summary

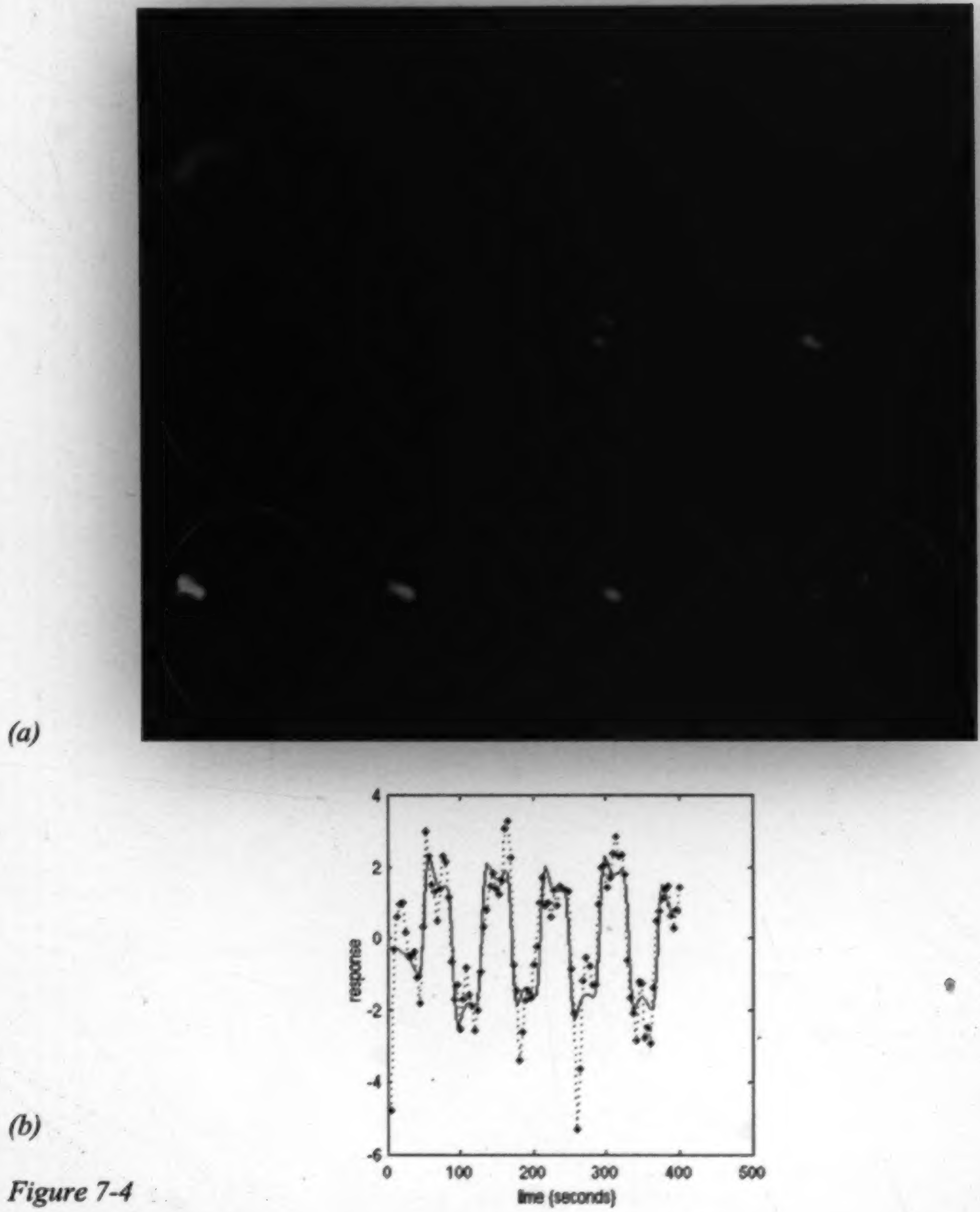
(a)
(b)
4
2
0
-2
-4
-6
response
0
100
200
300
400
500
ime (seconds)

Figure 7-4

(a) Group analysis of 18 subjects at baseline for the verbal task. Activation can be seen in the left and right frontal cortex as well as anterior cingulate and left superior parietal lobule (Left=Left side of brain, Right=Right side of brain). Brighter intensity reflects higher statistical significance. (b) signal time course from a single activated voxel.

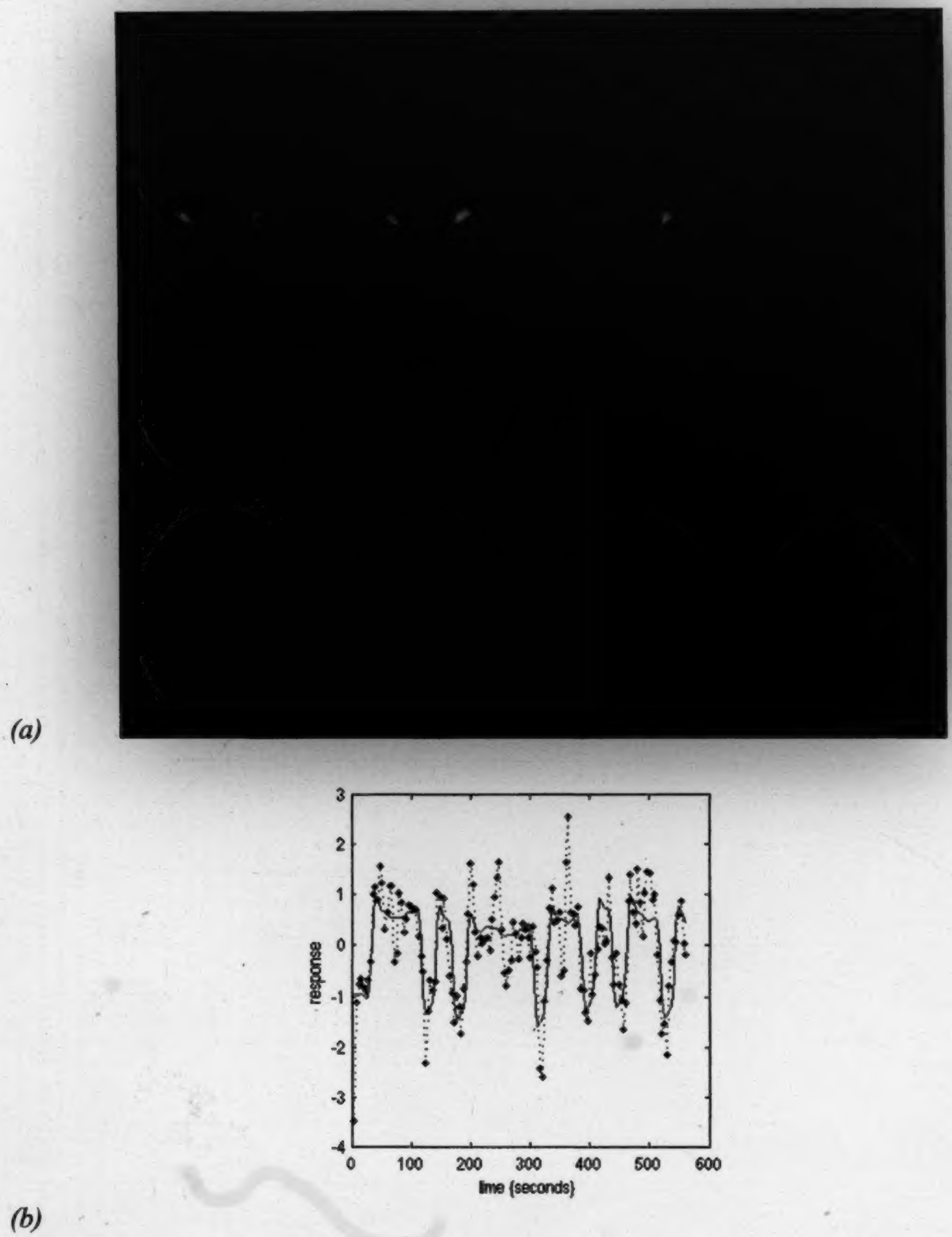

Figure 7-5

(a) Group analysis of all 18 subjects at baseline for the memory task. Activation can be seen in the left and right insula, left and right superior parietal lobule and left frontal cortex, (L=L, R=R). (b) signal time course from a single activated voxel.

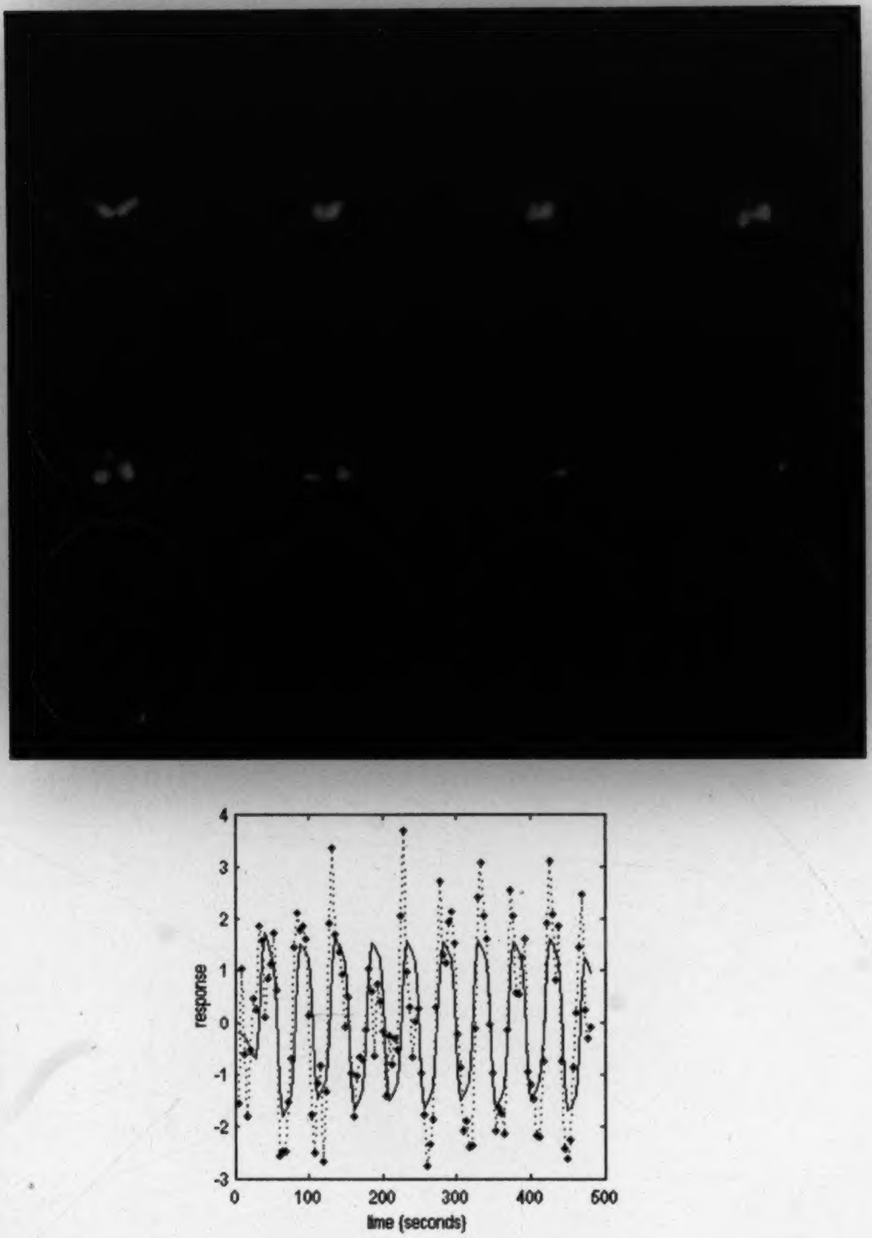

(a)

4
3
2
1
0
-1
-2
-3
response
0
100
200
300
400
500
time (seconds)

Figure 7-6

(a) Group analysis of all 18 subjects at baseline for the reaction task. Activation can be seen in the occipital cortex (primary visual cortex), superior and inferior parietal lobule, and fusiform gyrus. (L=L, R=R) (b) signal time course for a single activated voxel.

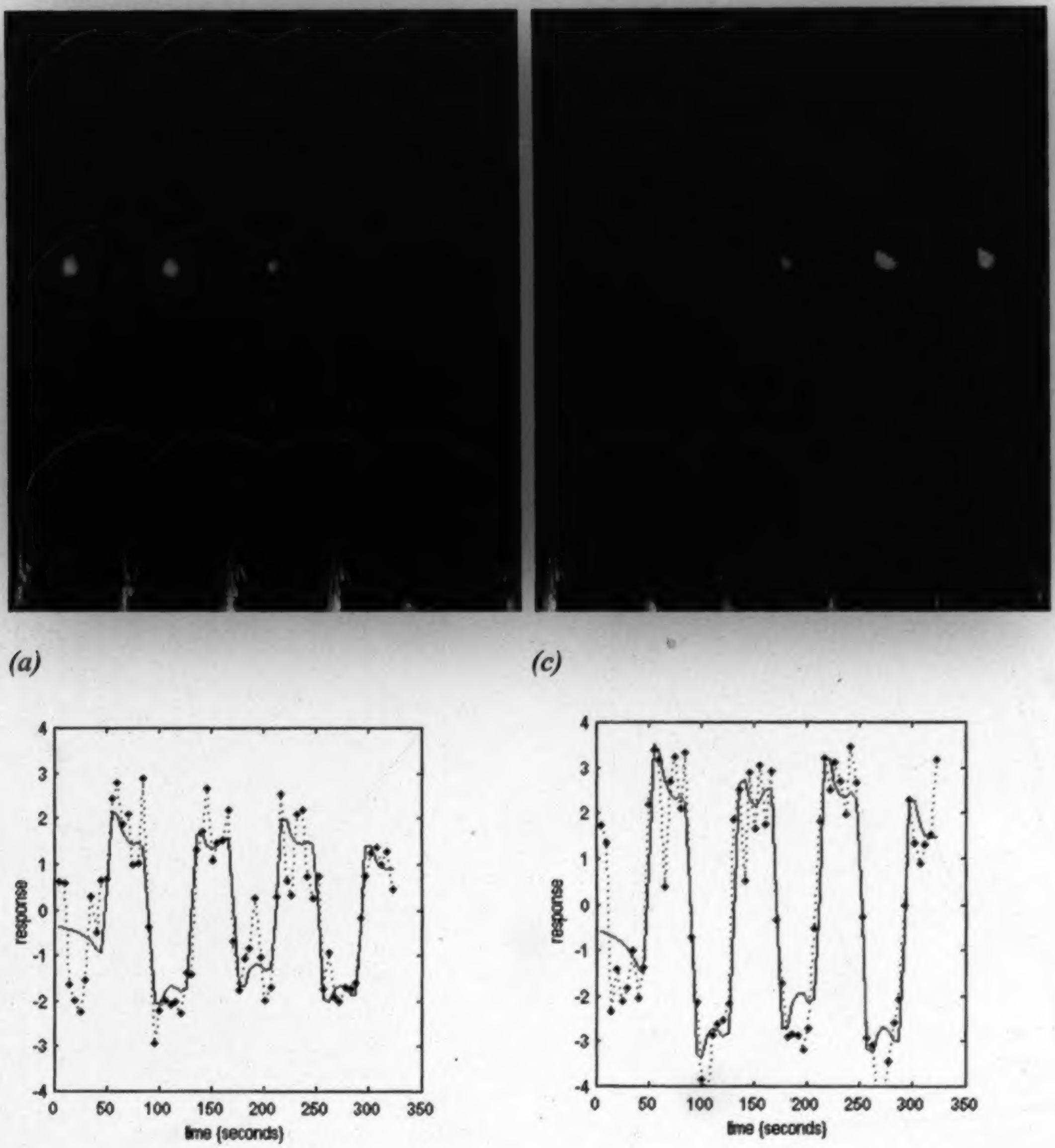
response
time (seconds)
4
3
2
1
0
-1
-2
-3
-4
0
50
100
150
200
250
300
350

(a) *(c)*

(b) *(d)*

Figure 7-7

Group analysis of the motor tasks showing brain activation and a representative time course from the most significant voxel. (a,b) right hand motor task, (c,d) left hand motor task. Brain activation is seen in contralateral primary motor cortex, cingulate, and superior temporal regions. (L=L, R=R)

7.5 Functional MRI ROI Analysis Results

Region of interest functional MRI analysis was performed for all five tasks using the number of activated pixels and the magnitude of the BOLD response. For each task, seven comparisons were made to evaluate (1) the effects of amphetamines, (2-3) the effects of lithium, (4-5) two control tasks, and (6-7) the effects of lithium on amphetamine stimulation as described in Section 6.4. Table 7-3 shows a summary of the results for each task and all seven comparisons.

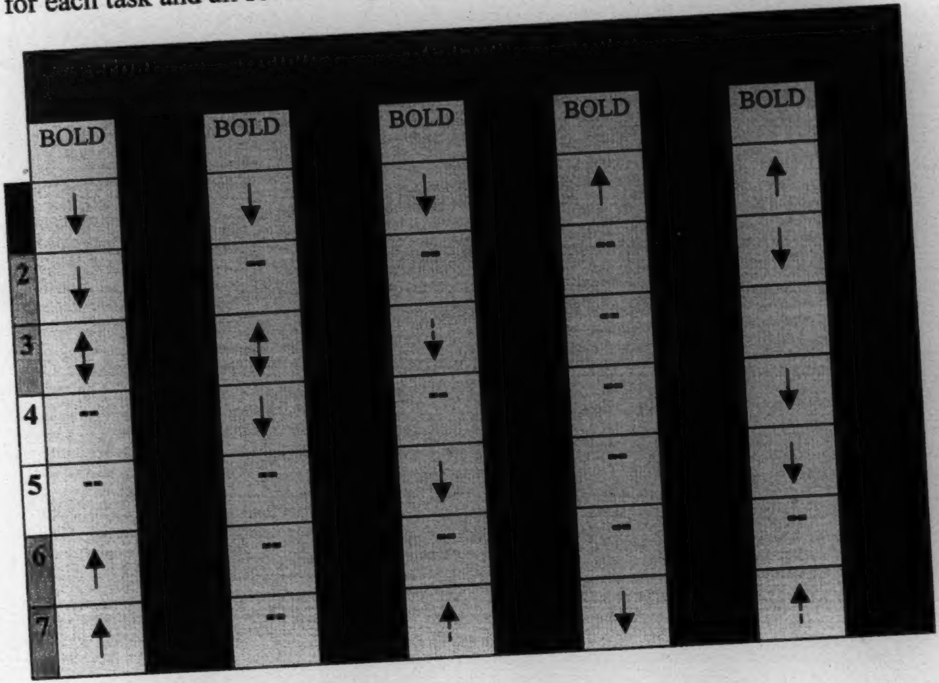

	BOLD	BOLD	BOLD	BOLD	BOLD
	↓	↓	↓	↑	↑
2	↓	--	--	--	↓
3	↕	↕	⇣	--	
4	--	↓	--	--	↓
5	--	--	↓	--	↓
6	↑	--	--	--	--
7	↑	--	⇡	↓	⇡

Table 7-3

Summary data for each of the tasks and the seven comparisons performed. A solid arrow ↑ or ↓ indicates that at least one region was found to have a significant response in the indicated direction ($p < 0.05$) for that comparison. A dashed arrow, ⇡ or ⇣ indicates that there were one or more regions that showed a trend ($0.05 \leq p \geq 0.08$) towards change. A double arrow, ↕ indicates that at least one region responded with an increase and one with a decrease.

7.5.1 The Effects of Dextroamphetamine

The effect of a single dose of 25 mg dextroamphetamine was to reduce the number of activated pixels in the memory task and verbal task as measured using fMRI. There were no significant differences in the number of activated pixels for the left and right hand motor tasks or the reaction task. The magnitude of the BOLD contrast was reduced by dextroamphetamine for the reaction task, memory task, and verbal task and increased for both motor tasks.

(1) Effects of Dextroamphetamine						
Verbal Task						
	BOLD Contrast			# Of Activated Pixels		
ROI	PRE	POST	p-value	PRE	POST	p-value
LIPL	1.9 ± 0.13	1.5 ± 0.09	0.003*	614 ± 128	345 ± 75	0.02*
LSPL				307 ± 59	230 ± 43	0.07
LPCG				760 ± 138	538 ± 91	0.04*
CING				305 ± 88	151 ± 42	0.07
Memory Task						
LDLPFC	1.3 ± 0.09	1.1 ± 0.08	0.03*			
LIF				236 ± 73	86 ± 29	0.04*
LMF	1.5 ± 0.11	1.3 ± 0.10	0.06	139 ± 35	65 ± 29	0.02*
LSF	1.2 ± 0.10	1.0 ± 0.07	0.04*	54 ± 17	19 ± 7	0.04*
LPCG				268 ± 61	160 ± 38	0.03*
CING	1.1 ± 0.07	1.0 ± 0.06	0.008*	92 ± 29	29 ± 12	0.03*
LI	1.1 ± 0.08	0.9 ± 0.08	0.06			
Reaction Task						
RMOG	1.2 ± 0.09	1.1 ± 0.7	0.01*			
RLG	2.1 ± 0.16	1.9 ± 0.15	0.04*			
Motor Left Hand Task						
RPSM	3.2 ± 0.19	3.9 ± 0.23	0.008*			
LIF	1.1 ± 0.08	1.6 ± 0.21	0.02*			
Motor Right Hand Task						
LIF	1.0 ± 0.09	1.3 ± 0.15	0.04*			

Table 7-4

The effects of dextroamphetamine on the number of activated pixels and BOLD contrast for the verbal task, memory task, reaction task, motor left hand task, and motor right hand task (mean ± SE). Only areas that showed a significant change or a trend towards change are shown.

7.5.2 The Effects of Lithium

The effect of lithium on cerebral blood flow and brain activity was tested using two comparisons. The first assessment used only the lithium group, which received lithium treatment for fourteen days, comparing the number of activated pixels and magnitude of the BOLD response for pre versus post medication. Lithium caused a decrease in the number of activated pixels for the lithium group in the verbal task, and right hand motor task. There was also a trend towards a decrease for the memory task. The magnitude of the BOLD response was also decreased for the lithium group post treatment for the verbal task and motor right hand task. The memory, reaction, and left hand motor tasks showed lithium had no effect on the magnitude of the BOLD response.

(2) Effects of Lithium						
Verbal Task						
	BOLD Contrast			# Of Activated Pixels		
ROI	PRE	POST	p-value	PRE	POST	p-value
RIPL	1.2 ± 0.25	0.8 ± 0.14	0.07			
LSPL	1.8 ± 0.17	1.4 ± 0.09	0.03*	325 ± 95	125 ± 33	0.06
RSPL	1.3 ± 0.24	0.9 ± 0.14	0.04*	45 ± 18	4 ± 4	0.03*
CING				358 ± 131	75 ± 22	0.07
Memory Task						
RIP				21 ± 8	6 ± 5	0.05
Reaction Task						
No Significant Differences						
Motor Left Hand Task						
No Significant Differences						
Motor Right Hand Task						
LSTG	2.4 ± 0.35	2.0 ± 0.36	0.04*	301 ± 114	65 ± 35	0.04*

Table 7-5

The effects of lithium on the number of activated pixels and BOLD contrast for the five tasks (mean ± SE). Only areas that showed a significant change of a trend towards change are shown.

The second test compared the number of activated pixels and magnitude of the BOLD response for the placebo group after treatment versus the lithium group after treatment. In this test memory, verbal, and reaction tasks all showed a decrease in the number of activated pixels caused by lithium compared to placebo. The magnitude of the BOLD response showed a significant change for the memory task and verbal task. The effect was heterogeneous with some areas showing a significant increase and some a decrease in the BOLD response for the lithium group compared to placebo.

(3) Effects of Lithium						
Verbal Task						
	BOLD Contrast			**# Of Activated Pixels**		
ROI	**POST Placebo**	**POST Lithium**	**p-value**	**POST Placebo**	**POST Lithium**	**p-value**
RIPL				63 ± 24	4 ± 4	0.02*
LSPL				302 ± 96	125 ± 33	0.08*
RSPL	1.4 ± 0.09	0.9 ± 0.14	0.009*	90 ± 26	4 ± 4	0.003*
LPCG	1.7 ± 0.12	2.3 ± 0.23	0.04*			
Memory Task						
RIPL	1.4 ± 0.13	1.0 ± 0.11	0.04*	65 ± 31	6 ± 5	0.08
LIOG	2.2 ± 0.26	1.6 ± 0.14	0.07	360 ± 60	171 ± 61	0.04*
LIF	1.3 ± 0.19	1.9 ± 0.24	0.04*			
Reaction Task						
LLG	2.4 ± 0.26	1.9 ± 0.17	0.07			
CUN				721 ± 227	221 ± 52	0.03*
LMOG				429 ± 120	177 ± 36	0.05
Motor Left Hand Task						
No Significant Differences						
Motor Right Hand Task						
No Significant Differences						

Table 7-6

The effects of lithium on the number of activated pixels and BOLD contrast (mean ± SE) for the verbal task, the memory task, the reaction task, the left hand motor task and the right hand motor task. Only areas that showed a significant change of a trend towards change are shown.

7.5.3 Control Comparisons

Two comparisons were identified as control comparisons. The first control comparison evaluated any differences between the group that would receive placebo treatment and the group that would eventually receive lithium treatment in the change caused by dextroamphetamine before treatment. The memory task and motor right hand task each showed a single area significantly different between the placebo group and lithium group for the change in the magnitude of the BOLD response caused by dextroamphetamine before treatment.

(4) Control Comparison						
Memory Task						
	BOLD Contrast			# Of Activated Pixels		
ROI	Change 1	Change 2	p-value	Change 1	Change 2	p-value
RSF	0.12 ± 0.11	-0.6 ± 0.18	0.004*			
Motor Right Hand Task						
LSTG	0.4 ± 0.17	-0.3 ± 0.17	0.01*			

Table 7-7

The change in the magnitude of the BOLD contrast and number of activated pixels (mean ± SE) caused by dextroamphetamine for the placebo group (change 1) versus the lithium group (change 2) prior to treatment.

The second control comparison was used to ensure there was no difference between the first and second administrations of amphetamine for the placebo group. The reaction task and the motor right task showed a difference in the magnitude of the BOLD response for the placebo group when comparing the change caused by amphetamines for the first and second administration of amphetamine. The memory task also showed a single area significantly different for the change in the number of activated pixels caused by dextroamphetamine for the two administrations of the drug for the placebo group.

(5) Control Comparison						
Memory Task						
	BOLD Contrast			**# Of Activated Pixels**		
ROI	**Change 1**	**Change 3**	**p-value**	**Change 1**	**Change 3**	**p-value**
RSPL				111 ± 60	-57 ±33	0.03*
Reaction Task						
LLG	0.2 ± 0.18	-0.5 ± 0.21	0.004*			
Motor Right Task						
SMA	0.2 ± 0.14	-0.4 ± 0.18	0.02*			

Table 7-8

The change in the magnitude of the BOLD response and number of activated pixels caused by dextroamphetamine for the first (change 1) and second (change 2) administrations of the drug (mean ± SE).

7.5.4 The Effects of Lithium on Dextroamphetamine Stimulation

The effects of lithium on dextroamphetamine stimulation was analysed using two comparisons. The first compared the change in the number of activated pixels and the BOLD response for the lithium group before and after treatment. Treatment with lithium had the effect of reversing or attenuating the change in the number of activated pixels caused by dextroamphetamine in the verbal task and motor right task. The memory task and motor left task showed a trend towards the same results. Lithium also caused a reversal of the BOLD intensity changes caused by dextroamphetamine administration for the verbal task. Figures 7-8 and 7-9 show the reversal of the change caused by amphetamine after treatment with lithium for the verbal task in the regions of interest that reached statistical significance.

(6) Effects of Lithium on Dextroamphetamine Stimulation						
Verbal Task						
	BOLD Contrast			# Of Activated Pixels		
ROI	Change 2	Change 4	p-value	Change 2	Change 4	p-value
RDLPFC	-0.2 ± 0.14	0.4 ± 0.11	0.02*			
LIPL				-320 ± 180	301 ± 165	0.03*
LSPL	-0.2 ± 0.13	0.8 ± 0.33	0.02*	-107 ± 52	345 ± 133	0.02*
RSPL	-0.1 ± 0.18	0.4 ± 0.22	0.08			
CING	-0.4 ± 0.19	0.3 ± 0.24	0.06	-266 ± 163	105 ± 64	0.04*
SMA				-442 ± 224	109 ± 127	0.01*
Memory Task						
RSF				-52 ± 22	-7 ± 11	0.07
Reaction Task						
No Significant Differences						
Motor Left Hand Task						
RSTG				133 ± 82	-111 ± 70	0.07
Motor Right Hand Task						
LSTG				-123 ± 28	120 ± 91	0.03*

Table 7-9

The effects of fourteen days of lithium treatment on the change in the number of activated pixels and the magnitude of the BOLD response caused by dextroamphetamine for the lithium group before and after medication (mean ± SE).

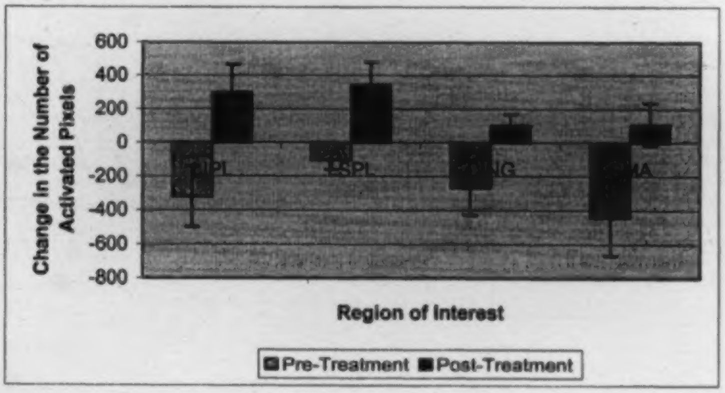

Figure 7-8

The effects of lithium treatment of the number of activated pixels (mean ± SE) for the verbal task, pre lithium treatment versus post lithium treatment.

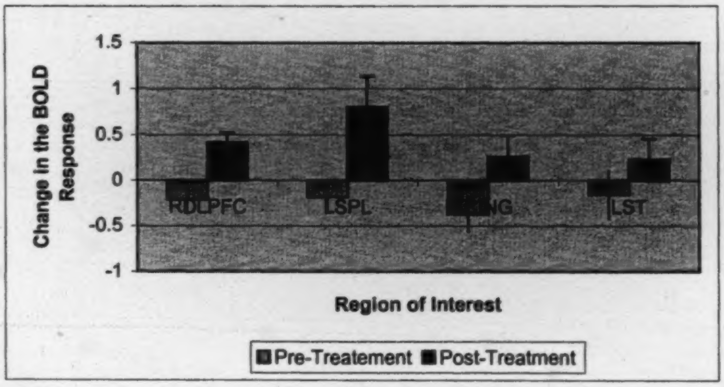

Figure 7-9

The effects of lithium treatment of the magnitude of the BOLD response (mean ± SE) for the verbal task, pre lithium treatment versus post lithium treatment.

The second comparison used to evaluate the effects of lithium on dextroamphetamine stimulation involved the comparison of the change in the number of activated pixels and the magnitude of the BOLD response caused by dextroamphetamine for the placebo group versus the lithium group after treatment. The verbal and reaction tasks show that lithium reverses or attenuates the effects of dextroamphetamine in the number of activated pixels. The motor left hand and motor right hand show a trend towards the same result. Additionally, the verbal, and motor left tasks show a significant reversal of the changes caused by dextroamphetamine in the magnitude of the BOLD response. The reaction task and motor right task show also show a trend that indicates lithium attenuated the effects of dextroamphetamine.

(7) Effects of Lithium on Dextroamphetamine Stimulation						
Verbal Task						
	BOLD Contrast			# Of Activated Pixels		
ROI	**Change 3**	**Change 4**	**p-value**	**Change 3**	**Change 4**	**p-value**
RDLPFC	-0.1 ± 0.18	0.4 ± 0.11	0.01*			
LIPL	-0.4 ± 0.21	0.5 ± 0.37	0.06			
LSPL	-0.1 ± 0.22	0.8 ± 0.33	0.05	-38 ± 88	345 ± 133	0.04*
Memory Task						
No Significant Differences						
Reaction Task						
CUN	-0.4 ± 0.09	0.2 ± 0.26	0.07	-316 ± 167	281 ± 208	0.04*
LMOG				-121 ± 98	150 ± 63	0.03*
LLG	-0.5 ± 0.21	-0.1 ± 0.09	0.07	-221 ± 97	324 ± 148	0.01*
RLG				-114 ± 76	154 ± 99	0.05*
Motor Left Hand Task						
RPSM	1.2 ± 0.32	-0.3 ± 0.29	0.004*			
RSTG				65 ± 65	-111 ± 70	0.08
Motor Right Hand Task						
LSTG	-0.5 ± 0.33	0.4 ± 0.27	0.06	-108 ± 61	120 ± 91	0.05
LIPL				-87 ± 50	57 ± 53	0.07

Table 7-10

The effects of fourteen days of treatment with lithium on the change caused by dextroamphetamine in the number of activated pixels and the magnitude of the BOLD response for those treated with placebo versus those treated with lithium (mean ± SE).

Chapter 8

Discussion

8.1 Introduction

The following chapter is an analysis and discussion of the results obtained from the fMRI study looking at the effects of dextroamphetamine and lithium on cerebral blood flow and brain activity. Each conclusion obtained from the study is presented and analyzed in the context of possible explanations for the given results and previous research related to the finding.

8.2 Dextroamphetamine Causes a Decrease in Cerebral Blood Flow and Brain Activity

As a model for mania, the effects of dextroamphetamine on cerebral blood flow and brain activity are important for understanding the pathophysiology of this condition. In the present study it has been shown that dextroamphetamine causes a decrease in cerebral blood flow and brain activity as measured using functional magnetic resonance imaging. These changes are not uniform across all the tasks studied; instead, dextroamphetamine caused both task specific changes and region specific changes. This result is consistent with previously published research using dextroamphetamine. Using PET and SPECT imaging techniques, dextroamphetamine has been shown to be a vasoconstrictive agent leading to decreases in global cerebral blood flow and metabolism [1-3]. This effect is similar to the effects of other stimulants such as caffeine [4]. However, not all studies are consistent with this finding. In a study evaluating the response to dextroamphetamine

(0.4mg/kg) on resting cerebral blood flow, it was concluded that the drug caused regional increases and decreases in specific cognitive areas, increasing rCBF in two prefrontal regions, inferior frontal lobe, brain stem, temporal lobe and thalamus and decreasing rCBF to motor cortex, visual cortex, fusiform gyrus and areas of the temporal lobe [5]. Furthermore, in another study using two abstract reasoning tasks to evaluate the response to dextroamphetamine (0.25 mg/kg), the Wisconsin Card Sorting Task (WCST) and the Ravens Progressive Matrices Task (RPMT), blood flow increased in the inferior frontal gyrus during WCST but decreased during RPMT. In a similar manner, blood flow in the hippocampus decreased during WCST performance and increased during RPMT [6]. This suggests that amphetamine may not have consistent regional effects; instead, the changes may be task dependant. Using new techniques such as fMRI and flow-sensitive alternating inversion recovery (FAIR) scan sequences to measure blood oxygen level dependent contrast and CBF respectively have not been able to show completely persuasive evidence for dextroamphetamine's effects on the brain. Using fMRI to measure the BOLD contrast change and the number of activated pixels in regions of interest while performing a tone decision task or a motor task with the thumb and index finger, a significant increase in the number of activated pixels was detected in the left and right primary auditory cortices for the tone decision task and the ipsilateral primary sensorimotor cortex and right middle frontal area during the motor task. In this study it was found that there were no changes in the magnitude of the BOLD contrast caused by dextroamphetamine [7]. In a follow up to the WCST and RPMT PET study, an fMRI study was performed using a working memory task. In a similar manner to the PET results, it was found that dextroamphetamine had dissociated effects on BOLD contrast measured using fMRI. An increase in the BOLD contrast was found for a high working memory load condition whereas a decrease was found during performance of a low working memory load condition [8]. Studies looking at the effects of other stimulants such as caffeine and cocaine have also shown that increases or decreased in the BOLD response are possible after drug administration [9-10]

Although changes in cerebral blood flow are typically considered, it is also possible that the effects of dextroamphetamine on blood flow and brain activity are caused by directly affecting neuronal activity. A decrease in the spatial extent of activation could reasonably be caused by a direct decrease in the number of neurons recruited to perform the task, or a decrease in the metabolic requirements of the neurons while performing the specific task. This model of dextroamphetamine stimulation would suggest that dextroamphetamine has the effect of increasing the efficiency with which the brain performs the given task. There are several studies that suggest indirect monoamine agonists such as dextroamphetamine optimize the response of neurons in both a task and region specific manner [6,8,11]. By increasing the efficiency by which neurons respond to a particular task it has been hypothesized that an increase in the BOLD response will accompany dextroamphetamine stimulation. After dextroamphetamine is administered the same absolute magnitude of the BOLD response is achieved; however, it is now compared to a relatively reduced baseline due to decreased cerebral blood flow. The net result is a proportional increase in BOLD contrast compared to baseline. Although not a consistent finding in the results of the present study it was found that for the motor tasks dextroamphetamine did increase BOLD contrast.

8.3 Lithium Causes a Decrease in Cerebral Blood Flow and Brain Activity

Although lithium is the most frequently prescribed prophylactic treatment for bipolar disorder and has been used and studied in medicine for over one hundred and sixty years, its mechanism of action remains unresolved. Therefore, it is of great interest to evaluate the effects of lithium on cerebral blood flow and brain activity in healthy volunteers. In this study, lithium was found to decrease the spatial extent of brain activation in a region specific manner. The magnitude of the BOLD response also showed significant changes as a result of lithium treatment causing areas of increased BOLD contrast and areas of decreased BOLD contrast. The postulated effects of lithium on the phosphatidylinositol cycle (PI) may explain the decrease in cerebral activation caused by lithium administration. Lithium affects the PI cycle by decreasing the concentration of *myo*-inositol and attenuating the effectiveness of the PI cycle. I-1,4,5-P_3, which acts as an intracellular second messenger that increases the release of calcium from intracellular stores within the endoplasmic reticulum, is reduced by attenuation of the PI cycle. By decreasing the levels of calcium release, lithium may decrease the amount of neurotransmitter released following a given level of receptor stimulation. Therefore, it is reasonable to assume that lithium would attenuate brain activity as measured using fMRI. However, other possibilities must also be considered as mechanisms by which lithium reduces brain activity and blood flow. Lithium may cause specific changes in global cerebral blood flow or in regional blood flow that would account for changes in activity. Also, lithium may cause changes in membrane transport systems, neurotransmitter receptor regulation, second messenger signaling, protein kinase C (PKC) regulation, and gene expression which could affect the vascular response itself, or directly affecting neuronal activity and metabolism.

Research into CBF changes associated with the administration of other medications effective in depression or mania has shown similar results to those in the present study. Benzodiazepines such as diazepam have been reported to reduce CBF [12]. Antidepressants such as fluoxetine (Prozac) report no CBF changes in healthy volunteers and decreased rCBF in patients treated for depressive disorder [13,14]. Perhaps most surprising is a study using the typical antipsychotic haloperidol, which found that the medication had no effect on CBF in a group of schizophrenic patients but significantly reduced global CBF in a healthy control group [15]. Another study of medications used in schizophrenia using an atypical antipsychotic, risperidone, concluded that risperidone had the effect of increasing frontal cortical activation measured using fMRI [16].

The evidence from this study and others using non-invasive methods to evaluate the effects of psychiatric medication on cerebral blood flow and brain activity show how difficult it is to study a wide range of disorders with a large group of drugs which may act via different mechanisms but lead to a similar reduction of psychiatric symptoms. The same drug may have different effects in healthy controls compared to patients and even different effects within subgroups of the patient population.

8.4 Lithium Causes a Reversal of the Effects of Dextroamphetamine Stimulation on Cerebral Blood Flow and Brain Activity

Dextroamphetamine causes an increase in blood pressure, heart rate, subjective measures of mood and physical well being, catecholamine activity, and cerebral metabolism similar to the changes associated with mania [17-19]. However, it is unclear if the mechanism of dextroamphetamine's actions is the same as naturally occurring mania. Dextroamphetamine is thought to function by increasing the levels of catecholamine neurotransmitters such as dopamine and norepinephrine through inhibition of their reuptake in the synaptic cleft, increasing their release, or binding directly to post synaptic receptors. Through stimulation of dopamine and norepinephrine pathways dextroamphetamine leads to stimulation of the PI cycle. Recently, using ^{1}H and ^{31}P magnetic resonance spectroscopy (MRS) it was confirmed that dextroamphetamine administration led to increases in the activity of the PI cycle measurable as increases in the peak area ratios of *myo*-inositol and the phosphomonoester (PME) peak, which contains inositol monophosphates as well as other phosphates [20]. The proposed mechanism of action of lithium, the inositol depletion hypothesis, is that lithium attenuates the effects of the PI cycle through noncompetitive inhibition of the enzymes IMPase and IPPase, which are involved in the breakdown of inositol phosphates to *myo*-inositol. Therefore, if both proposed mechanisms of action are correct, then lithium should function to reverse the effects of stimulation of the PI cycle by dextroamphetamine.

Most studies have shown lithium to reverse or attenuate the subjective effects of dextroamphetamine stimulation [21]. Also, using ^{1}H and ^{31}P magnetic resonance spectroscopy (MRS), it has been shown that stimulation of the PI cycle with an acute dextroamphetamine administration following treatment with lithium led to an increase in inositol monophosphates, which supports the inositol depletion hypothesis [22]. In this study we have further validated the use of dextroamphetamine as a model for mania by showing that lithium reverses the effects of dextroamphetamine on cerebral blood flow and brain activity measured using fMRI. For three of the five tasks, dextroamphetamine alone caused a significant decrease in the number of activated pixels or in the magnitude of the BOLD response. After fourteen days of lithium treatment the administration of dextroamphetamine caused an increase in the spatial extent of activation and BOLD contrast. This is the first time fMRI has been used to evaluate the effects of lithium on dextroamphetamine stimulation and the results suggest that dextroamphetamine is a valid model for mania since it induces the same subjective and physiological effects at the naturally occurring condition and responds to the same pharmacological treatment.

8.5 The Use of Functional Magnetic Resonance Imaging in Psychiatric Research

Functional magnetic resonance imaging is based on indirect measurements of neuronal activity via changes in blood oxygenation. As such, it has several possible weaknesses. For example, using fMRI alone, it is not possible to detect if changes in neuronal activity are excitatory or inhibitory as both processes require energy and therefore require oxygen. However, functional MRI does have significant advantages over earlier techniques such as CT, PET, and SPECT in terms of enhanced spatial and temporal resolution, noninvasive nature, and absence of radiation exposure. The use of fMRI in psychiatric research allows the researcher to study in vivo the relationship between altered cerebral activation patterns and the psychopathologic and cognitive features of psychiatric disorders. Therefore, fMRI is a useful research tool in the evaluation of psychiatric disorders to evaluate changes associated with certain pathological disorders or conditions as well as continued research into the mechanism of action of psychiatric medications.

8.6 References

1. Mathew, R.J. and Wilson, W.H. (1985), *Dextroamphetamine-Induces Changes in Regional Cerebral Blood Flow.* Psychopharmacology, 87: 298-302.
2. Wolkin, A. et al. (1987), *Effects of Amphetamine on Local Cerebral Metabolism in Normal and Schizophrenic Subjects as Measured by Positron Emission Tomography.* Psychopharmacology, 92: 241-246.
3. Kahn, D.A. et al. (1989), *Dissociated Effects of Amphetamine on Arousal and Cortical Blood Flow in Humans.* Biological Psychiatry, 25: 755-767.
4. Mathew, R.J. et al. (1983), *Caffeine and Cerebral Blood Flow.* British Journal of Psychiatry, 143: 604-608.
5. Devous, M.D. et al. (2001), *Regional Cerebral Blood Flow Response to Oral Amphetamine Challenge in Healthy Volunteers.* Journal of Nuclear Medicine, 42: 535-542.
6. Mattay, V.S. (1996), *Dextroamphetamine Enhances "Neural Network Specific" Physiological Signals: A Positron Emission Tomography rCBF Study.* The Journal of Neuroscience, 16: 4816-4822.
7. Uftring, S.J. et al. (2001), *An fMRI Study of the Effect of Amphetamine on Brain Activity.* Neuropsychopharmacology, 25: 925-935.
8. Mattay, V.S. et al. (2000), *Effects of Dextroamphetamine on Coginitive Performance and Cortical Activation.* Neuroimage, 12: 268-275.
9. Mulderink, T.A. et al. (2002), *On the Use of Caffeine as a Contrast Booster for BOLD fMRI Studies.* Neuroimage, 15: 37-44.

10. Gollub, R.L. et al. (1998), *Cocaine Decreases Cortical Cerebral Blood Flow But Does Not Obscure Regional Activation in Functional Magnetic Resonance Imaging in Human Subjects.* Journal of Cerebral Blood Flow and Metabolism, 18: 724-734.

11. Daniel, D.G. et al. (1991), *The Effect of Amphetamine on Regional Cerebral Blood Flow During Cognitive Activation in Schizophrenia.* Journal of Neuroscience, 11: 1907-1917.

12. Mathew, R.J. and Wilson, W.H. (1991), *Evaluation of the Effects of Diazepam and an Experimental Anti-Anxiety Drug on Regional Cerebral Blood Flow.* Psychiatry Research, 40: 125-134.

13. Kocmur, M et al. (1998), *Evaluation of Brain Perfusion with Technetium-99m Bicisate Single Photon Emission Tomography in Patients with Depressive Disorder Before and After Drug Treatment.* European Journal of Nuclear Medicine, 25: 1412-1414.

14. Bonne, O. et al. (1999), *Clinical Doses of Fluoxetine and Cerebral Blood Flow in Healthy Volunteers.* Psychopharmacology, 143: 24-28.

15. Goldman, R.G. et al. (1996), *Acute Effects of Haloperidol on Cerebral Cortex Blood Flow in Normal and Schizophrenic Subjects.* Biological Psychiatry, 40: 604-608.

16. Honey, G.D. et al. (1999), *Differences in Frontal Cortical Activation By a Working Memory Task After Substitution of Risperidone for Typical Antipsychotic Drugs in Patients with Schizophrenia.* Proceedings of the National Academy of Sciences, 96: 13432-13437.

17. Jacobs, D. and Silverstone, T. (1986), *Dextroamphetamine-Induced Arousal in Human Subjects as a Model for Mania.* Psychological Medicine, 16: 323-329.

18. Diehl, D.J. and Gershon, S. (1992), *The Role of Dopamine in Mood Disorders.* Comprehensive Psychiatry, 33: 115-20.

19. Vollenweider, F.X. et al. (1998), *Effects of High Amphetamine Dose on Mood and Cerebral Glucose Metabolism in Normal Volunteers Using Positron Emission Tomography (PET).* Psychiatry Research, 83: 149-62.

20. Silverstone, P.H. et al. (2002), *Dextro-Amphetamine Increases Phosphoinositol Cycle Activity in Volunteers: An MRS Study.* Human Psychopharmacology, 17: 425-429.

21. Jacobs, D. and Silverstone, T. (1986), *Dextroamphetamine Induced Arousal in Human Subjects as a Model for Mania.* Psychological Medicine, 16: 323-329.

22. Silverstone, P.H. et al. (1999), *Effects of Lithium and Amphetamine on Inositol Metabolism in the Human Brain as Measured by* ^{1}H *and* ^{31}P *MRS.* Biological Psychiatry, 46: 1634-1641.

Chapter 9

Conclusions

The work presented in this thesis represents the first use of fMRI at 1.5T at the University of Alberta. The fMRI study, evaluating the effects of dextroamphetamine and lithium on cerebral blood flow in healthy volunteers, also embodies the first collaboration between the Department of Biomedical Engineering and the Department of Psychiatry for an fMRI study. Through the completion of this project we have been able to develop the framework by which future MRI studies can be performed at 1.5T, and the infrastructure, techniques, and experience gained will ensure that the development of fMRI at higher field strengths of 3T and 4.7T will be a smooth transition.

The results from a double blind, placebo-controlled drug study using functional magnetic resonance imaging to investigate the effects of lithium and dextroamphetamine on cerebral blood flow and brain activity have also shown that fMRI can be applied to drug research and psychiatry to achieve meaningful results. In our study, it was concluded that dextroamphetamine and lithium both function to decrease brain activation as measured using fMRI. Also, lithium was able to reverse the effects of dextroamphetamine stimulation after treatment.

Functional magnetic resonance imaging is a powerful research tool for investigations in psychology, psychiatry, neuroscience, and many other disciplines. However, the elucidation of the mechanisms by which a drug or task cause an increase in the spatial extent or intensity of the BOLD response remains impossible using fMRI alone. By combining fMRI with other MR applications such as perfusion imaging and arterial spin labeling or in combination with other modalities such as electroencephalography or magnetoencephalography it may be possible to obtain a greater understanding of what an increase or decrease in fMRI signal actually corresponds to. The limits of functional MRI resolution are not dictated by technical or instrumental requirements. Instead the indirect method of measuring cerebral blood flow suffers from temporal resolution limits of a few seconds and spatial localization limits that may be on the order of a few millimeters. Even with high field MRI systems precise mapping of cerebral blood flow changes to increases in neuronal activity may not be possible.

Increasingly, more complex statistical analysis programs hold promise in reducing functional imaging experiment times or allowing for single event paradigms that yield reliable robust results. In the future at the University of Alberta it may be possible to automate many of the image processing steps so as to minimize operator input time, increase productivity, and make better use of computer resources.

The movement of fMRI experiments up to higher field systems such as 3.0T or 4.7T holds promise of higher signal to noise ratios that will make the evaluation of more complex or subtle cognitive functions. However, appropriate methods for precise shimming of the magnet will be required to account for increased susceptibility at higher fields.

Future directions in the development of fMRI at the University of Alberta include collaboration with other departments to help in the development of appropriate paradigms to evaluate interesting cognitive functions. From a technical standpoint it will become more important to have accurate timing between the paradigm delivery system and the MRI hardware. A triggering system will help, especially for event related studies, to eliminate any slight timing imperfections in the paradigm, which reduce the effectiveness of the statistical analysis.

The results from chapter 7 show that the use of functional imaging in psychiatric research is of great interest. The medical community can use this type of research to better understand the pathophysiology of psychiatric disorders and the medications used to treat these conditions. For the engineering community, intensive research in this area promises solutions to technical challenges and advancement of specific MRI techniques to meet the needs of researchers and patients.

Appendix A

Analysis of a Sample fMRI Data Set

The following section presents a step-by-step analysis of a sample fMRI data set using SPM99. The data was collected at 1.5T using a standard finger tapping paradigm with the following parameters: TR = 5.04s, TE = 50s, 128x128 matrix, 30 contiguous slices 3mm thick to cover the motor cortex and 66 time points. The total imaging time is then 5min 32s. The first two volumes where discarded before analysis to allow the magnetization to approach steady state. Therefore 1920 images will be used in the analysis. The paradigm consists of four 40s blocks of tapping the thumb and forefinger of the right hand alternated with four 40s blocks of rest where subjects remained as still as possible. This section is not comprehensive in terms of the details involved in each step. For more information refer to the SPM manual available on the SPM website [1]. All SPM related MATLAB files that are not released with SPM99 can be found in *C://MATLAB11/spm_m_files* on fMRI PC in the NMR Research Facility.

Data Transfer and Preparation

After the fMRI data is collected the images must be sent offline for processing. From the main screen on the 1.5T Seimens scanner choose:

Patient → Browser

from the tab bar at the top of the screen. Select the series you want to transfer by clicking on the image icon next to the image data. Next choose:

Transfer → Export to off-line

and type in the destination of the computer the images will be transferred to. For example, to transfer to Paradigm15 computer type:

//Paradigm15/E_Drive/Your_Folder_Name/Motor_Right

Once the transfer of data is complete (the status can be checked by clicking on the telephone icon at the bottom of the screen or choosing *Transfer → Local job status* from the Patient Browser) the data must be renumbered so that the files sort in numerical order. This is accomplished by using the program **IMA Tool** available on the Paradigm15 PC. Open IMA Tool then drag and drop the folder containing the images to be renumbered onto the program interface. Choosing the option "Drop Everything After the Slice Name in the New Filenames" will remove the time stamp and DICOM information from the image name. For example the images will be renamed as follows.

MR_Morgan_Functional_SUBJ1.3.14.2002.09.31.19284758940.ima

to

MR_Morgan_Functional_SUBJ1.3.0014.ima

Where Morgan_Functional is the study name, SUBJ1 is the subject name, 3 is the series number and 0014 is the image or slice number.

IMA Image Conversion

SPM99 uses images in the Analyze format (Mayo Clinic, Rochester, USA) therefore images must be converted from ima to Analyze. An Analyze image contains all the slices from a single time point. In our case this means that each Analyze image will contain 30 slices. The conversion is performed using a free software program called MRIcro [2]. To convert a series of images from ima format to Analyze start MRIcro and choose:

Import → Convert Foreign to Analyze

The following window will appear.

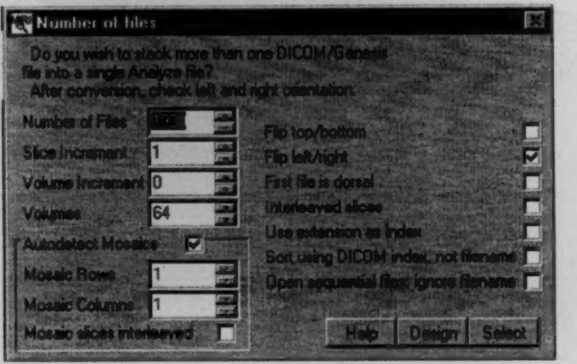

Do you wish to stack more than one DICOM/Genesis file into a single Analyze file?
After conversion, check left and right orientation.

Number of Files [illegible]
Slice Increment 1
Volume Increment 0
Volumes 64
Autodetect Mosaics ☑
Mosaic Rows 1
Mosaic Columns 1
Mosaic slices interleaved ☐

Flip top/bottom ☐
Flip left/right ☑
First file is dorsal ☐
Interleaved slices ☐
Use extension as index ☐
Sort using DICOM index, not filename ☐
Open sequential files; ignore filename ☐

Figure A-1

The conversion of IMA files to Analyze format using MRIcro.

Enter 1920 for the number of files and 64 for the number of volumes. Ensure that the *Flip left/right* box is checked to maintain the proper orientation for later steps. MRIcro will then prompt you to choose the first image in the series make a 4D Analyze image that contains 64 time points. The next step will be to separate this 4D image into 64 individual Analyze images that each contain 30 slices. First open the 4D Analyze image just created.

File → Open Image

MRIcro will prompt you to choose which of the 64 time points you would like to open from the 4D Analyze image. Choose volume one. Next, from the tab menu at the top of the screen choose:

File → Save As

From the pop up window press *Save (Intel).* The next window will ask you if you would like to save the 4D Analyze image as multiple 3D images. Choose *Segment Padded* to save the new images in numerical order. Now there should be 64 Analyze images that each of which contains a single volume of images and represents a single time point in the series of functional MRI data.

Data Preprocessing (SPM)

Reorientation

The first step using SPM is to reorient the images to that they are in the same orientation as the SPM templates. Select *Display* from the SPM interface then select the first image in the fMRI series. The image needs to be flipped and translated so that the upper left box contains a coronal view, the lower left box contains an axial view with the front of the brain at the top of the box, and the top right box should contain a saggital view with the front of the brain on the left side of the box. Enter a –1 in the resize x, and resize y boxes to flip the images to the proper orientation. Next enter values in the boxes for translation and rotations to align the blue cross hairs with the anterior commissure. For more information on locating the anterior commissure see reference [3]. Select *Reorient Images* then select all the images in the data set.

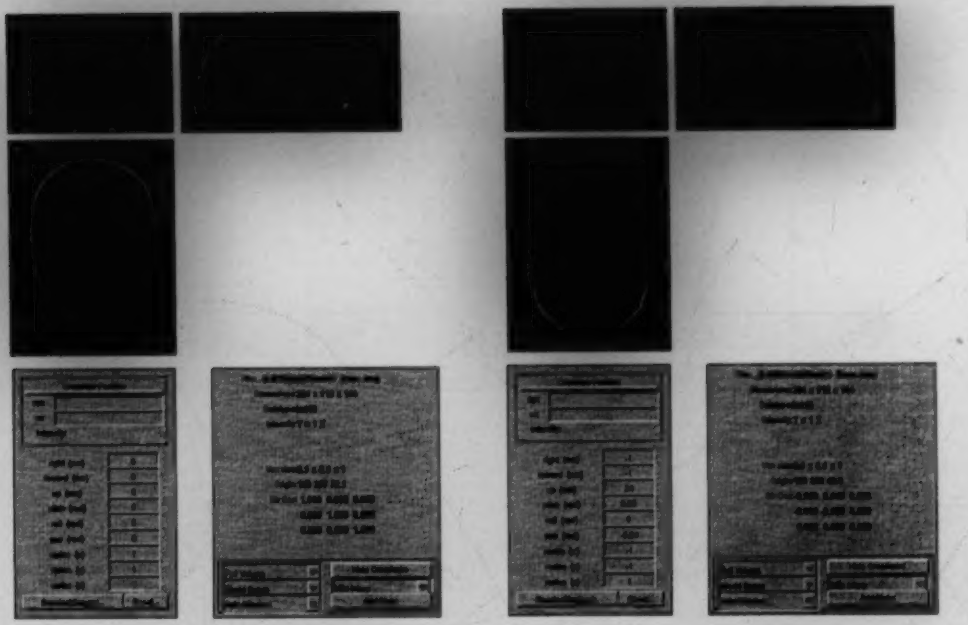

Figure A-2: Reorientation of an Analyze image using SPM. a) before reorientation, b) after reorientation to match the orientation of the template images.

Realignment

Select *Realign* from the SPM window.

Number of Subjects	*"1"*
Number of Sessions for Subject 1	*"1"*
Select Images	*Choose all the *.img files in the data set (1-64)*
Which Option?	*"coregister and reslice"*
Reslice Interpolation Method	*"tri-linear interpolation"*

For most applications tri-linear interpolation is a good compromise between accuracy and processing time. If sinc interpolation is chosen the interpolation will be more accurate but at the cost of an approximate doubling of the time required to realign the images.

Create What? *"mean image only"*

After the images are realigned a graph will appear in the SPM Display window. This graph depicts the motion parameters for the three translations and three rotations used in the realignment process. Typing rd_motion in the MATLAB command window will generate a table of the motion parameters including mean, max and standard deviation of each translation or rotation.

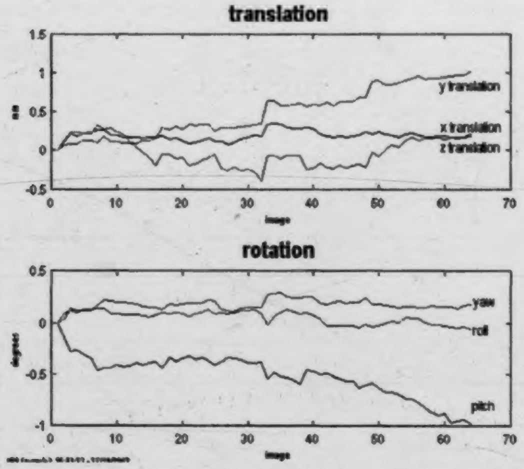

Figure A-3

Motion parameters detected by SPM during realignment of the image series to the first image in the data set.

Normalization

Select *Normalize* from the SPM window.

Which Option? *"determine parameters and write normalized"*

Number of Subjects?	*"1"*
Image to Determine Parameters	*Choose the mean*.img file created during realignment*
Images to Write Normalized	*Choose all the *.img files in the data set*
Template Image	*"EPI.img"*
Interpolation Method	*"bilinear interpolation"*

After normalization has completed the quality should be evaluated by choosing *Check Reg* from the SPM window. If normalization is unsatisfactory it is possible to change the number of non-linear iterations and the number of non-linear basis functions used to place more or less emphasis on spatial warping in the normalization process.

Smoothing

Select *Smooth* from the SPM window

Smoothing {FWHM in mm}	*"8"*
Select Images	*Choose all the newly created normalized images in the data set (n*.img's)*

Model Specification and Estimation

Select *fMRI Models* from the SPM window.

What would you like to do?	*"Specify and Estimate a Model"*
Number of Sessions?	*"1"*

Select Scans for Session 1	*Choose all the smoothed, normalized images in the data set (sn*.img's)*
Interscan Interval (s)	*"5.04"*
Number of Conditions or Trials	*"1"*
Name for Condition 1	*"Finger Tapping Right Hand"*
SOA (Stimulus Onset Asynchrony)	*"Fixed"*

SOA refers to the period of time (in scans) between two consecutive repetitions of the same event. If this interval is constant for the entire task then choose "fixed" if it is not then choose "variable" and then enter a vector list of the first scan in each repetition of the task.

SOA (scans for Finger Tapping Right Hand) "16"

The finger-tapping paradigm has a block of eight scans at rest followed by eight scans of the task. Therefore the SOA for our task is 16 scans in duration.

Time to First Trial (scans)	*"8"*

The first block in the finger tapping is rest. Therefore the finger-tapping condition begins on the eighth scan.

Parametric Modulation	*"none"*

Parametric modulation is chosen to conduct analysis using a predictor variable that varies parametrically across the experiment.

Are These Trials...	*"Epochs"*

Epochs refer to trials grouped into blocks that span a specified number of scans.

Select the Type of Response	*"fixed response - box car"*

Selecting "box car" specifies the expected response function that the general linear model will use to calculate how well the voxel response follows the task.

Convolve with hrf *"yes"*

Convolving with a hrf adds the hemodynamic response function into the box car model. This function serves to delay and spread out the expected response to the task.

Add Temporal Derivatives *"no"*

Temporal derivatives add the derivative of each regressor (the height of the box car) into the general linear model. These can be used to model a slight time shift in the regressor or to account for slight timing imperfections in the model.

Epoch Length (scans) for Finger Tapping *"8"*

Interaction Among Trials (Volterra) *"no"*

Volterra allows modeling of the interaction of successive trials, or the influence one activity at previous time has on the signal at a later time point.

User Specified Regressors *"0"*

Additional regressors can be added to the model to help explain some of the variance in the functional data time series and hence improve the sensitivity of the model to activation. It is sometimes useful to add the realignment parameters to the model to help explain some of the variance in the data. To use the realignment parameters as regressors choose *"User Specified Regressors → 1"* then hit "*Enter*". Next type *"spm_load"* in the text box and press *"Enter"*. Choose the *realignment_params*.txt* file that was created during realignment. Caution should be used when adding realignment parameters to the model design. If the subject motion is highly correlated with the task then these parameters will explain much of the activation in the model rather than the variance leading to substantially less activation in the final analysis. To evaluate how correlated the realignment parameters and the task are type *"rd_taskcorr('Motion')"* in the MATLAB terminal window. This program will return a table of p-values that represent the correlation between task and motion.

Remove Global Effects *"scale"*

Global effects can also be highly correlated to the paradigm if the global brain intensity varies with the task [4]. To evaluate how well global signal intensity correlates with the task type *"rd_taskcorr('Global')"* in the MATLAB terminal window. The table of p-values can then be used to decide whether global scaling will be beneficial or not.

High Pass Filter *"specify"*

A high pass filter is used to remove low frequency noise and signal drifts. By default a value is chosen four times the period of an epoch.

Session Cutoff Period (secs) *"161"*

Low Pass Filter *"hrf"*

The low pass filter attempts to make a correction for temporal autocorrelations in fMRI data. By using a low pass filter the temporal correlation in the data is dominated by the filter and is used to ensure the validity of certain assumptions in the statistical analysis.

Model Intrinsic Correlations *"none"*

Set up Specific F-contrasts *"no"*

Estimate *"now"*

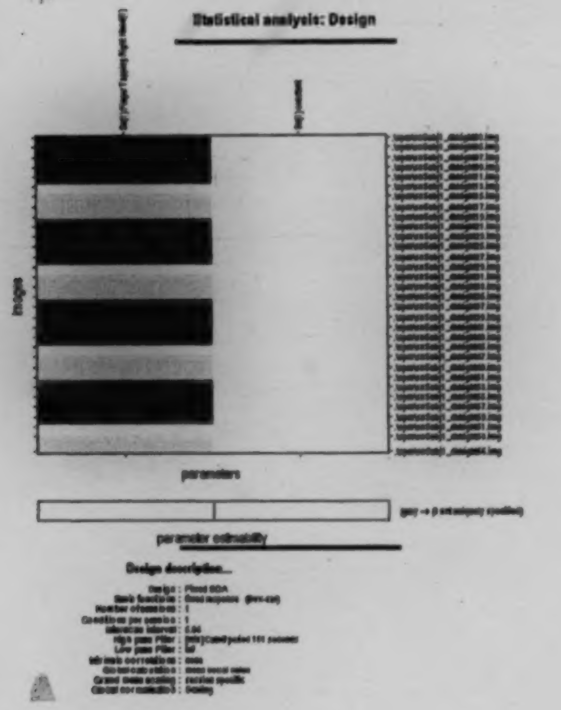
Statistical analysis: Design
images
parameters
parameter estimability
Design description...

Figure A-4

The output of the model specification stage in SPM99.

Results Assessment

Select *"Results"* from the SPM window.

Select SPM.mat	*Choose the SPM.mat file created in the MATLAB working directory during model estimation.*

A new window will appear with the design matrix on the right.

Define New Contrast	*Type the name of the new contrast in the top text box.*

Contrast	*Enter a "1" to see results where activation > rest.* *Enter a "-1" to see results where rest > activation*

Because there is only one parameter of interest in the general linear model, the height of the boxcar. A single contrast value is all that is needed to evaluate the model.

Mask With Other Contrast(s)	*"no"*

To view two or more contrasts using inclusive or exclusive masking select *"yes"* then select the appropriate contrast to mask.

Title For Comparison	*Enter a title for the comparison or press enter.*
Corrected Height Threshold	*"yes"*

A corrected height threshold refers to the use of p-values that have been corrected for multiple comparisons. If you have very specific apriori hypotheses about one specific region then it may be possible to use uncorrected p-values to assess results. For most applications however corrected p-values should be used to ensure the validity of the analysis.

Threshold	*"0.05"*
Extent Threshold	*"0"*

If you would only like to see activation clusters above a certain minimum threshold number of voxels then enter a value here. Otherwise set to zero to see the results from all available voxels.

References

1. http://www.fil.ion.ucl.ac.uk/spm *Statistical Parametric Mapping (SPM).* Wellcome Department of Cognitive Neurology, University College London.
2. http://www.psychology.nottingham.ac.uk/staff/cr1/mricro.html MRIcro, Dr. Chris Rorden, University of Nottingham.
3. http://www.mrccbu.cam.ac.ul/Imaging/antcomm.html Dr. Matthew Brett, Medical Research Counsel, Cambridge.
4. Desjardins, A.E. (2001), *Removal of Confounding Effects of Global Signal In Functional Magnetic Resonance Imaging Analyses.* Neuroimage, 13:751-758.